

Isotope Planetology

Inaugural-Dissertation
zur
Erlangung des Doktorgrades
der Mathematisch-Naturwissenschaftlichen Fakultät
der Universität zu Köln

vorgelegt von

Maxwell Marzban Thiemens

aus San Diego

Köln, 2018

Berichtersteller
(Gutachter)

Prof. Dr. Carsten Münker

Dr. Dominik Hezel

Tag der mündlichen Prüfung: 11.1.19

*A process cannot be understood by stopping it.
Understanding must move with the flow of the process,
must join it and flow with it.*

Dune

By F. Herbert

1965

Table of Contents

Table of Contents.....	5
1.0 Acknowledgements	7
2.0 Overview	9
2.1 Abstract.....	10
2.2 Zusammenfassung.....	12
3.0 Introduction	15
3.1 Early Solar System Evolution	16
3.2 Lunar Genesis.....	19
3.3 The Lunar Magma Ocean.....	23
3.4 Lunar Isotopic Composition	30
3.5 From Earth's formation to mantle rocks from the Eifel	33
3.6 Motivation and Objectives	39
4.0 Isotopic investigations of peridotites from the West Eifel Volcanic Field.....	44
4.1.0 Introduction	45
4.1.1 Background	45
4.1.2 Geological Setting	48
4.2.1 Methods and Samples	51
4.3.0 Results.....	52
4.3.1 Microprobe Analysis	52
4.3.2 Isotope Analyses	55
4.4.0 Discussion	62
4.4.1 Direct chronological information - mineral isochrons and model ages	62
4.4.2 Indirect chronological information from recently reset peridotites	64
4.5.0 Conclusions	66
5.0 Isotope dating of lunar meteorite NWA 6950	72
5.1.0 Introduction	73
5.2.0 Methods.....	76
5.3.0 Results.....	78
5.4.0 Discussion	82
5.4.1 The age of NWA 6950	82
5.4.2 Age spectra within the NWA 773 clan	84
5.4.3 NWA 6950 and the evolution of (ur)KREEP	86

5.4.4	NWA 6950 representing KREEP evolution.....	89
5.4.5	Differing model ages.....	90
5.5.0	Conclusions.....	92
6.0	New Evidence for an Old Moon.....	94
6.1.0	Introduction.....	95
6.2.0	Methods and Results.....	97
6.2.1	Sample selection.....	97
6.2.2	Sample Preparation.....	98
6.2.3	Analytical protocols.....	103
6.2.4	Results - modeling constraints.....	104
6.2.5	Lunar Magma Ocean fractionation and partial melting modeling.....	105
6.2.6	Results.....	107
6.4.0	Discussion.....	108
6.5.0	Conclusions.....	115
Appendix 1.0	Lunar Samples Gallery.....	119
A1.1	Apollo 11.....	120
A1.2	Apollo 12.....	121
A1.3	Apollo 13.....	123
A1.4	Apollo 14.....	123
A1.5	Apollo 15.....	124
A1.6	Apollo 16.....	126
A1.7	Apollo 17.....	127
Appendix 2.0	References.....	130
Appendix 3.0	Erklärung.....	155
Appendix 4.0	Curriculum Vitae:.....	156

1.0 Acknowledgements

I gratefully acknowledge funding from the ERC grant 669666 “Infant Earth” to Carsten Münker and SPI385 1/1 to Peter Sprung. This work wouldn’t have been possible without the Apollo samples provided by CAPTEM, or by Northwest Africa 6950, provided by Randy Korotev. Without these the work would not have been possible.

Chronologically, of course, it is prudent to thank my parents first. Both Mom and Dad encouraged me towards study and the application of this from to was the most fundamental help towards the writing of this thesis. Thank you both for everything you have done.

The skills applied to this thesis have similarly been developed over time. Dr. Schuller’s lab was the first I worked in, and I learned fundamental presentation skills (as well as some computer programming). I then learned lab etiquette with Dr. Kummel, for which I greatly owe thanks to him and the team of welcoming graduate students in his lab. Dr. Keating’s lab was where I spent the most time, and where I learned how to deal with students, bureacracy, and failed experiments. Dr. Renbarger was my mentor, and continued to provide advice for years after I left the lab. This thesis is built upon the foundation you all made.

I would still be floundering through physics if Dr. Moynier had not suggested I try isotope chemistry. While the projects themselves had their own hiccups, I am incredibly appreciative for the opportunity he gave me.

Similarly, my subsequent research endeavors were largely guided by Dr. Peter Sprung. He has, for years, provided a sounding board, a role model, and incredible feedback. His sweat and blood are in this thesis, and there is no way to encompass how appreciative I am for the magnitude of his work.

In a similar vein, I would thank Dr. Carsten Münker who has provided the funding, feedback, and final reads (penultimate, at best, but I didn’t want to lose alliteration) on this work. You’ve been a great help both socially and scientifically, Carsten. Thank you for everything.

This work also owes much to Dr. Raúl Fonseca. Raúl’s fingerprints are on “New Evidence for an Old Moon,” and his hard work and reliability are most appreciated. Thank you for being a R.O.C. that we all can count on.

I similarly would like to thank Dr. Dominik Hezel for being willing to serve on this committee, as well as for his advice and support. He was one of the first faculty I met from Cologne, and acted as a mentor at several key points during my time here (including the very beginning and very end).

Amongst my peers, first gratitude goes to Felipe Leitzke. My first presentation of my PhD was a co-presentation on the Moon with Felipe, and we've maintained that trend. He is a co-author, a hard worker, an inspiration, and a good friend.

I would also like to thank J. Tusch for his invaluable help on section 2.2. I hope I can some day repay him for it. Also, C. Marien for his collaboration on the final measurements. We pulled some long days, but have worthwhile data for it. Thank you both.

Last, but certainly not least, of my co-authors is Carina Gerritzen. Carina's thesis makes up the interesting data in the Eifel section of this work, and her diligence and hard work helped structure my own work. She has also scoured my reference list, and is an incredible partner. Thank you for everything you've done.

I would like to recognize and thank Dr. Günter Lugmair. *Nanos gigantum humeris insidentes*; I am as a dwarf, standing on the shoulder of giants. It seems that every chapter of this thesis had been touched upon by Günter before I was born, and I hope that I have expanded upon his works well.

It becomes harder to delineate how to thank everyone else. My thanks to everyone at the Schloss, with whom I have started this work, my doctor siblings, Ninja and Sebastian, for sharing this journey with me, and to everyone at the Black Box with whom I have finished it. Finally, my sister, Lillian, for being an amazing person who I love very much.

Humans become little isolated clusters on their isolated planets, and the social structure which defies that isolation stretches throughout this thesis. To the working planetologist, his most important tool is human beings. My thanks to all of you who have defied isolation with me.

2.0 Overview

...now I realise that great wisdom comes from simplicity.

Eisenhorn

By D. Abnett

2005

2.1 Abstract

The quest for in-depth knowledge of the formation and early evolution of the Earth-Moon system is a cornerstone of the planetary sciences. Virtually all chemical studies that address these key questions rely on the availability of extremely ancient rock samples (>4 billion years ago). On Earth's surface, active plate tectonics, weathering, and volcanism have destroyed nearly all ancient samples. Samples from the Moon are sufficiently old but strongly limited in quantity and cover only a small portion of the lunar surface.

The Moon is thought to have formed from the residue of an impact (or impacts) into the proto-Earth. There are two schools of thought as to when this occurred, one advocating an "old Moon" forming prior to 100 million years after solar system formation (SSF) and one supporting a "young Moon" forming later than 100 million years after SSF. This debate and the clear definition of the processes involved have continued unabated for the 50 years since lunar samples were first returned by the Apollo missions. A key to deepening our knowledge of these issues resides in understanding the extinct ^{182}Hf - ^{182}W decay system in lunar and terrestrial rocks.

To address this question, we analyzed a suite of 29 lunar samples from the Apollo missions to better understand the elemental Hf and W budgets of the moon. We used new high-precision, high field strength element (HFSE) analyses, combined with isotopic and experimental partitioning data in line with the lunar magma ocean (LMO) model. Through these methods it is possible to observe lunar mantle-wide heterogeneities in ratios of highly incompatible elements such as U/W, which are traditionally assumed to be invariant. This observation, in conjunction with ^{182}W isotope data for lunar rocks, supports the hypothesis of a Moon covered by a magma ocean after its formation. Crystallization and mixing of this LMO produced different hybrid cumulate sources; thus forming the sources of the distinct rock types found in the lunar sample suite.

Under the low oxygen fugacity conditions during lunar mantle partial melting, the low-Ti mare basalt source preferentially retains tungsten (W) over hafnium (Hf). The measured Hf/W values of low-Ti mare basalts thus provide a minimum for the Hf/W of the low-Ti source and by extension of the silicate Moon. We find that the Hf/W of the silicate Moon should lie between 30 to 50, significantly higher than the silicate Earth's modeled Hf/W of 25.8. Combined with a recently reported "global, uniform" ^{182}W excess in lunar samples, we find that in-situ decay of ^{182}Hf , in the time range between 40 to 60 million years after SSF is a superior explanation of the lunar ^{182}W excess instead of a previously suggested disproportionate "late accretion" of extraterrestrial material to the Moon and the Earth. Our finding lends clear support for an "old Moon."

We expanded our work on lunar samples to include the KREEP-rich gabbroic meteorite Northwest Africa (NWA) 6950. This meteorite yields new insight into the history of the KREEP reservoir which formed as the final residual melt of the LMO. A previous study had dated the meteorite to 3100 million years

ago through Pb-Pb dating of baddeleyite grains. This marks the NWA 6950 meteorite to be the youngest KREEP-like sample available and thus decisive for constraining lunar evolution. We obtained Lu-Hf, Sm-Nd, and Rb-Sr mineral isochrons for this meteorite. Through Lu-Hf dating we found an age of 3103 ± 39 million years ago, perfectly overlapping the Pb-Pb age and underpinning the significance of this meteorite's isotope systematics to anchor the evolution of KREEP. A Sm-Nd isochron of clean, hand-picked minerals yielded a compatible age of 3052 ± 57 million years ago. Inclusion of all mineral fractions that might have suffered later disturbance yields a young Sm-Nd isochron age of 2900 ± 200 million years ago that is closely akin to previous ages found via Ar-Ar (2800), Rb-Sr (2900), and Sm-Nd (2900) which dates younger resetting. In addition, the Rb-Sr isochron provides an even younger age of ca. 1450 million years ago, although this may bear no geological relevance. The significance of finding these young ages becomes clear considering that several Sm-Nd and Rb-Sr studies aimed to date related meteorites whose history might thus have been characterized incorrectly. The initial ϵ_{Hf} of NWA 6950 is the youngest anchor of the KREEP evolution line, from which we determined a time of KREEP formation at 4514 million years ago, or ca. 55 million years after SSF. We therefore found, through an entirely different line of research, independent support for an "old Moon" formation.

To calibrate this methodology, we investigated multiple peridotites from the West Eifel volcanic field of Germany that exhibit similarly low abundances of Lu, Hf, Sm, Nd, Rb, and Sr. For this project, three different ion exchange separation techniques were investigated as part of the calibration. Mineral isochrons of Lu-Hf, Sm-Nd, and Rb-Sr all provided a functionally modern age, indicative of a resetting event during the Quaternary. We also found that whole rock, host rock, and mineral compositions argue against equilibration of the host magma and the peridotite xenoliths. The observation that whole rock samples plot off the horizontal isochrons, in contrast, is explained by melt infiltration and grain boundary entrainment which likely postdated the resetting of the isochrons. One peridotite examined in a companion study supervised by myself (M.M. Thiemens) yielded four distinct ages. The Lu-Hf system was reset by a Quaternary age event, while the Hf isotope signature was highly radiogenic, indicative of differentiation from a modern mantle source between 1.22 and 1.76 Ga. Rb-Sr isochron data yielded an age of ca. 635 Ma, and a Sm-Nd age of 235 Ma corresponds with regional uplift. Our findings reveal that fine scaled isotope investigations are potent tools to unravel evolutionary complexities. The wealth of fine scaled information gained from the Eifel peridotite xenoliths once again underlines the stark contrast between the extremely dynamic evolution of the Earth's lithosphere and mantle when compared to the largely static lunar evolution following LMO crystallization.

2.2 Zusammenfassung

Ein tiefgreifendes Verständnis der Geschichte und Entwicklung des Erde-Mond Systems ist eine wesentliche Grundlage der Planetenwissenschaften. Die Verfügbarkeit von sehr alten Gesteinsproben (> 4 Milliarden Jahre) ist eine wichtige Voraussetzung für alle chemischen Studien, die sich dieser Thematik zuwenden. Verwitterung, Vulkanismus, sowie Plattentektonik zerstörten nahezu all solche alten Proben auf der Erdoberfläche. Proben vom Mond sind zwar ausreichend alt, jedoch stark limitiert und nur von wenigen Probenlokalitäten der Mondoberfläche verfügbar. Es wird angenommen, dass sich der Mond aus den Resten eines oder mehrerer Impakte mit der frühen Erde gebildet hat. Es koexistieren zwei Lehrmeinungen darüber wann dieses Ereignis stattfand. Die Denkschule der „old moon“ Fraktion vertritt die Ansicht, dass sich der Mond ca. 50 Millionen Jahre nach Entstehung des Sonnensystems bildete, wohingegen Verfechter der „young moon“ Fraktion 100 Millionen Jahre für realistischer halten. Die Diskussion über den Zeitpunkt der Mondentstehung sowie über die dabei beteiligten Prozesse dauern unvermindert an, seit vor ca. 50 Jahren die ersten Mondproben zur Erde gebracht wurden. Ein Zugang zu mehr Erkenntnissen bzgl. beider Prozesse liegt im Verständnis des ausgestorbenen $^{182}\text{Hf} - ^{182}\text{W}$ Isotopensystems in lunaren sowie terrestrischen Gesteinen.

Um dieser Frage nachzugehen, analysierten wir eine Suite von 29 Mondproben der Apollo Missionen auf ihren Gehalt an den Elementen Hf und W. Unsere hoch-präzisen Messungen der HFSE Elemente (high field strength elements – Elemente hoher Feldstärke) in Kombination mit Isotopendaten sowie experimentell ermittelten Verteilungskoeffizienten ist in Einklang mit dem lunar magma ocean (LMO) Modell. Unsere Untersuchungen offenbaren, dass Elementverhältnisse inkompatibler Elemente, wie etwa U/W, im Mantel des Mondes variieren. Diese Elementverhältnisse werden traditionellerweise als invariant erachtet. Diese Beobachtung, zusammen mit Isotopendaten für ^{182}W an Mondgesteinen, unterstützen die These eines Mondes, der nach seiner Entstehung von einem Magmaozean bedeckt war. Durch Kristallisation sowie Mischungsprozesse innerhalb dieses Magmaozeans entstanden unterschiedliche Kumulate; diese stellten die Quelle der verschiedenen Gesteinstypen dar, welche uns heute vorliegen.

Für die Quelle von low-Ti Basalten zeigt sich, dass aufgrund der reduzierten Bedingungen, welche auf dem Mond vorherrschen, beim partiellen Aufschmelzen W gegenüber Hf zurückgehalten wird. Die gemessenen Hf/W

Verhältnisse der low-Ti Basalte ermöglichen daher Minimalabschätzungen über das Hf/W Verhältnis der Mantelquelle, sowie das des Gesamtsilikat – Mond. Unseren Berechnungen zufolge liegt das Hf/W Verhältnis des Gesamtsilikat – Mond zwischen 30 und 50, und damit signifikant über dem modellierten Hf/W Verhältnis von 25.8 für die Gesamtsilikat – Erde. Unter Annahme eines einheitlichen ^{182}W Exzesses des Mondes, wie in jüngsten Publikationen postuliert, ist der in-situ Zerfall von ^{182}Hf im Zeitraum zwischen 40 und 60 Millionen Jahre nach Entstehung des Sonnensystems eine bessere Erklärung für die ^{182}W Exzesse, als die zuvor proklamierte ungleichmäßige Akkretion extraterrestrischer Materials für Erde und Mond. Unsere Erkenntnisse sind daher ein eindeutiger Beleg für einen „alten Mond“.

Wir erweiterten unsere Studien an Mondgesteinen um einen gabbroiden Mondmeteoriten vom Typ KREEP-rich aus der Gruppe northwest Africa (NWA) 6950. Dieser Meteorit ermöglicht neue Erkenntnisse über das KREEP Reservoir welches sich während der finalen Phase des LMO gebildet hat. Eine vorherige Studie bestimmte das Alter unter Anwendung der Pb-Pb Datierung an Baddeleyit auf 3100 Millionen Jahre. Dieses Alter belegt, dass es sich beim NWA 6950 Meteoriten um die jüngste verfügbare KREEP ähnliche Probe handelt und impliziert, dass sie für das Verständnis der Mondentwicklung von besonderer Bedeutung ist. Wir erstellten Lu-Hf, Sm-Nd, sowie Rb-Sr Mineralisochronen für diesen Meteoriten. Mittels Lu-Hf Datierung erhielten wir ein Alter von 3103 ± 39 Millionen Jahren, welches perfekt mit den Pb-Pb Altern übereinstimmt und die große Bedeutung der Isotopensystematik dieses Meteoriten herausstellt, da er als Ankerpunkt für die Entwicklung des KREEP Reservoirs dient. Eine Sm – Nd Isochrone von handgepickten einschlussfreien Mineralseparaten ergab ein konsistentes Alter von 3052 ± 57 Millionen Jahren. Unter Berücksichtigung aller Mineralfraktionen, welche sekundärer Alteration ausgesetzt worden sein könnten, ergibt ein jüngeres Sm – Nd Isochronen Alter von 2900 ± 200 Millionen Jahren, welches Altern ähnelt die zuvor durch Ar-Ar (2800), Rb-Sr (2900), sowie Sm-Nd (2900) erhoben wurden und ein resetting Ereignis datieren. Alter für Rb-Sr ergaben in dieser Studie sogar ein noch jüngeres Alter von ca. 1450 Millionen Jahren, welches sehr unwahrscheinlich ist. Die Bestimmung dieser jungen Alter ist von weitreichender Bedeutung, da viele Sm-Nd sowie Rb-Sr Studien an Meteoriten die Absicht hatten diese zu datieren und zu korrelieren, die Geschichte aber falsch rekonstruiert worden sein könnte. Das initiale ϵ_{Hf} von NWA 6950 ist der jüngste Ankerpunkt der KREEP Entwicklungslinie, durch die wir den Zeitpunkt der KREEP – Bildung auf 4514 Millionen Jahre beziffern, bzw.

auf 55 Millionen Jahre nach Entstehung des Sonnensystems. Durch diesen anderen analytischen Ansatz fanden wir einen weiteren unabhängigen Beleg für einen „alten Mond“.

Um die Methode der Isotopen – Altersdatierung zu überprüfen, führten wir Messungen an mehreren Peridotiten aus dem Vulkanfeld der West Eifel durch, welche ähnlich geringe Häufigkeiten an Lu, Hf, Sm, Nd, Rb sowie Sr aufweisen. Für die Separation dieser Elemente benutzten wir drei unterschiedliche chromatographische Abtrennverfahren. Mineral – Isochronen für Lu – Hf, Sm – Nd, sowie Rb – Sr ergaben moderne Alter, welche eine vulkanische Aktivität bzw. ein resetting der Isotopensysteme im Quartär bezeugen. Weiterhin zeigt die Zusammensetzungen der Minerale, des Gesamt- sowie Umgebungsgesteins, dass sich zwischen Peridotit Xenolithen und dem Umgebungsgestein kein chemisches Gleichgewicht einstellte. Dass das Gesamtgestein nicht auf der horizontalen Mineralisochrone liegt, deutet darauf hin, dass es zu einem späteren Zeitpunkt zur Infiltration von Schmelze sowie zu Bildung von Schmelzeinschlüssen an Korngrenzen kam. Ein Peridotit, welcher in einer von mir (M.M. Thiemens) betreuten Begleitstudie untersucht wurde, ergab vier voneinander abweichende Alter. Durch ein quartäres Ereignis wurde das $^{176}\text{Lu} - ^{176}\text{Hf}$ System zurückgesetzt, wohingegen eine besonders radiogene Hf Isotopensignatur eine Differentiation vom Mantel bezeugt, die sich zwischen 1.22 und 1.76 Milliarden Jahren vollzog. Isochronen für Rb – Sr ergeben ein Alter von ca. 635 Ma. Das Isochronenalter von 235 Ma für Sm – Nd fällt zeitlich mit regionalen Hebungsprozessen zusammen. Die Ergebnisse dieser Studie zeigen auf, dass durch hochauflösende Isotopenstudien komplexe Entwicklungen nachgezeichnet werden können. Das Vermögen der kleinräumigen Erkenntnisse, welche in unserer Studie zu den Peridotit Xenolithen der Eifel gewonnen wurden, verdeutlicht einmal mehr den großen Unterschied zwischen dem dynamischen System Lithosphäre – Mantel der Erde, und der vergleichsweise statischen Entwicklung des Mondes nach Kristallisation des Magmaozeans.

3.0 Introduction

*We are generalists. You can't draw neat lines around planet-wide problems.
Planetology is a cut-and-fit science.*

Dune

By F. Herbert

1965

3.1 Early Solar System Evolution

Knowledge grows from small pieces, bits and parcels which grow into general understanding (Herbert, 1976). Planetary formation follows a similar process (Kant, 1755). The solar system originated in a 65 light year across interstellar molecular cloud of dust and gas (Montmerle *et al.*, 2006). Part of this cloud collapsed in on itself, likely the consequence of nearby supernovae (Looney *et al.*, 2006), a theory supported by the abundance of short lived radionuclides (Cameron and Truran, 1977; Davies *et al.*, 2014 and references therein). The cloud collapsed into a dense disk of between 10^3 - 10^4 AU in the protostellar stage, with a bipolar outflow (e.g. Shu *et al.*, 1987; Montmerle *et al.*, 2006). By ca. 10^5 years the surrounding envelope collapsed even further, the disk stretching between 500 – 1000 Au in radius, with the three primary components at this stage being the outer envelope, collapsed disk, and the ejecting matter (Shang *et al.*, 2002; Matzner and McKee, 2000; Matsumoto *et al.*, 2000; Montmerle *et al.*, 2006).

This early disk evolved further, and by 0.1 Ga, the Sun had almost finished reaching its final mass, had created a 0.1 Au magnetosphere, and the ejection of material perpendicular to the Sun had depleted the majority of its angular momentum (e.g. Adams, 2010; Montmerle *et al.*, 2006 and references therein). The disk and envelope were originally composed of submicron-sized dust particles. These particles began to stick together, forming larger dust aggregates, which formed pebbles, which formed larger rocky bodies (planetesimals).

The earliest ages measured from solar system materials are found in Ca-Al rich inclusions (CAIs) found in carbonaceous chondrite meteorites. The youngest age measured was 4.568 Ga via Pb-Pb dating of a CAI from the meteorite northwest Africa 2364, which defines the timing of the formation of the solar system, hereafter referred to as T_0 (Bouvier and Wadhwa, 2010). This was later

suggested to be an artifact, with a revised aggregate age being

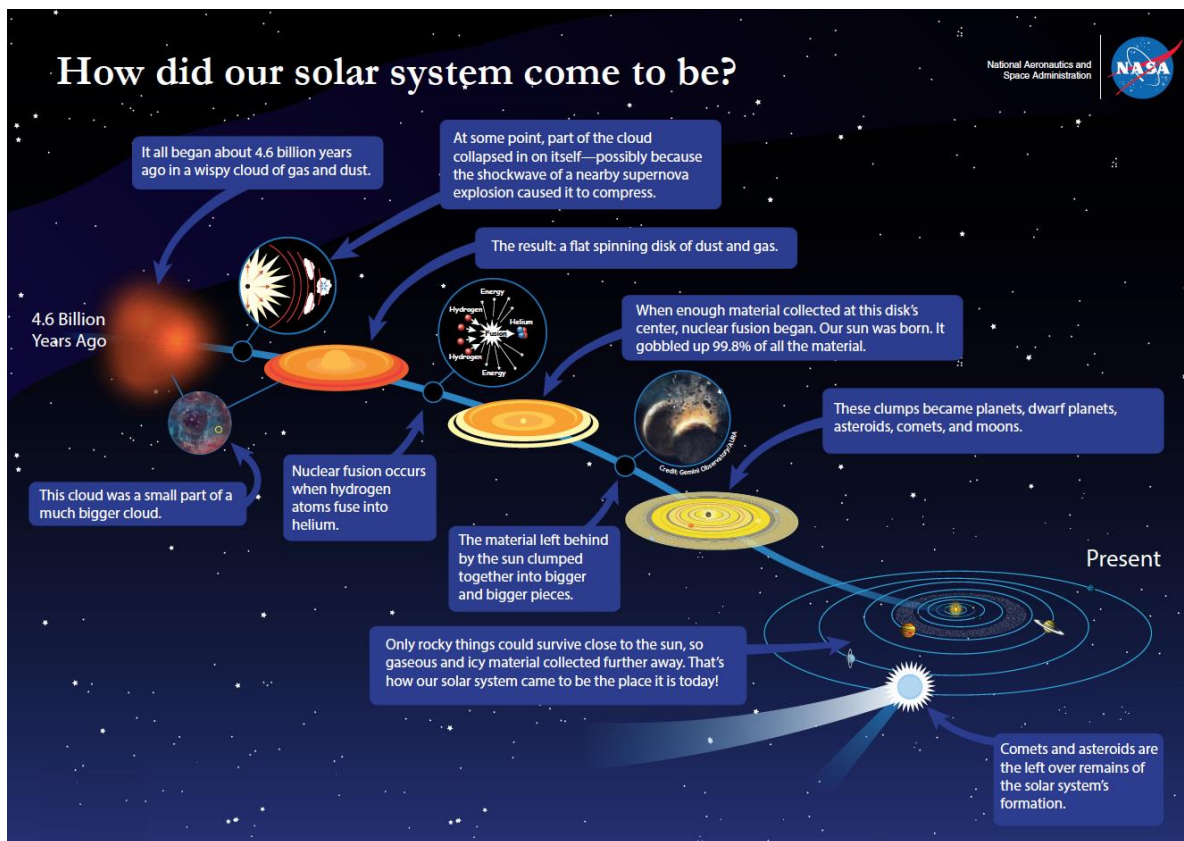


Figure 3.1: An aesthetic summary of the solar system's formation and evolution (image source: NASA.gov)

proposed instead at 4.567 Ga (Connelly *et al.*, 2017). The use of decay systems which went extinct in the early solar system such as ^{129}I (half-life 15.7 Ma, Reynolds, 1960), ^{10}Be (half-life 1.388 Ma, Korschinek *et al.*, 2009) and ^{41}Ca (half-life 0.103 Ma, Mabuchi *et al.*, 1974) constrain this timing further. CAIs also have the highest inferred initial $^{26}\text{Al}/^{27}\text{Al}$ ratio of any material formed in the solar system, the parent of the ^{26}Al - ^{26}Mg decay system (half-life .72Ma) (MacPherson *et al.*, 1995). The decay of ^{26}Al is thought to have acted as the principle heat source in planetesimals, leading to the differentiation of iron meteorites, as will be discussed later (e.g. Urey, 1955; Greenwood *et al.*, 2006; Gaidos *et al.*, 2009)

Following the formation of the CAIs, the more volatile compounds condensed, and chondrules formed by shock waves or flash heating (Palme *et al.*, 2015). Chondrules are typically sub-centimeter sized spherical igneous objects

which comprise chondritic meteorites (e.g. Connolly and Desch, 2004). While timing these events is difficult, it is generally thought that during the first 2-4 million years of the solar system chondrules and larger, undifferentiated bodies began to form (e.g. Bizzarro *et al.*, 2005; Connelly *et al.*, 2012). Perhaps even closer to T_0 is the formation of the parent bodies for igneous iron meteorites, which are modelled to have formed in the first 500 ky of the solar system, while igneous iron meteorites themselves then formed in the first 2 million years as metal cores of these bodies (e.g., Kruijer *et al.*, 2013, Wittig *et al.*, 2013). This would be contemporary with the accretion ages of achondrite groups and non-magmatic iron meteorites, which would subsequently differentiate between 3 and 5 million years after solar system formation (Schulz *et al.*, 2009), with further heating after 5 Ma (Schulz *et al.*, 2010). Recent studies have found this differentiation to have occurred ca. 6 million years after T_0 (Hunt *et al.*, 2018). These time intervals date the formation of planetesimals.

Although small materials have formed early in the solar system, the larger planetary bodies would take a commensurately longer time. While the gas giants formed in the first 0.1 Ma, the terrestrial planets took longer (Walsh *et al.*, 2011). Dating when the formation of terrestrial planets happened can be difficult with, for example, estimates for Mars ranging between 2 – 10 Ma (Nimmo and Kleine, 2007; Dauphas and Pourmand, 2011). The suggestion is that Mars stopped growing early, as Jupiter appropriated the material past 1 AU, leading to a starved planet (Walsh *et al.*, 2011). While this will be discussed in further detail, the partitioning between Hf and W allows for dating of planetary core formations. This has been used to suggest an age of Earth formation in the first 30 million years of the solar system (Kleine *et al.*, 2002), with 2/3 of Earth's mass having accreted in the first 10 million years (Rudge *et al.*, 2010). The latter study, however, leaves the termination of accretion as late as 100 million years after SSF. The study by König *et al.* (2011) found an age of 38 million years after solar system formation for the Earth itself through a ^{182}Hf - ^{182}W single stage model age for the

formation of the Earth's core based on high accuracy constraints of the Hf-W ratio for the silicate Earth.

The abundance of siderophile elements in the Earth's and other silicate mantles in the solar system is elevated compared to what they would be following core formation (Ringwood, 1966). The later suggestion was that a late (some 10^7 - 10^8 years after t_0) delivery of carbonaceous chondrite type material could explain the abundances of volatiles and siderophiles (Chou, 1978). Arguments have been made for when this occurred, but most modern studies find an age closer to 100 ± 50 My after SSF (Albarède, 2009; Ballhaus *et al.*, 2013; Schönbacher *et al.*, 2010). The later delivery of materials has consequences for dating core formation, as the addition of material following core formation would reset the bulk silicate inventory of siderophile elements. These signatures can be difficult to trace given the Earth's continual renewal and alteration of its surface by processes such as plate tectonics and weathering (e.g. Sobolev *et al.*, 2011). Fortunately, the Moon's surface has remained mostly unchanged, providing an analogue of what the Earth and its proto-crust could have looked like following its formation, and even harbor some early Earth material (e.g. Ozima *et al.*, 2008).

3.2 Lunar Genesis

Human study of the Moon is documented as far back as 5,000 years ago (Brennan, 1983). For many ancient cultures, the Moon represented a god such as Sin (Mesopotamian), Khonsu (Egyptian), Máni (Norse) or goddesses such as Selene (Greek) or Luna (Roman). These anthropomorphisms evolved as a way of trying to understand the Moon, and even as worship of the deities themselves has atrophied, it has continued to mark the vernacular used regarding the Moon. The adjective selenic, referring to things of or related to the Moon, derives from the goddess Selene. Similarly, the poetic name Luna and the commonly used adjective lunar both derive from the Roman goddess.

More modern explanations for the Moon's origin include lunar capture, fission, co-formation, and the big impact. Lunar capture holds that, rather than having formed near the Earth, the Moon formed elsewhere and was captured by the Earth (Urey, 1952). This process is one we have seen elsewhere in the solar system, such as Neptune's capture of its moon Triton (Agnor and Hamilton, 2006). The Kona conference in 1984 on the origin of the Moon found this to be unlikely based on the dynamics of the capture event (Hartmann *et al.*, 1986). As further evidence of the compositional similarities between the Earth and Moon were discovered, the extreme degree of coincidence required for the Moon to resemble the Earth so closely put to rest the lunar capture model (e.g. Dauphas *et al.*, 2014; Young *et al.*, 2016, references therein).

The fission model has the Earth forming alone. The Earth had a rapid spin, ca. 2.5 hours per rotation, causing centrifugal force to eject material which forms the Moon (Darwin, 1879, Jeans, 1929). This accounts for the density difference between the two bodies, as Earth's core has already formed while the residual molten material forms the Moon (Darwin, 1879). The scar on Earth's surface from this event was thought to be the Pacific Ocean (Fisher 1889). This was also suggested as the cause for continental drift in pre-plate tectonic models (Ampferer 1925). The formation of Earth's core was thought to have caused angular acceleration causing the detachment of the Moon (Ringwood, 1960). This theory has been discarded for multiple reasons, such as the dissimilarities between the Moon and Earth's oceanic crust, ages of lunar materials, and the acceptance of plate tectonics.

The co-formation theory holds that the Earth and Moon formed as a simultaneously accreting binary planetary system (Thomson 1864). While this explains chemical similarities between the Earth and Moon, the difference in density between the two stands in contrast to this theory. This theory would later evolve to be an external incentive to fission, wherein the Earth and Moon

accreting from a residual cloud of proto-Earth material following a large impact (Daly 1946, Canup 2012).

The current, most accepted model synthesizes the fission and co-formation theories. In this, the early Earth is struck by another planetary body, creating a cloud of ejecta from which the Moon condenses (Daly 1946). Later reinvented as the giant impact theory, the primary version of this has a Mars-sized body (Canup and Asphaug 2001) striking the proto-Earth (Hartmann and Davis, 1975; Cameron and Ward, 1976). It explains the chemical similarities found between the Earth and Moon, while also explaining differences, such as the stronger depletion of volatiles on the Moon. It also explains the lunar orbit and angular momentum, the depletion of volatile and highly siderophile elements, and the enrichment in refractory elements in the Moon compared to the Earth. Refinements of this idea include having a rapidly spinning proto-Earth be struck, with the ensuing angular momentum of the post impact disk bleeding off by evection resonance between the Earth, Moon, and Sun (Cúk and Stewart, 2012; Canup 2014).

The Earth and Moon share chemical similarities in many things, particularly oxygen isotopes (Wiechert *et al.*, 2001, Young *et al.*, 2016). The $\Delta^{17}\text{O}$ signatures of both bodies is almost identical, indicating either a shared origin for the two or an impactor of identical composition to the Earth. Small differences between the two have been measured, though the origin of these may be the result of larger degrees of impactor melting, impactor and proto-Earth similarities, or later additions of material to the Earth (Herwatz *et al.*, 2014; Greenwood *et al.*, 2018). Earth-Moon isotopic similarities have also been found with near homogeneity of Ti isotopes (Zhang *et al.*, 2012) and Cr isotopes (Qin *et al.*, 2010; Mougél *et al.*, 2018). Given the extreme improbability of these isotopic similarities being the consequence of an impactor with an identical isotopic

signature to the proto-Earth, the consensus holds that the Earth and Moon share an origin (e.g. Dauphas *et al.*, 2014).

An issue with the similarity of the Earth and Moon signatures is that only 75% of the ejecta which formed the Moon would have originated from the Earth, given a Mars-sized impactor (Canup *et al.*, 2013). This has been, amongst many other ideas, explained by the impactor having been primarily composed of ice, meaning significant portions of it volatilized (Wolbeck and Connolly, 2010). It has also been suggested that, following the impact, a disk of material took 10^2 - 10^3 years before accreting into the Moon and back onto Earth, giving time for equilibration between the two (Pahlevan and Stevenson, 2007). Potassium isotope evidence indicates a high-energy, high-angular-momentum giant impactor as lunar rocks are enriched in the heavy isotopes of K compared to the Earth and chondrites (Wang and Jacobsen, 2016). Reufer *et al.*, (2012) explained the lunar formation as the consequence of multiple, rapid, indirect impactors, which could explain up to 73% of the Moon being composed of terrestrial material. More recently Rufu *et al.*, (2017) proposed a new model in which the Earth was struck with multiple impactors, creating multiple Moons which subsequently merged.

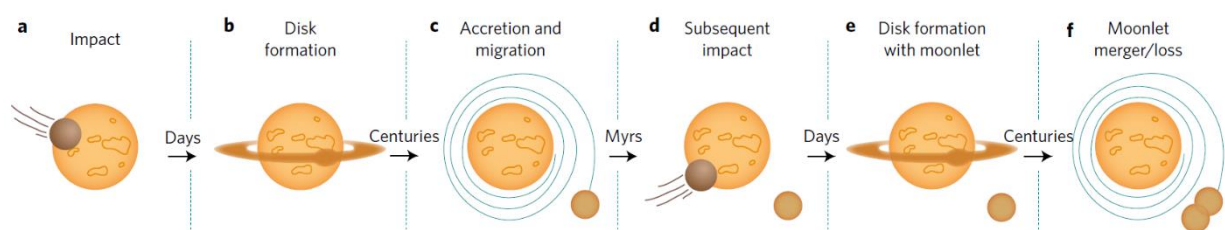


*Figure 3.2: Stages of lunar formation with multiple impactors. A body strikes the early Earth (a), forming a disk of material (b). Over time, this accretes into a moonlet. A subsequent impact (d), repeats the process, forming another disk of material (e). As this material accretes into a new moonlet, the two eventually combine, forming the Moon (from Rufu *et al.*, 2017).*

3.3 The Lunar Magma Ocean

While every planet has undergone a magma ocean stage, the Moon is the body in which this is best preserved. Following the return of lunar samples via the Apollo missions, it was clear that the Moon had undergone silicate differentiation (Smith *et al.*, 1970; Wood *et al.*, 1970). Petrologic, geochemical, and geophysical data all support a theory which holds that following the impact(s) which formed the Moon, the outer portion of the Moon was molten. As this lunar magma ocean (LMO) cooled, olivine, followed by pyroxene, crystallized and sank out (e.g. Snyder *et al.*, 1992). As olivine and pyroxene sank out of the melt, the residual magma became enriched in incompatible elements (e.g. Shearer *et al.*, 2006). At 78% LMO crystallization, low-density plagioclase began to crystallize, rising to the surface of the LMO and cooling into an anorthositic crust (Snyder *et al.*, 1992). The formation of plagioclase removed Eu from the residual melt, creating the widespread Eu anomaly in many lunar rocks (e.g. Taylor 1975).

This primary feldspathic crust is composed of anorthositic rock with a Mg# between 40 and 70, and an An# in plagioclase between 94-98 (Warren *et al.*, 1985; Nyquist *et al.*, 2006). These samples are known as the ferroan anorthosite suite, or FANs.

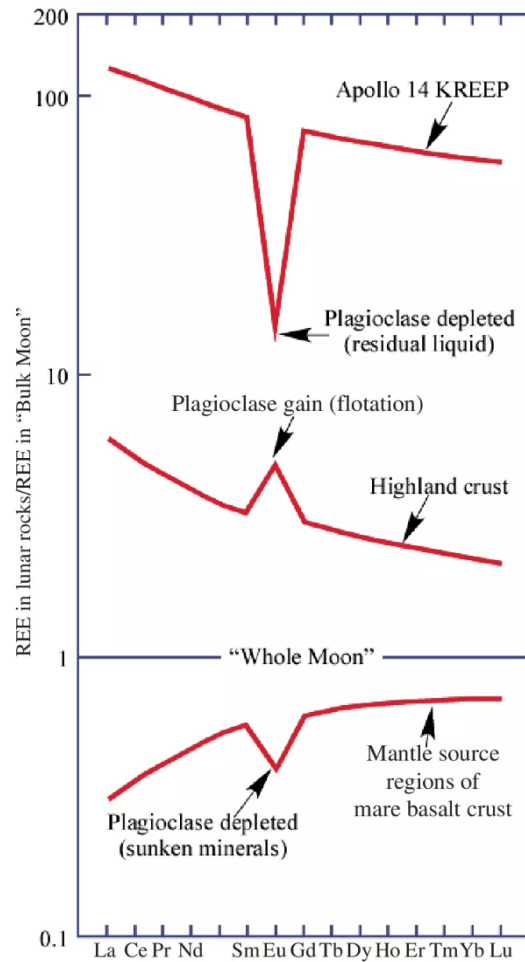


Figure 3.3: Rare Earth element abundances of KREEP and plagioclase, showing the Eu anomaly. The depletion of Eu in KREEP is accounted for by a gain in the plagioclase-rich highland crust. This captures a change in the redox/chemistry of the samples. Plot from O'hara and Niu (2015).

Table 3.1: Stages of equilibrium (through 78%) and fractional crystallization (78%-100%) of the lunar magma ocean (from Snyder et al., 1992)

% Crystallized	Mineral Composition
0-40	Olivine
40-78	Orthopyroxene (with some olivine resorption)
78-86	53% plagioclase, 25% olivine, 22% pigeonite
86-95	38% clinopyroxene, 36% plagioclase, 26% pigeonite
95%+	34% pigeonite, 31% plagioclase, 24% clinopyroxene, 11% ilmenite

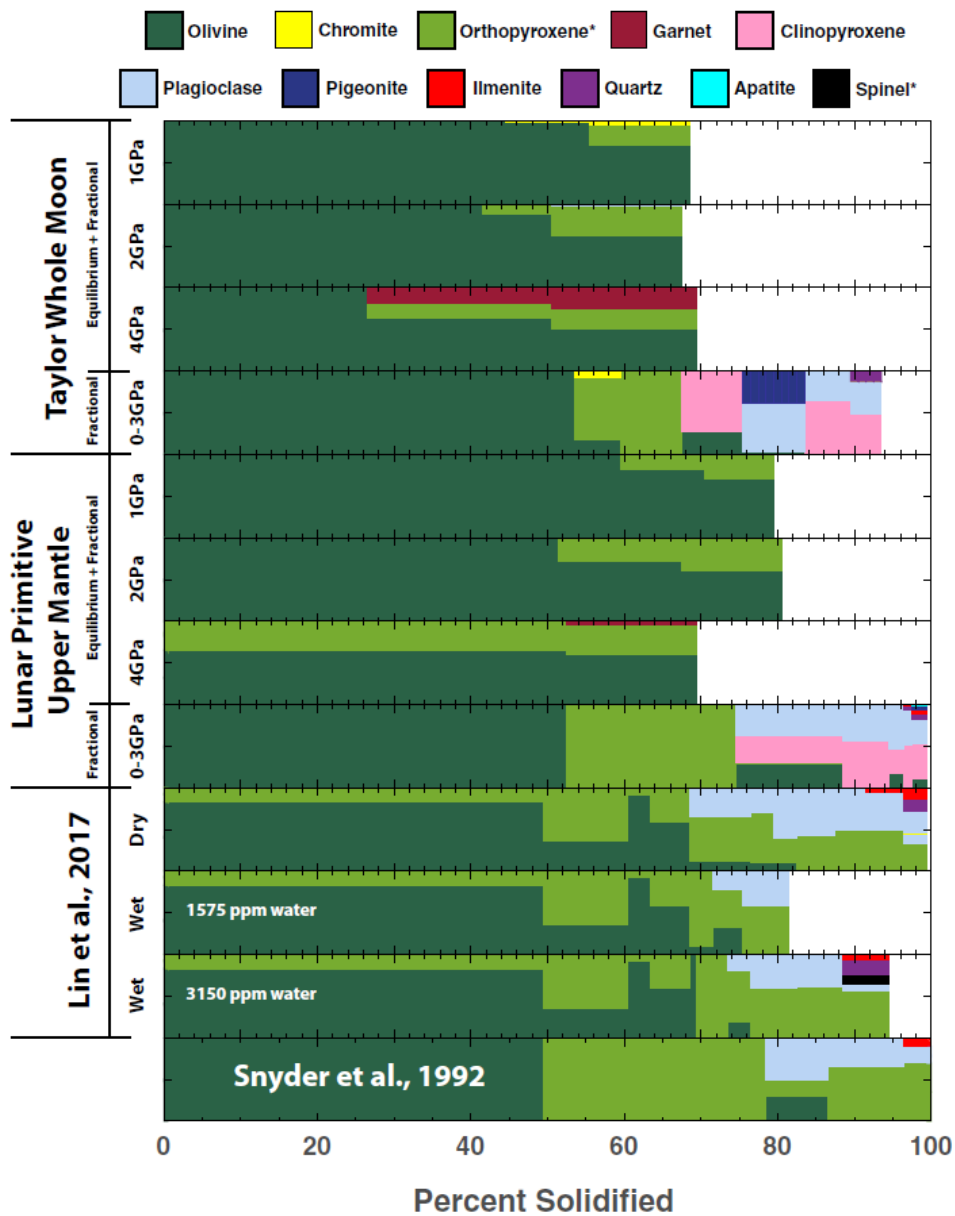


Figure 3.4: Crystallization sequences of Snyder et al., 1992, expanded by Rapp and Draper (2018). This figure compares experimental crystallization sequences and cumulate products with previous results. The equilibrium and fractional data of the lunar primitive upper mantle (LPUM) and Taylor Whole Moon (TWM) are from Elardo et al., 2011. The fractional crystallization results for the TWM are from Rapp and Draper (2012, 2013, 2014, 2016), and the LPUM data from Rapp and Draper (2018). The study by Lin et al., (2017) is a geophysically constrained bulk composition model derived from Khan et al., (2007). From Rapp and Draper, 2018

The remaining fluid had a thermal blanket in the form of the anorthosite crust, slowing the rate of cooling in the remaining LMO (Shearer *et al.*, 2006). This layer became increasingly dense, highly enriched in Fe-O, Th, K, rare earth elements (REE), and P (Warren 1990; Snyder 1992). This unique composition in the residual melt is termed KREEP (Hubbard *et al.*, 1971). This was later modified with the Germanic prefix “ur,” meaning original, as urKREEP to refer to the primary formation of KREEP (Warren and Wasson 1979). Amongst the final crystallization products from this melt was a dense ilmenite-rich (FeTiO₃) cumulate. Apollo 15 and 16 gamma ray spectrometry found a concentration of KREEP on the lunar nearside (Metzger *et al.*, 1973), which was expanded upon with global elemental mapping of the Moon (Lawrence *et al.*, 1998).

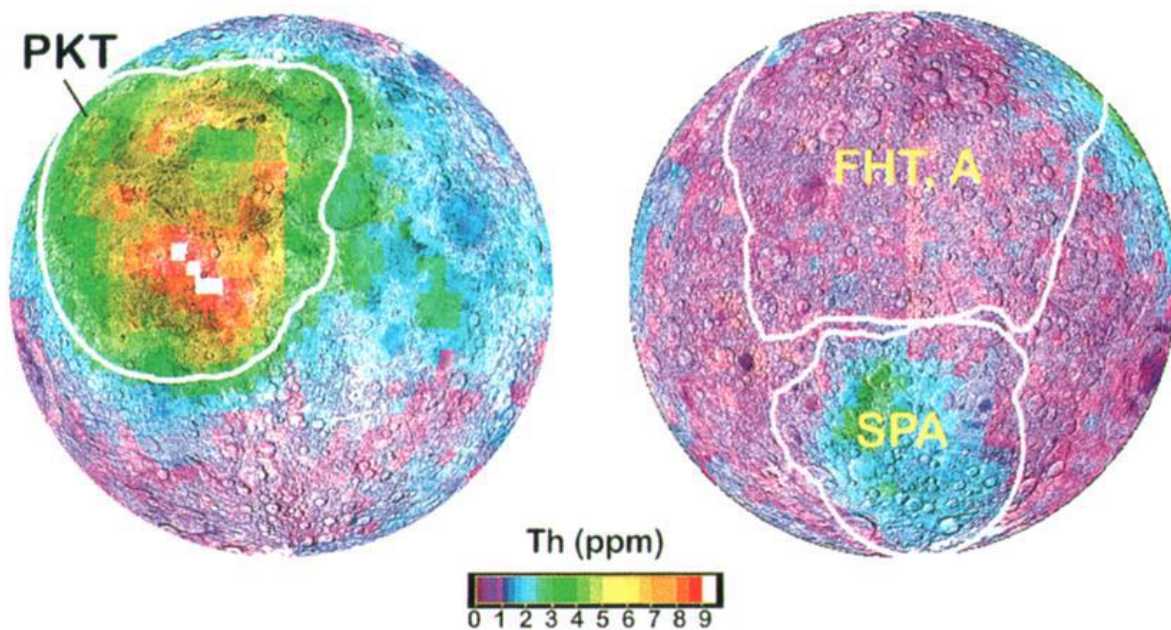


Figure 3.4: Th distribution on the Moon. The highest abundance of Th is found in the Procellarum KREEP Terrane (PKT), while the Feldspathic Highlands Terrane (FHT) is anorthosite rich. South Pole Aitken Terrane (SPA) has an enrichment in Th as well, though not to the degree of the PKT (figure from Joliff *et al.*, 2000).

At this stage, the Moon had formed an outer crust of FAN, with a stratum of a very dense ilmenite-bearing KREEP rich cumulate, atop the less dense olivine and pyroxene layers. Ilmenite would crystalize between 150 and 100 km depth

(Hess and Parmentier, 1995; Van Ormann and Grove, 2000), until KREEP began to crystallize as well. The high-Ti cumulates would have a density between 3700 – 3800 kg/m³, atop mantle cumulates with a mantle density of 3300 kg/m³ (Elkins-Tanton *et al.*, 2002). The density instability led to an overturn, mixing the LMO cumulates into the sources of the surface rocks we now have access to (Kesson and Ringwood, 1976; Beard *et al.*, 1998). The composition of these source cumulates has been modeled based on Lu, Hf, Sm, and Nd isotopic analyses (Unruh *et al.*, 1984; Sprung *et al.*, 2013) and elemental partitioning (Snyder *et al.*, 1992; Fonseca *et al.*, 2014; Leitzke *et al.*, 2016).

Following the formation of the anorthositic crust, the intrusion of partial melts from the lunar interior created secondary crustal rocks, known as the Mg-suite. The intrusion of the Mg-suite has been shown by their being petrogenetic history which is unrelated to that of the FAN crust (Shearer and Papike 2005). The Mg-suite rocks assimilated portions of the KREEP component, giving them a KREEP-like geochemical signature indicative of their formation following the closure of KREEP formation (Gross and Joy, 2016). Geochemical models also show the Mg-suite as being the mixture of early LMO crystallization products which assimilated KREEP during mantle overturn (Hess 1994; Longhi 2003).

The timing of LMO crystallization is a major subject of debate in the lunar community, as it provides a maximum age on lunar formation. The two primary camps hold that the Moon formed “old,” that is, prior to 100 Ma after t_0 , typically ca. 50 Ma (Barboni *et al.*, 2017; Bottke *et al.*, 2015; Jacobson *et al.*, 2014; Yin *et al.*, 2014) or “young,” over 100 Ma after t_0 (Borg *et al.*, 2011; Carlson *et al.*, 2014; Connely and Bizarro, 2016; Snape *et al.*, 2016). Much of this debate centers on the isotope signature of the Moon, and is the crux of two chapters of this thesis.

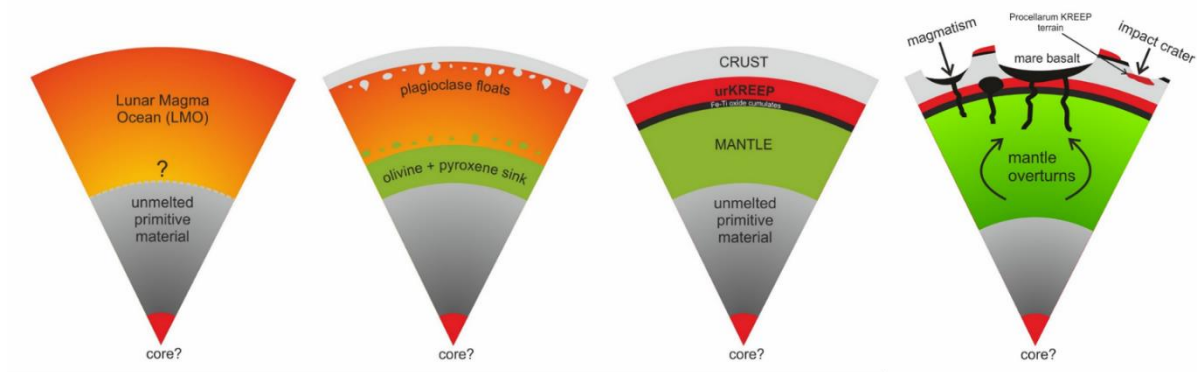


Figure 3.6: Lunar magma ocean differentiation and evolution. A) The post-impact Moon bears an LMO. At this point, and hereafter, the core may exist. Similarly, a degree of unmelted primitive material may be within the lunar interior, the depth and quantity thereof is subject to debate (e.g. Warren and Taylor, 2014). (B) Olivine and pyroxene sink out of the LMO, while plagioclase floats, forming a crust. (C) The final stage, prior to overturn, has the olivine and pyroxene rich mantle, with ilmenite bearing cumulates atop the mantle. Here, the final residue of the LMO, the urKREEP, is also left, under a layer of crust. (D) The density driven mantle overturn begins, and magmatism and impacts alter the visible crust. Figure by R. Fonseca.

While being shorter lived than terrestrial magmatism, lunar magmatism continued beyond the crystallization and later overturn of the LMO. This early volcanism, prior to 4.0 Ga, lead to the deposition of basalt flows which were subsequently covered and obscured by impact craters and their ejecta, known as cryptomare (Head and Wilson, 1992). After 4.0 Ga, effusive volcanism became the primary source of new crust, creating the mare basalts. Around 15% of the lunar surface is covered by partial melts, infilling older impact basins (e.g. Hiesinger and Head 2006). These mare basalts primarily exist on the lunar nearside. Trace element analysis has yielded negative Eu-anomalies in the mare basalts, in contrast to the positive Eu-anomalies of the FAN (Warren 1985; Delano 2009). This would indicate that the mare basalts have formed from a

source which had already formed FAN, leaving the correlative Eu-depletion found in the mare basalts (Warren 1985; Shearer *et al.* 2006; Delano 2009).

Lunar basalts have two main lithologies; mare basalts and picritic glasses (Papike *et al.*, 1998; Shearer and Papike, 1999; Shearer *et al.*, 2006). The mare basalts are classified by their TiO₂ contents, which vary greatly (e.g. Delano, 1986; Papike *et al.*, 1998; Meyer, 2012). These are classified by their weight (wt%) TiO₂: the very-low Ti (< 1 wt%), low-Ti (1 – 6 wt%), and high-Ti (> 6 wt%) (Binder, 1982; Crawford, 2014; Warren and Taylor, 2014 and references therein). The primary Ti-bearing phase is ilmenite, and the ilmenite-bearing high-Ti basalts are primarily confined to Oceanus Procellarum and Mare Tranquillitatis (e.g. Crawford, 2015). Low-Ti basalts are found throughout the nearside Mare, as well as the South Pole Aitken Basin on the farside (Crawford, 2015).

Understanding the history of the Moon via samples is fortunately not limited to the returned samples from the Luna and Apollo missions. The collected samples are all from the lunar near side, and dominated by ejecta from the Imbrium forming impact (e.g. Lawrence *et al.*, 2000). Fortunately, 348 lunar meteorites have been registered to date (Meteorite Bulletin). These meteorites sample portions of the Moon unvisited by scientific missions, providing new geochemical and geographical insights (e.g. Korotev *et al.*, 2003). The majority (ca. 60%) have 3-6% FeO, with high (>20 weight %) Al₂O₃ content and low KREEP compositions, indicating that they are likely sourced from the lunar feldspathic highlands (Calzada-Diaz *et al.*, 2015 and references therein). These lunar meteorites can be further split into three groups based on their Mg# (the molar ratio of magnesium to iron in an igneous rock, Allaby 2008), Magnesian anorthosites (Mg% 65-90), ferroan anorthosites (Mg# 50-68), and the remaining anorthositic lithologies (Gross *et al.*, 2014). These span a range from hyperferroan to highly magnesian.

3.4 Lunar Isotopic Composition

What we know now is that the Earth and Moon are the most closely related bodies in the solar system with regards to $\Delta^{17}\text{O}$ (Wiechert *et al.*, 2001). This is particularly strong evidence for a shared origin of the Earth and Moon given the $\Delta^{17}\text{O}$ between objects of the solar system and their similarities, which are now agreed to be chemical rather than nucleosynthetic in origin (Thiemens and Heidenreich, 1983). The details of what chemical process creates these $\Delta^{17}\text{O}$ is still the subject of debate (e.g. Chakraborty *et al.*, 2013). Higher precision analysis of lunar samples found a ca. 12 ppm difference in $\Delta^{17}\text{O}$ between the Earth and Moon (Herwatz *et al.*, 2014). This was explained as a signature of the Moon forming impactor(s), or the result of material accreted during a late veneer. Similarities between the Earth and Moon extend to other isotopic systems as well. These include K isotopes (Humayun and Clayton, 1995; Wang and Jacobsen 2016), Cr isotopes (Lugmair and Shukolyukov, 1998), Si (Georg *et al.*, 2007), and Ti isotopes (Zhang *et al.*, 2012).

Reconstructing the Moon's history is primarily the subject of radiometric dating. The earliest crustal samples which should be accessible are FANs, but the impact cratering of the lunar surface may reset some of the isotope decay systems one would use. The Sm-Nd decay system is proposed to be the least mobile system in shock metamorphism, and thus most likely to provide accurate dates (Gaffney *et al.*, 2011; Borg *et al.*, 2015). The oldest recorded age from the Sm-Nd decay system was 4.562 ± 0.068 Ga, measured in a FAN clast of lunar sample 67016 (Alibert *et al.*, 1994). Ar-Ar measurements on a different clast from the same sample yield an age of 3.95 ± 0.07 Ga, indicating a post-crystallization thermal event (Turner and Cadogen 1975) that arises from gas loss and associated isotope fractionation. The lack of correlation of old ages in these samples is considered evidence that only the most robust ages are accurate for lunar formation (Borg *et al.*, 2015), inherently biasing arguments on the Moon's age.

The story of W isotopes has proven more contentious, but the ^{182}Hf - ^{182}W short-lived decay system is a key system to understand and calculate the time of lunar formation. The decay of ^{182}Hf to ^{182}W has a half-life 8.9 My (Vockenhuber *et al.*, 2004), making it an ideal dating system for the early solar system. The system is even more ideal, as Hf is a lithophile, while W is moderately-siderophile, allowing the decay system to be used to trace planetary differentiation. The neutron capture of ^{181}Ta creates ^{182}Ta , which through β -decay turns into ^{182}W , but in lunar samples the amount of this cosmogenic ^{182}W is negligible (Leya *et al.*, 2000). Originally measured as being heterogeneous (Lee and Halliday, 1996, Lee *et al.*, 1997), ^{182}W isotope abundances were later suggested to be identical between the Earth and Moon (Touboul *et al.*, 2007). Since then, the precision of W isotope measurements has dramatically improved, allowing for the resolution of a supposedly uniform excess of ^{182}W on the Moon compared to the Earth (Touboul *et al.*, 2015; Kruijer *et al.*, 2015; Kruijer and Kleine, 2017). The proposed homogeneity of the lunar ^{182}W is taken as evidence of lunar differentiation after the extinction of ^{182}Hf (Kruijer and Kleine, 2017), i.e., a so called late-forming Moon scenario. Alternatively, partitioning of the lunar core very early in the solar system's history, while the system is still extant, requires the Moon to have formed within the first ca. 60 million years after solar system formation (Jacobsen 2005), i.e., a so called early-forming Moon scenario. A synthesis of multiple studies, and a new explanation for excess ^{182}W is the subject of chapter 6 of this thesis, in which we provide evidence in favor of an early formation of the Moon within the first ca 60 million years after solar system formation.

The use of ^{182}W is highly dependent on high field strength element (HFSE) abundances in the Earth and Moon. Previous studies (e.g., Touboul *et al.*, 2009; Kruijer *et al.*, 2015) have assumed that the elemental ratios of W, U, and Th are incompatible during igneous processes, and have assumed a Hf/U value (Rocholl and Jochum, 1993) as well as U/W values of the bulk silicate Earth (BSE)

(Newsom *et al.*, 1996) and for the silicate Moon (Palme and Rammensee, 1981) to that effect. However, W behaves more incompatibly than U and Th during terrestrial mantle melting, and to this effect the Hf/W value of the BSE has been revised to 25.8 (König *et al.*, 2011), close to the estimate of 24.9 for Hf/W of the BSE (Münker, 2010). While the incompatible behavior of W during lunar silicate differentiation is well known (e.g. Palme and Rammensee, 1981; Wänke *et al.*, 1974, 1975) the ratio of other incompatible elements with W vary greatly (Münker, 2010). This is due to the less incompatible behavior of W during lunar silicate differentiation (Fonseca *et al.*, 2014; Palme and Rammensee, 1981; Palme and Wänke, 1975). The lunar reducing conditions render W much less incompatible than on Earth (Fonseca *et al.*, 2014), where U and W are both highly incompatible elements. Therefore, the assumption of constant U/W in the Moon is wrong, and leading to previous incorrect estimates of the Hf/W of the silicate Moon (e.g., Touboul *et al.*, 2009; Kruijer *et al.*, 2015; Kruijer and Kleine, 2017).

In this dissertation we have used multiple decay systems (Hf-W-Lu-Hf, Sm-Nd, and Rb-Sr) in order to constrain timing of lunar formation and crystallization of the lunar magma ocean. Radioactive decay systems can be broadly categorized as being “short lived” ($< 10^5$ years) or “long lived ($> 10^5$ years).” A short lived system, such as ^{14}C (half-life $5.73 \pm .04$ ky, Godwin, 1962) is useful in tracing processes in recent history, or while they were still extent, as with the previously discussed ^{26}Al . The Hf-W system (decay of ^{182}Hf to ^{182}W , half-life of 8.9 Ma, Vockenhuber *et al.*, 2004) is a long lived system, though used to constrain events in the early solar system, as it is functionally extinct in the first 60 Ma after SSF. The decay of ^{176}Lu to ^{176}Hf has a half-life of 37.1 Ga (Scherer *et al.*, 2001), allowing for dating of events long after ^{182}Hf is extinct. The decay of ^{87}Rb to ^{87}Sr has a half-life of ca. 49 Ga (e.g., Nebel *et al.*, 2011), and the incompatible nature of Rb means that ^{87}Sr can be used to date the time of closure for a given sample. The decay of ^{147}Sm to ^{143}Nd is particularly slow with a half-life of 106 Ga (Lugmair and Marti, 1978). These systems can all be combined,

however, with mineral isochron dating of natural rocks. For this method, different minerals are separated from a given sample and analyzed for their daughter-element isotope compositions as well as for their mother-to-daughter element ratio. Over time, the initially uniform radiogenic daughter-element isotope compositions increased by an amount governed by the mother-to-daughter element ratio of the respective mineral. The radiogenic isotope compositions of all mineral fractions form a straight line with a positive slope whose value uniquely defines the time that has elapsed since crystallization of the rock.

3.5 From Earth's formation to mantle rocks from the Eifel

Following the formation of the Moon, the Earth also began to cool. A complete history of global differentiation processes on Earth, including the advent of its oceans and the creation of its atmosphere is beyond the scope of this dissertation. More relevant, and field sampling approachable, is the history of the Earth's mantle. The evolution of a terrestrial magma ocean is harder to constrain, with multiple crystallization scenarios leading to the present-day Earth (e.g. Ballmer *et al.*, 2017). Following the magma ocean period, different models hold this age between 4 and 3 billion years (O'Neil, 2016; Condie and Kröner, 2013), plate tectonics began on Earth. While the Moon formed its anorthositic crust and had a mantle overturn, a version of this process is still underway on the Earth. The Earth's crust and the upper mantle are referred to as the lithosphere. The lithosphere is composed of a rigid mass that makes up the outer layer of the Earth and is divided into tectonic plates (Meier, 2016). These plates are in continual motion, leading to subduction beneath one another at active continental margins and island arcs, and the generation of new material along spreading ridges when the plates move apart.

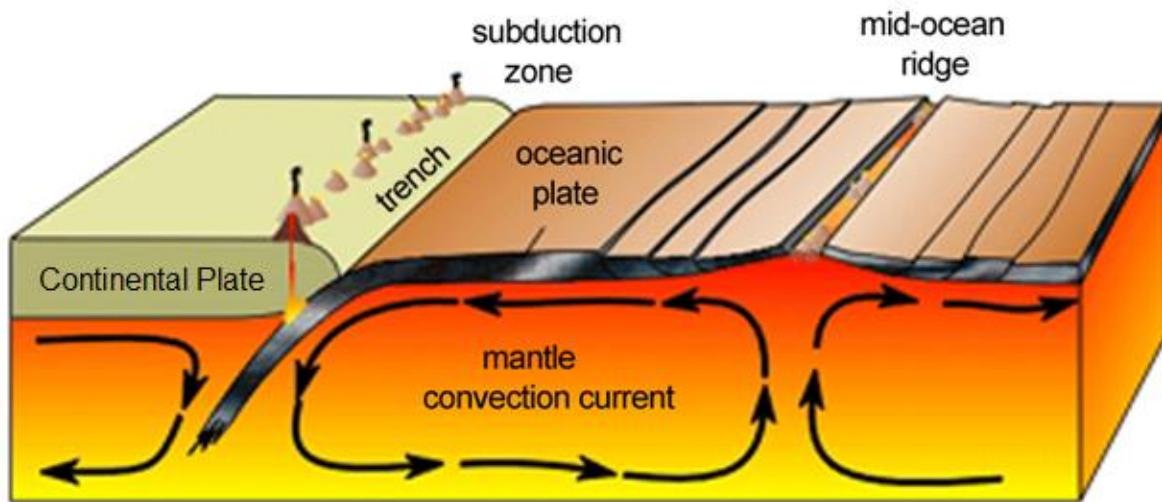


Figure 3.7: The motion process of tectonic plates. The new crustal material is generated at the mid-ocean ridge, while the plate subducts beneath another plate, here continental, at the subduction zone. source: heritage.nf.ca/articles/environment/geology.php

The movement of the tectonic plates has created and broken up multiple “supercontinents,” in which most continental crust combines to make a single landmass (e.g. Bedard, 2018; Wegener, 1912; Kroner and Romer, 2013). The most recent supercontinent was Pangaea (Wegener, 1912). It was formed during the collision of two previous continents, Gondwana (Suess, 1892) and Laurasia, in an event known as the Variscan orogeny (Kossmat *et al.*, 1927; Kroner and Romer, 2013). This collision was the major mountain forming event in central Europe, lasting from the late Devonian (360 Ma) to the late Carboniferous (300 Ma) (Suess, 1885; Kossmat, 1927). This means that central Europe is one of the places with the best record of Pangaea’s formation, as well as intra-plate volcanism.

This collision was also the event which formed the Rhenish Massif, an uplifted plateau in what is now central Europe (Kroner and Romer, 2013; Garcia-Castellanos *et al.*, 2000; Wegener, 1912; Suess, 1885; Kossmat, 1927), which makes central Europe a unique/suitable location to study Earth’s geological history. The Rhenish Massif has undergone multiple compressional and decompressional stress and strain events since its origin, as well as continual erosion (Kroner and

Romer, 2013; Illies *et al.*, 1979; Königshof *et al.*, 2016). The compressional tectonic activity was replaced by extensional tectonics during the Permian (300-250 Ma) (van Wees *et al.*, 2000; Meier *et al.*, 2016 and references therein). In the Mesozoic, peaking in the Eocene (50-30 Ma), a new rift system along the main strike directions NW-SE and SSW-NNE caused volcanic activity (Ziegler *et al.*, 1992).

The cause of volcanic activity in central Europe is a central research theme (Regenauer-Lieb, 1998). Researchers have found evidence, particularly through the Mesozoic and Cenozoic, for episodes of lithospheric thinning leading to surface uplift and volcanism (Ziegler *et al.*, 1992; Regenauer-Lieb, 1998; Meier *et al.*, 2016 and references therein). The uplift brought the Rhenish Massif to an average height of 300m above sea level, similar to other central European Paleozoic blocks (Illies *et al.* 1979; Schmincke *et al.*, 2007). Volcanism has also been suggested as the consequence of major plume activity beneath central Europe (Ritter *et al.*, 2001; Hoernle *et al.*, 1995, Duncan *et al.*, 1972), though later studies have suggested that the plume is a modeling artifact (Meier *et al.*, 2016).

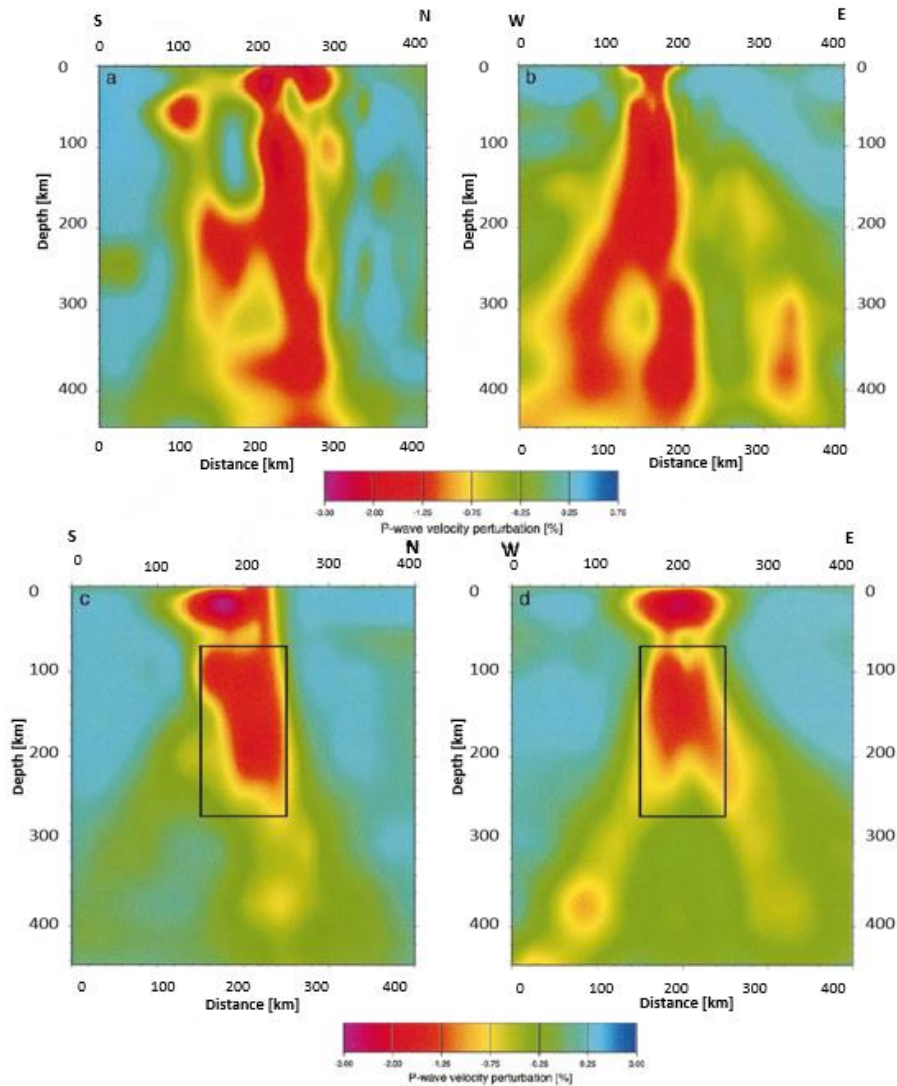


Figure 3.8 Low velocity zones beneath the Eifel volcanic field (red), showing a columnar low P-velocity anomaly in the upper mantle. This was suggested as evidence of a plume, but was later suggested to be a measurement of partial melting (Meier *et al.*, 2016). Illustrated by Ritter *et al.*, 2001

Research into mantle evolution has heretofore been mostly limited to geophysical investigations such as seismic refraction profiles (e.g. Meier *et al.*, 2016; Ritter *et al.*, 2001). However, geochemical approaches have been made by several authors (e.g. Mertes and Schmincke, 1985; Schmincke and Mertes, 1979; Schmincke *et al.*, 1999; Witt-Eickschen *et al.*, 1993; Witt-Eickschen and O'Neill, 2005; Meier *et al.*, 2015). As the lithosphere beneath the Rhenish Massif has undergone multiple metasomatic events, the Eifel, the most recently active

volcanic area on top of the Rhenish Massif is a major focus of this study. Together with the Massif Central, the Eifel volcanic field is central Europe's youngest volcanic field, lying at the west end of a 350 km long volcanic belt, west of the Rhine River and north of the Mosel River (Schmincke *et al.*, 2014; Wilson and Downes, 2006). The Eifel volcanic fields are divided into the Quaternary West Eifel Volcanic Field (WEVF) and East Eifel Volcanic Field (EEVF) and the Tertiary Hocheifel Volcanic Field.

The Rieden complex (430-360 ka), the Wehr volcano (>215 ka), and the Laacher See (12.9 ka), are the three largest volcanic complexes of the EEVF (Schmitt *et al.*, 2010). Evidence for high pressure magma fractionation near the crust/mantle boundary, high temperature overprinting of basement rocks, as well as mantle metasomatism are typical features found in EEVF rocks (Schmincke *et al.*, 2007). The WEVF covers an area of about 500-600 km² (Schmincke *et al.*, 2014). Volcanic activity initiated less than 700 ka, and has increased in the last <100ka (Schmincke *et al.*, 2014). The magmas of the Quaternary Eifel volcanism are mostly SiO₂ undersaturated, mafic with a high abundance of MgO and FeO (Mertes and Schmincke 1983) and foiditic, K-rich with K₂O > Na₂O. Typical lavas contain about 30% phenocrysts of clinopyroxene, olivine, phlogopite or titanomagnetite (Schmincke *et al.*, 2007).

The continued renewal of Earth's surface by plate tectonics and active volcanism makes determining its primordial history difficult. The advantage of plate tectonics, however, is that it allows for direct analysis of mantle rocks because of intraplate volcanic activity that causes deep mantle material to rise and accumulate within magma chambers. Volcanic eruptions then cause the material to be exposed to the surface. Peridotites are igneous rocks composed of pyroxene and olivine, and are the dominant rocks of Earth's upper mantle (above 400 km depth). Nodules of peridotite can be found as xenoliths in basalts, therefore allowing direct analysis of rocks from the Earth's mantle. Peridotites

are divided into four types by composition. Lherzolites are the most common form, and are dominated by olivine, clinopyroxene, and orthopyroxene. Harzburgite and Wehrlite are peridotites composed primarily of olivine plus orthopyroxene and clinopyroxene, respectively. Dunite, the fourth type, is composed almost exclusively by olivine. Peridotite xenoliths provide evidence for the evolution of the lithospheric mantle beneath the Eifel. Several authors have published isotope studies (e.g. Witt-Eickschen *et al.*, 1993, 2003, 2005; Stosch and Lugmair, 1986), but the geologic history of the xenoliths and in particular the timing of metasomatic events remain unclear. Recently developed methods for isotope measurements can provide a more precise chronology. The analysis of peridotites related to the Variscan orogeny and its subsequent volcanism will be discussed in chapter 4.

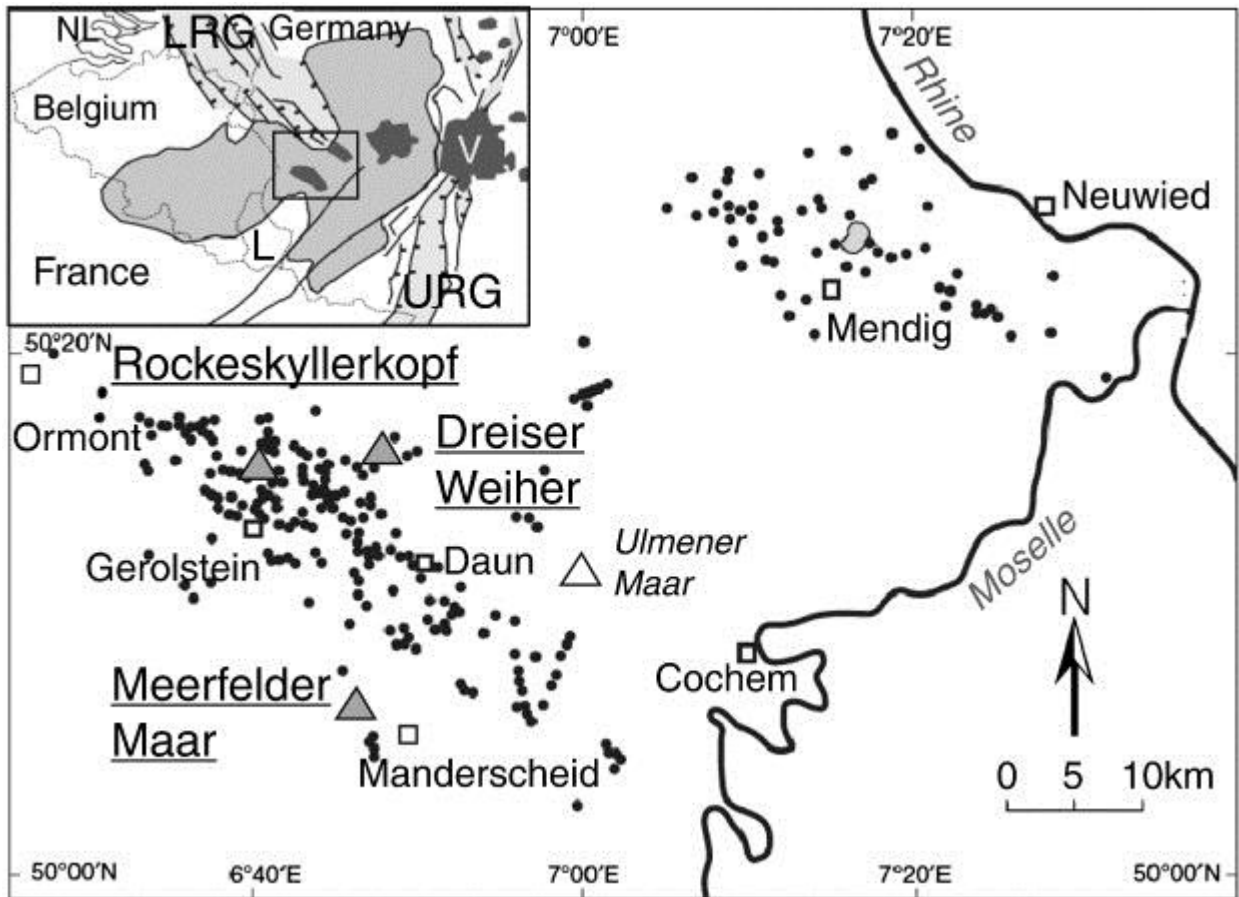


Figure 3.9 The location and distribution of volcanic centers in the Eifel volcanic field. Xenolith bearing localities (triangles) and towns (squares) are delineated (from Denis *et al.*, 2013)

3.6 Motivation and Objectives

As discussed, the Earth-Moon system and its evolution is an exceedingly complex system to unravel. Even a planetary body as “simple” as the Moon has had a complex history, with multi-disciplinary studies helping to create the image of the Moon as it stands today. There still stand large gaps in our knowledge with major points of contention amongst cosmochemists related to how one approaches the formation, timing, and evolution of the Moon and how to interpret the experimental data. Many cosmochemical studies on the Moon assume terrestrial behavior for element partitioning, so the combination of partitioning data with chemical would offer a fresh look. As the number of studies

on the Moon are fundamentally limited by the available samples, the small amount needed for our high precision methods made the Moon an excellent target for analysis.

Our overall goal was to study planetary formation and evolution using a diverse range of methods, including element partitioning and isochrons. Mineral isochron dating of ultramafic samples is challenging, because the concentrations of the elements of interests are all very low in mafic minerals such as olivine or orthopyroxene. We tested this method on terrestrial samples, i.e., on mantle xenoliths from the Eifel, in order to ensure analytical fidelity. Results are presented in **chapter 4**. The initial goal was to test the boundaries of what we could measure in terms of reproducibility, blank propagation, and minimum sample size.

Our scientific aim here was to see if we could learn anything new about the chemical signature of the Mantle underlying Europe. We measured peridotite xenoliths from Meerfelder Maar and Dreiser Weiher multiple times, each time using a different ion exchange recipe to produce pure analytes of the involved elements for mass spectrometric measurements. These samples had been deposited in Olivine Nepheline Basalt-suite host basalts (one of two suites in the WEVF) in the quarternary (< 0.7 Ma). We separated each mineral from the peridotites (ol, opx, cpx) for the purpose of isochron dating, and each aliquot was analyzed for all 6 parent and daughter elements from the 3 long-lived radiogenic isotope systems. Here, the robustness and intrinsic pitfalls of the systems in question are all on display, as we see the ease with which they can be thermally reset, as well as their capacities to provide information about multiple stages of the geological evolution of the same sample. While the peridotites all yielded ages correlating with quarternary volcanism (functionally modern ages), of interest is that the whole rock fraction often did not plot on the isochron line. This implies melt infiltration of the whole rock, which is excluded by the process

of mineral picking. The whole rock fraction did not form a mixing line between host rock and mineral separates, indicating that the infiltrating agent was not sourced from the host rock.

The data are supplemented by work conducted for a BSc thesis (Gerritzen, 2018) which was supervised by the author of this thesis. Data by Gerritzen (2018) are incorporated into the broader framework of this thesis, and these individual data are highlighted in chapter 4. The key result of the mineral isochron dating of Eifel xenoliths is that most measured peridotites are reset by most recent geological events that presumably predate the eruption of their quaternary basaltic host lavas. One specific peridotite sample from Dreiser Weiher, however, provides a far more compelling history, as each isotope decay system records a different age pattern. While Lu-Hf yields a modern age, possibly indicative of the sample deposition, the highly radiogenic Hf signature (ϵ_{Hf} of 37.0) allowed for the calculation of depletion model ages. Using depleted mantle (Vervoort and Blichert-Toft, 1999) and CHUR (Bouvier *et al.*, 2008) as the minimum and maximum values, we found a source age for the xenolith between 1.22 – 1.76 Ga, in agreement with the 1.6 Ga model age found with Re-Os analysis (Schmitt and Snow, 2002). The Sm-Nd dating gave an age of 236 ± 110 Ma, which overlaps with the Variscan orogeny (e.g. Kroner and Romer, 2013). Rb-Sr yielded an age of 635 ± 110 Ma, which does not necessarily bear geological significance, but correlates with a mantle heating event which had been previously suggested by Sm-Nd studies at 560 Ma (Stosch *et al.*, 1980; Paul *et al.*, 1971).

We extended this method to the lunar meteorite NWA 6950 with the aim of learning more about the evolution of the Moon. The NWA 6950 meteorite is part of the so called NWA 773 clan (coupled meteorite finds), a group of mafic-ultramafic cumulates from the lower lunar crust. Meteorites of the NWA 773 clan are the youngest set of KREEP rich lunar samples, but Sm-Nd and Rb-Sr dating studies (ca. 2.9 Ga, Borg *et al.*, 2009) have given different age information than

obtained by the Ar-Ar (2.8 Ga, Fernandes *et al.*, 2003) and Pb-Pb methods (3.1 Ga, Shaulis *et al.*, 2017). We prepared mineral separates of the meteorite NWA 6950, and combined Lu-Hf with Rb-Sr and Sm-Nd measurements in order to constrain the formation of this meteorite clan, with the broader goal of developing greater insights into KREEP evolution and formation. Our results, presented in chapter 5, found the Lu-Hf system ($3.103 \pm .045$ Ga) to corroborate Pb-Pb ages (average 3.180 Ga), while the other systems (Rb-Sr and Sm-Nd) yield a more complicated picture. We used the initial Hf isotope composition of NWA 6950 ($\epsilon_{\text{Hf}} -12.5 \pm 0.6$) to expand the Hf isotope evolution line of KREEP to unprecedentedly young ages. The result show that, unlike the assumption of previous studies (e.g., Borg *et al.*, 2009; Gaffney and Borg, 2014), rocks of the Mg suite cannot be used to estimate the Hf evolution line of KREEP which evolved along more unradiogenic values. Using the revised Hf isotope evolution line for KREEP, formation of the KREEP reservoir and by inference crystallization of the Moon can now be dated back to 4.514 Ga, ca. 50 Ma after solar system formation.

Our final goal was to learn about the earliest history of the Moon. To achieve this goal, we mapped the elemental behavior of lunar samples to constrain the lunar magma ocean time scale and mechanism, as presented in chapter 6. This is, in part, to help settle the ongoing strife between the two camps on lunar formation. We measured 29 samples from the Apollo missions for the concentration of high field strength elements HFSEs by isotope dilution. The work by Leitzke *et al.*, (2016) enables us to address further compositional dependencies relevant for the partitioning behavior of trace elements during lunar silicate differentiation. Key to this study is the Ti content of the melt. We combined our high accuracy analyses with these novel experimental data to constrain HFSE behavior in the early Moon. The HFSE, such as Hf, W, U, and Th, are used to constrain timescales for the differentiation of planetary bodies, as the difference in behavior between siderophile and lithophile elements combined with a decay system (as previously described with the ^{182}Hf - ^{182}W decay system)

allow tracing of a planet's evolution. Our results found strong support for cumulate source melt models, with most sample group showing astonishing intra-group homogeneity for Hf/W and U/W (e.g., low-Ti mare basalts from Apollo 12 varied by ± 3 and ± 0.1 , respectively. Amongst the Apollo 17 high-Ti mare basalts we found a larger range of Hf/W (from 125 to 145). We modeled a source mineral assemblage based on Hf and Nd isotope systematics from previous studies (Fonseca *et al.*, 2014; Leitzke *et al.*, 2016; Sprung *et al.*, 2013). We found that partial melting of this source explained the range we measured in the high-Ti basalts. Our data also showed the independence of the KREEP forming source from other cumulate sources, as the KREEP-rich sample have a large range of U/W values (from 0.5 to 3.5) at sub-terrestrial Hf/W (< 25). Our high accuracy Hf and W analyses were combined with literature ^{182}W data (Kruijer *et al.*, 2015; Kruijer and Kleine, 2015) to provide a range of dates for lunar formation between 44 and 60 Ma after SSF, finding further support for an old Moon formation. In this thesis we have found evidence for an old Moon from two independent isotopic approaches.

4.0 Isotopic investigations of peridotites from the West Eifel Volcanic Field

*When faced with a problem you do not understand,
do any part of it you do understand,
then look at it again.*

The Moon is a Harsh Mistress

By R. Heinlein

1966

4.1.0 Introduction

4.1.1 Background

The configuration of the Eurasian plates during the Variscan orogeny forms the fundament on which the Central European lithosphere evolved (e.g. Ziegler and Dézes, 2006; Schulmann *et al.*, 2014). As such, areas of central to western European intraplate volcanism during the Cenozoic are intimately linked to extensive structures within and regional uplift of the Variscan basement. These tectonic movements are the result of the collision of Africa and Eurasia during the Alpine orogeny (Kossmat *et al.*, 1927; Kroner and Romer, 2013; Wilson & Downes, 1991; Wilson & Patterson, 2001) causing decompressional melting in the mantle that might have been added to by a possible mantle plume activity (e.g. Granet *et al.*, 1995; Hoernle *et al.*, 1995; Regenauer-Lieb *et al.*, 1998). Central Europe's topography is dominated by uplifted blocks of Variscan basement, including the Rhenish Massif, a massive block of mainly Devonian to lower Carboniferous rocks in Central West Germany. The Massif formed during the Variscan Orogeny of the late Devonian to Early Carboniferous (ca. 360-320 Ma), during the collision of Gondwana and Laurussia (Kossmat *et al.*, 1927; Kroner and Romer, 2013; Ziegler *et al.*, 2006). The compressional tectonic activity was followed by extensional tectonics and basin evolution during the Permian (300-250 Ma) (Meier *et al.*, 2016 and references therein; van Wees *et al.*, 2000).

A new rift system along the main strike directions NW-SE and SSW-NNE formed during the Mesozoic (Regenauer-Lieb *et al.*, 1998; Ziegler *et al.*, 1992). The oceanic lithosphere subducted during the Alpine orogeny disengaged from the continental lithosphere and sank into the asthenosphere. Rising hot asthenospheric material heated the continental lithosphere, which thinned out as a thermal process, triggering volcanism in Central Europe north of the Alps (Wilson and Downes 1992; Ziegler *et al.*, 1992). The Cenozoic volcanic activity

along the Mesozoic extension lines is often collectively called the Central European Volcanic Province (e.g. Meyer and Fougler, 2007). It covers areas in Lower Silesia, within the Bohemian and Rhenish Massif, in the vicinity of the Black Forest and the Vosges as well as in the Massif Central (Lustrino & Wilson, 2007; Regenauer-Lieb *et al.*, 1998; Wilson & Downes, 1991; Ziegler *et al.*, 1992). Within southern Germany, several centers of volcanic activity between ca.45 Ma and sub-recent times comprising the Eifel, the Upper Palatinate, Heldburg, Westerwald, Siebengebirge, Rhön, Vogelsberg, the Hessian Depression, the Kaiserstuhl, and Hegau in order of the oldest occurrences (see compilation in Jung *et al.*, 2012). Noteworthy, many of these fields show long-lasting or intermittent activity, with two primary phases dating from the Oligocene to Miocene, and Pliocene to modern age (Lustrino and Wilson, 2007).

The focus of this study is on peridotite xenoliths from the West Eifel volcanic field (WEVF). In the greater vicinity of this field, the Hocheifel formed within the Rhenish Massif over two periods of volcanic activity during the Eocene, from 44-30 Ma and 37-35 Ma (Fekiacova *et al.*, 2007; Fuchs *et al.*, 1983; Schmincke *et al.*, 2014; Wilson and Downes 2006). The younger, Quarternary Eifel volcanic fields can be broadly divided into the West Eifel volcanic field (WEVF) and the East Eifel volcanic field (EEVF) which formed since ca. 0.7 Ma. Following its formation, the WEVF has undergone multiple volcanic events, up to as recently as 11 ka ago (Ulmener Maar: Zolitschka *et al.*, 1995) the most prominent of which is the Laacher See eruption which produced an almost Europe-wide tuff horizon (Schmincke 2008; 2013). West and East Eifel volcanism comprised very primitive to highly differentiated varieties (Mertes and Schmincke, 1985), a good summary of which can be found in Schmincke (2007). Within the rocks of the western WEVF clinopyroxenite and mantle peridotite xenoliths frequently occur (e.g., Shaw *et al.*, 2005). Of the latter, hydrous and anhydrous varieties are known and both groups encompass dunites, lherzolites, harzburgites, and wehrlites (e.g., Stosch and Seck, 1980). In contrast to most

previous studies that investigated the evolution of the lithospheric mantle beneath the Eifel by means of peridotite xenoliths (e.g., Stosch and Seck, 1980; Witt-Eickschen *et al.*, 1993; 1998; 2003; Witt-Eickschen and Kramm, 1998; to name a few) we here exclusively focus on samples that visually appear vein-free. These previous studies found evidence for several heating events in the mantle at ca. 560 Ma (Stosch *et al.*, 1980; Paul *et al.*, 1971), 100-150 Ma (Witt-Eickschen *et al.*, 2003), as well as due to Quaternary volcanism (Ritter *et al.*, 2001).

Within the WEVF are the Dreiser Weiher and Meerfelder Maar localities. Dreiser Weiher is a young (ca. 11.7 ka) Pleistocene maar-type volcano, located at the east-central part of the WEVF (Stosch *et al.*, 1980). Meerfelder Maar is located to the southwest of the WEVF, 18 km south of Dreiser Weiher (Witt-Eickschen *et al.*, 1998). Meerfelder Maar is a maar-type volcano with an eruption age of ca. 45 ka (Schmincke *et al.*, 2014).

Here, we aim to discern evolutionary episodes within the lithospheric mantle beneath the West Eifel via a multi-system, isochron approach utilizing the Rb-Sr, the Sm-Nd, and the Lu-Hf system. Vein-free xenolithic peridotite samples from two renowned and well-studied locations of Quaternary volcanic activity – Dreiser Weiher and Meerfelder Maar – are investigated. With vein-free samples promising to be the least complex, metasomatic overprint, recrystallization, or diffusional resetting might not have obliterated all primary depletion information. A particular focus is given to which constituents of the peridotites, i.e., minerals or grain boundaries, might hold distinct information.

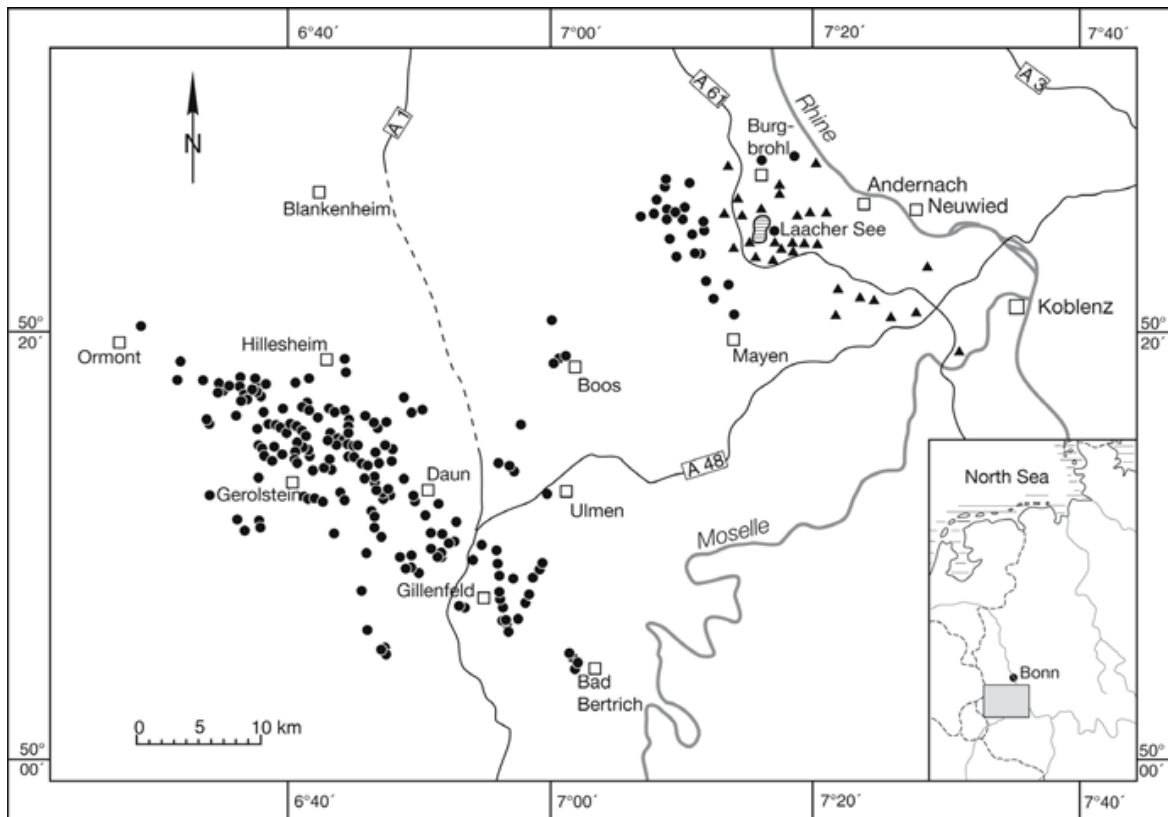


Figure 4.5: The eruptive centers of the Eifel volcanic fields (WEVF, EEVF). The youngest centers (215 ka) are shown in triangles (from Schmincke 2007).

4.1.2 Geological Setting

Whether as the consequence of a mantle plume or crustal thinning, the past 700 ka have seen volcanism throughout the Eifel. The WEVF itself is dominated by 240 volcanoes comprising ca. 2% pyroclastic vents, 2% scoria rings, 30% maars and tuff rings, and 66% scoria cones (Mertes 1983; Büchel and Mertes 1982; Schmincke 2014). Within the WEVF, magmatic activity begetting lava flows focused on the north-west section of the WEVF beginning ca. 700 ka (Mertz *et al.*, 2015). Magmatic activity originated in the north-west of the WEVF and migrated southeast (Schmincke, 2014). There are two major episodes in the past 700 ka: one at 480 ka, the other 80 ka, which are characterized distinctly by their different chemical compositions. The older of these bears higher radiogenic

Sr and H₂O/Na₂O than the more recent events. Typical basalts bear 30% phenocrysts of clinopyroxene (CPX), olivine (Ol), phlogopite, or titanomagnetite (Schmincke, 2007).

A highly enriched leucitite- (melilite) – nephelinite suite (F) dominates in the older part of the WEVF, and two ol-rich very mafic sodic suites are restricted to the younger WEVF (basanite (B) and olivine nephelinite (ON)), collectively referred to as the ONB-suite (Frechen and Thiele, 1979; Mertes and Schmincke, 1985; Mertz *et al.*, 2015; Schmincke *et al.*, 2007). These suites cover compositions ranging from very primitive to highly differentiated (Mertes and Schmincke, 1985). The basalts of the region are mafic, with high MgO and FeO contents. The F-suite is K enriched (bearing a K₂O/Na₂O ratio > 1), while the ONB-suites are sodic lavas (K₂O/Na₂O ratio < 1) (Mertes and Schmincke, 1985). The F-suite has high CaO and K₂O, as well as Rb, Ba, and LREE contents but lower concentrations of Al₂O₃, Na₂O, Sr, and Ni than the ONB-suite. The ONB suite represent the most primitive suite of the Quaternary Eifel magmas. Isotopically, the ONB-suite exhibits typical ⁸⁷Sr/⁸⁶Sr of ca. 0.7039 and ¹⁴³Nd/¹⁴⁴Nd between 0.5128 and 0.51285, while the F-suite lavas have ⁸⁷Sr/⁸⁶Sr > 0.7041 and ¹⁴³Nd/¹⁴⁴Nd below 0.51285 (Wörner *et al.*, 1986).

Of note are the basalts of Dreiser Weiher and Meerfelder Maar, the sample sites for this study, which have been previously suggested to be members of the ONB-suite (Witt-Eickschen *et al.*, 1998; Stosch and Lugmair, 1986). Specifically, Dreiser Weiher has been identified as a basanite (Stosch and Lugmair, 1986) while Meerfelder Maar is olivine-nephelinite (Witt-Eickschen *et al.*, 1998). As these samples have ⁸⁷Sr/⁸⁶Sr > 0.703920 and ¹⁴³Nd/¹⁴⁴Nd > 0.512800, they clearly fall within the range of the ONB suite.

It has been suggested that the magmas formed in the garnet-spinel peridotite field (>70km depth) (Mertz *et al.*, 2015). The magmas are thought to have sourced from a depleted asthenospheric and enriched lithospheric sources

(Schmincke, 2007; Mertz, 2014; Witt Eickschen 2003; Wörner and Wright, 1984; Wörner *et al.*, 1986). The enriched lithospheric source is less agreed upon, and is thought to be either phlogopite or amphibole-bearing lithospheric mantle metasomatized by multi-stage magmatic processes prior to the eruption (e.g. Witt-Eickschen *et al.*, 2003; Mertz *et al.*, 2015). Alternatively, it has been suggested that the lithospheric source is part of an uprising mantle plume consisting of asthenospherically derived phlogopite-garnet-spinel peridotite (e.g. Witt-Eickschen *et al.*, 2003; Shaw *et al.*, 2005; Shaw and Woodland, 2012).

The peridotite xenolith suites of the WEVF contain spinel peridotites with modal CPX between 2-20% (Seck and Wedepohl 1983; Schmincke 2007; Witt-Eickschen *et al.*, 2003). These are found throughout the mafic alkaline magmas of the quarternary WEVF, particularly Dreiser Weiher and Meerfelder Maar (Witt-Eickschen, 2007 and references therein). CPX-poor lherzolites and harzburgites are the dominant forms of peridotite. The peridotites of the WEVF have been suggested to represent ancient (1.6 – 2.0 Ga old) depleted mantle (Schmidt and Snow, 2002; Stosch *et al.*, 1986). These are high temperature peridotites, with equilibrium temperatures between 1100-1160°C. The peridotites from Dreiser Weiher can also contain Ol-CPX as veins, thought to be the result of Quaternary volcanism, given the compositional similarities between them and WEVF lavas (Witt-Eickschen and Kramm, 1998). Mantle metasomatism which can cause chemical alterations to xenoliths, beginning with transport processes (Rudnick, 1993) or their carrier fluids during transport (Ehrenberg and Griffin, 1979; Emery *et al.*, 1985; Griffin *et al.*, 1979; Padovani *et al.*, 1982; Rogers, 1977; Rudnick and Taylor, 1987; Ruckers and Hawkesworth, 1982). Partial melting along grain boundaries can also occur (Garvey and Robinson 1984; Jones *et al.* 1983; Padovani and Carter 1977).

The xenoliths (peridotites) in the Dreiser Weiher xenolith suite were previously reported to represent possibly ancient (1.6 – 2.0 Ga) depleted mantle

(Schmidt and Snow, 2002; Stosch *et al.*, 1986). These xenoliths were later modified by multiple metasomatic processes which may have occurred between ca. 560-550 Ma (Paul *et al.*, 1971; Stosch *et al.*, 1980), in the early Cretaceous (150 – 100 Ma) (Witt-Eickschen *et al.*, 2003), or up to the Quaternary (Stosch *et al.*, 1980), possibly associated with the Quaternary eruption of lavas in the WEVF.

4.2.1 Methods and Samples

The analyzed peridotites originated from the Dreiser Weiher and Meerfelder Maar localities in the WEVF. The peridotites from each site were mechanically separated into their constituents, i.e., chromium diopside (CPX), olivine, spinel (Sp), and pyroxene. We also analyzed the host rock basalt (HR) and whole rocks (WR) alongside the mineral separates, performing both low pressure hotplate digestions in Savillex vials at 120°C for 24h and high pressure digestions in Savillex vials inside Parr autoclaves at 180°C for 5 days on them. Acid amounts for digestion were varied to accommodate different weighted in mineral masses. Generally, cHNO₃ and cHF were used in a proportion 1:1. Samples were spiked with mixed ¹⁴⁹Sm-¹⁵⁰Nd, ⁸⁷Rb-⁸⁴Sr, and ¹⁷⁶Lu-¹⁸⁰Hf tracers prior to digestion. Sample digestions and ion exchange chromatography were performed in the clean labs at Cologne.

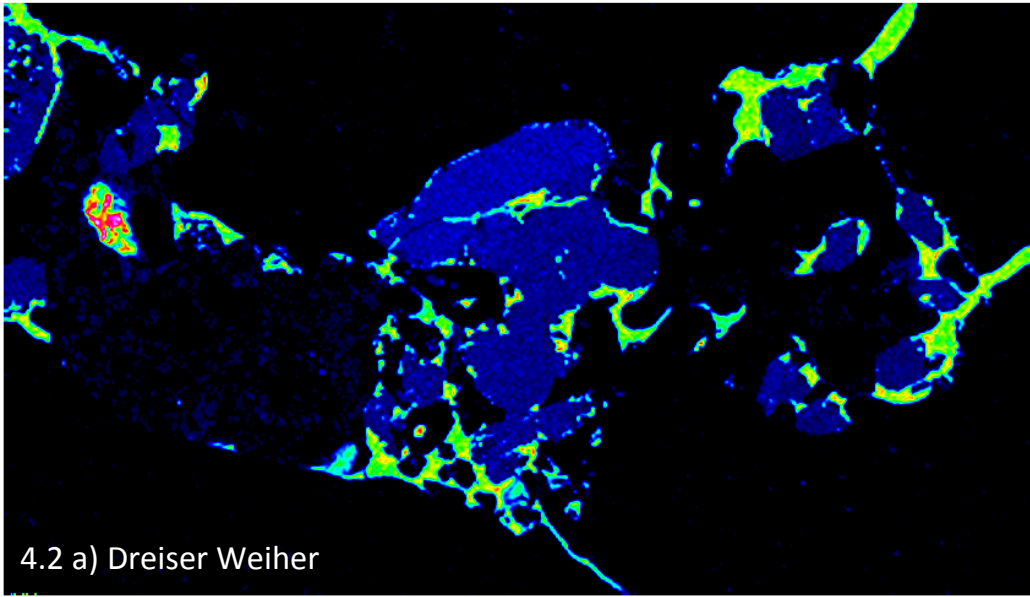
For this study we used three different separation protocols, with the goal of ensuring that we would be able to analyze our elements of interest in samples similar to those found on the Moon (chapters 5 and 6). The first separation protocol was based on Münker 2010, the second on Sprung *et al.* (2013), and the final is based on Bast *et al.*, 2015. The most important modification compared to the Bast *et al.* method is the use of HCl-H₂O₂ instead of HCl-HF as a loading agent on the first (Ag50Wx8) exchange column. This modification enables direct loading of the HFSE-Ti-cut onto the subsequent In resin column on which Ti and Zr are separated from Hf without any previous drydown. The chemically pure

samples were analyzed on the Cologne/Bonn Thermo Fisher Scientific Neptune MC-ICP-MS. Rock standards AGV-2 and BHVO-2 were analyzed alongside the samples, and agreement with literature values provided evidence of method fidelity. Thin section analyses for visual evaluation of element distributions within the peridotites were performed on the University of Bonn JEOL Superprobe JXA 8200. Distribution maps for Mg, Al, Fe, Ca, Mn, Na, Si, Ti, Cr, were obtained with a beam current of 80 nA and an acceleration voltage of 15 kV.

4.3.0 Results

4.3.1 Microprobe Analysis

Results of microprobe element distributions maps across typical grain boundaries in the central areas of the samples are given in Figure 4.2. A general trend towards enrichments of incompatible elements along grain boundaries can be observed for instance from the distribution of Na with mineral grains generally showing a homogenous appearance with respect to incompatible element distributions.

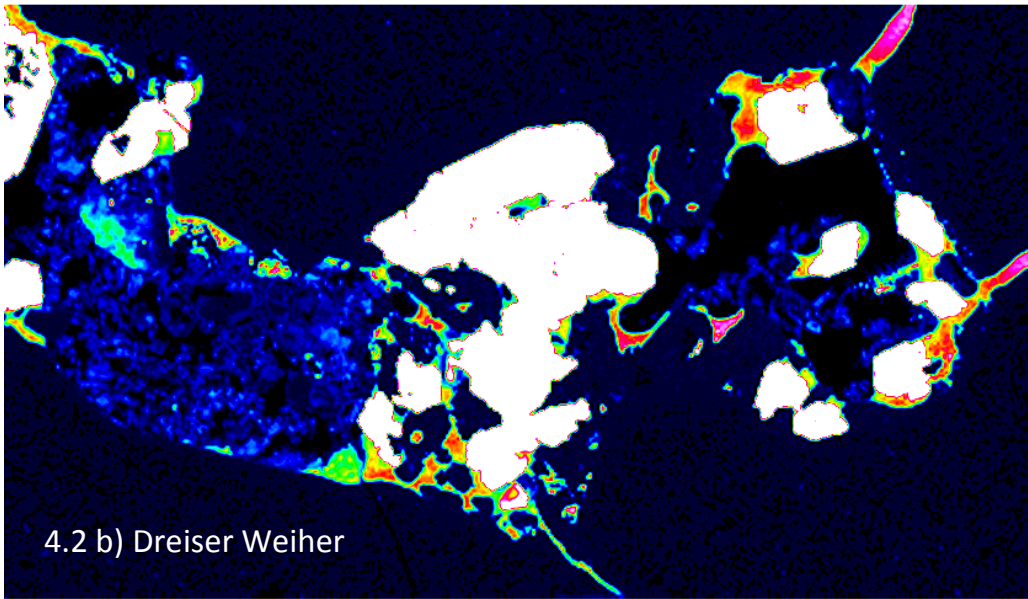


Na	Lv Area%
327	0.0
306	0.0
286	0.0
265	0.0
245	0.0
224	0.0
204	0.1
183	0.3
163	0.9
143	1.2
122	0.9
102	0.7
81	0.8
61	1.0
40	1.5
20	9.2
0	83.4
Ave	13

Na ————— 200 um

Na WDS 2ch TAP
 Ka Order 1
 Peak Pos. (mm) 129.8430
 Accum. 1
 Max 327
 Min 0
 Ave 13
 A, B value 0.0000, 0.0000

Group : Keppler
 Sample : maxwell
 Jan 22 02:06 2016
 Acc. V 15.0 kv
 Prob C 5.014e-08A
 Scan OFF Mag 430
 Prob Diam. (um) 0
 Dwell(ms) 100.00
 Stage No. 1
 X : 70.4485 mm
 Y : 71.6810 mm
 Z : 10.4885 mm
 Direction: Single
 Points 350*200
 Interval(um) X:3.00
 Y:3.00



Ca	Lv Area%
1000	12.1
937	0.1
875	0.2
812	0.2
750	0.3
687	0.5
625	0.7
562	0.8
500	0.7
437	0.6
375	0.7
312	0.6
250	0.7
187	1.1
125	2.4
62	6.0
0	72.2
Ave	279

Ca ————— 200 um

Ca WDS 4ch PETH
 Ka Order 1
 Peak Pos. (mm) 107.4880
 Accum. 1
 Max 2185
 Min 0
 Ave 279
 A, B value 0.0000, 0.0000

Group : Keppler
 Sample : maxwell
 Jan 22 02:06 2016
 Acc. V 15.0 kv
 Prob C 5.014e-08A
 Scan OFF Mag 430
 Prob Diam. (um) 0
 Dwell(ms) 100.00
 Stage No. 1
 X : 70.4485 mm
 Y : 71.6810 mm
 Z : 10.4885 mm
 Direction: Single
 Points 350*200
 Interval(um) X:3.00
 Y:3.00

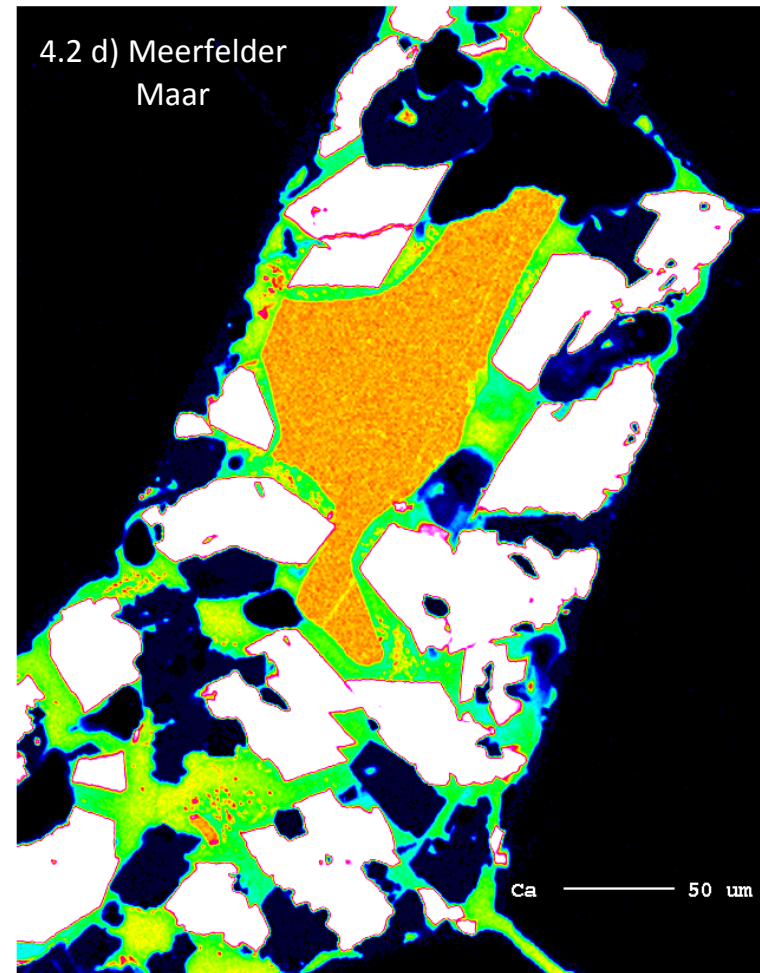
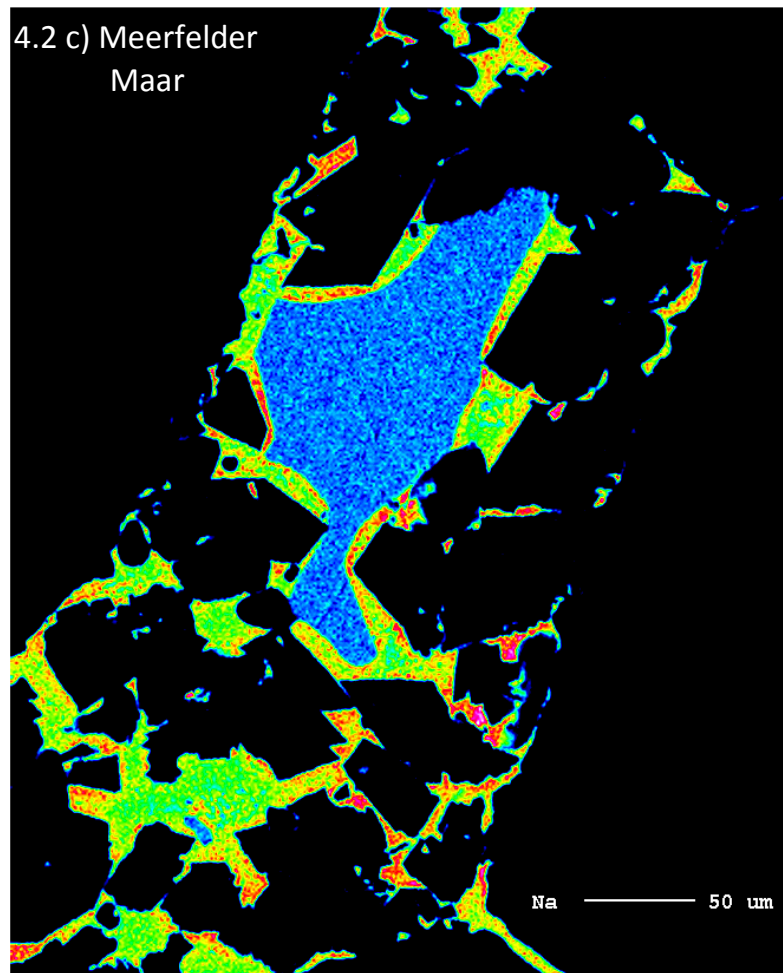


Figure 4.2: Dreiser Weiher elemental map of Na (a) and Ca (b); Meerfelder Maar map of Na (c) and Ca (d). In both localities, we see an enrichment along grain edges, which is not readily apparent to the naked eye.

4.3.2 Isotope Analyses

The Lu-Hf data is shown in table 4.1.1. Sm-Nd and Rb-Sr data are shown in table 4.1.2. Supplemental work done in the Gerritzen 2018 study are shown in table 4.1.3. Data from previous studies can be found in table 4.1.4. The host rock basalt of Dreiser Weiher has an ϵHf of ca. 3.5 and $^{176}\text{Lu}/^{177}\text{Hf}$ of 0.0082. This value falls below several measurements of WR which on average yielded an ϵHf of 4.9. A second WR digestion at high pressure yielded ϵHf values around 2.0 which overlap with those of the most radiogenic mineral separates: one analysis each of Ol (ϵHf of 2.0), OPX (ϵHf of 3.1), and CPX (ϵHf of 2.1). The $^{176}\text{Lu}/^{177}\text{Hf}$ values range is from 0.0270 (CPX) to 0.0953 (OPX). The Dreiser Weiher mineral isochron yields an age of -37 ± 23 Ma (2 s.d.) with an initial $^{176}\text{Lu}/^{177}\text{Hf}$ of 0.282835 ± 0.000046 (ϵHf of 1.9) and an MSWD of 0.58 (figure 4.3). In $^{143}\text{Nd}/^{144}\text{Nd}$ HR ($^{143}\text{Nd}/^{144}\text{Nd}$, 0.512799 ± 0.000035 , ϵNd of 3.1) is the most radiogenic, followed by Ol (0.512690 ± 0.000015 , ϵNd 1.1 ± 0.2), and OPX, CPX, and WR (ca. 0.516700 ± 0.000200 , ϵNd of 0.8). In contrast to the host rock, whose $^{147}\text{Sm}/^{144}\text{Nd}$ is 0.1003 ± 0.0001 , all mineral separates and WR yielded $^{147}\text{Sm}/^{144}\text{Nd}$ below ca. 0.1, ranging from 0.0894 (whole rock) to 0.03483 (OPX). This creates an isochron with an age of -76 ± 110 Ma, an initial $^{143}\text{Nd}/^{144}\text{Nd}$ of 0.282842 ± 0.000030 , and an MSWD of 1.2 (figure 4.4). The host rock has an $^{87}\text{Rb}/^{86}\text{Sr}$ of 0.28 and overlaps with CPX, OPX, and WR in its $^{87}\text{Sr}/^{86}\text{Sr}$ of 0.70422. The host rock thus isotopically overlaps typical ONB basalts (figure 4.8). Despite a range of $^{87}\text{Rb}/^{86}\text{Sr}$ from 0.0022 ± 0.0001 (CPX) to 0.0550 (Ol), CPX, OPX, and WR all share the same $^{87}\text{Sr}/^{86}\text{Sr}$, forming a Rb-Sr isochron with an age of 101 ± 580 Ma, an initial $^{87}\text{Sr}/^{86}\text{Sr}$ of 0.703430 ± 0.000330 and an MSWD of 2489 (figure 4.5).

The host rock of the Meerfelder Maar xenolith bears an extremely low $^{176}\text{Lu}/^{177}\text{Hf}$ (0.007623 ± 0.000004), the consequence of its strong enrichment in Hf (23.7 ppm). In Lu-Hf-isochron space, all samples straddle a horizontal line at a $^{176}\text{Hf}/^{177}\text{Hf}$ value of ca. 0.28285 (ϵHf of ca. 2.5) and $^{176}\text{Lu}/^{177}\text{Hf}$ ranging from

0.040194 to 0.044125 for the whole rock replicates. The Lu-Hf isotopic analysis failed for the mineral separates from Meerfelder Maar due to extremely low Hf

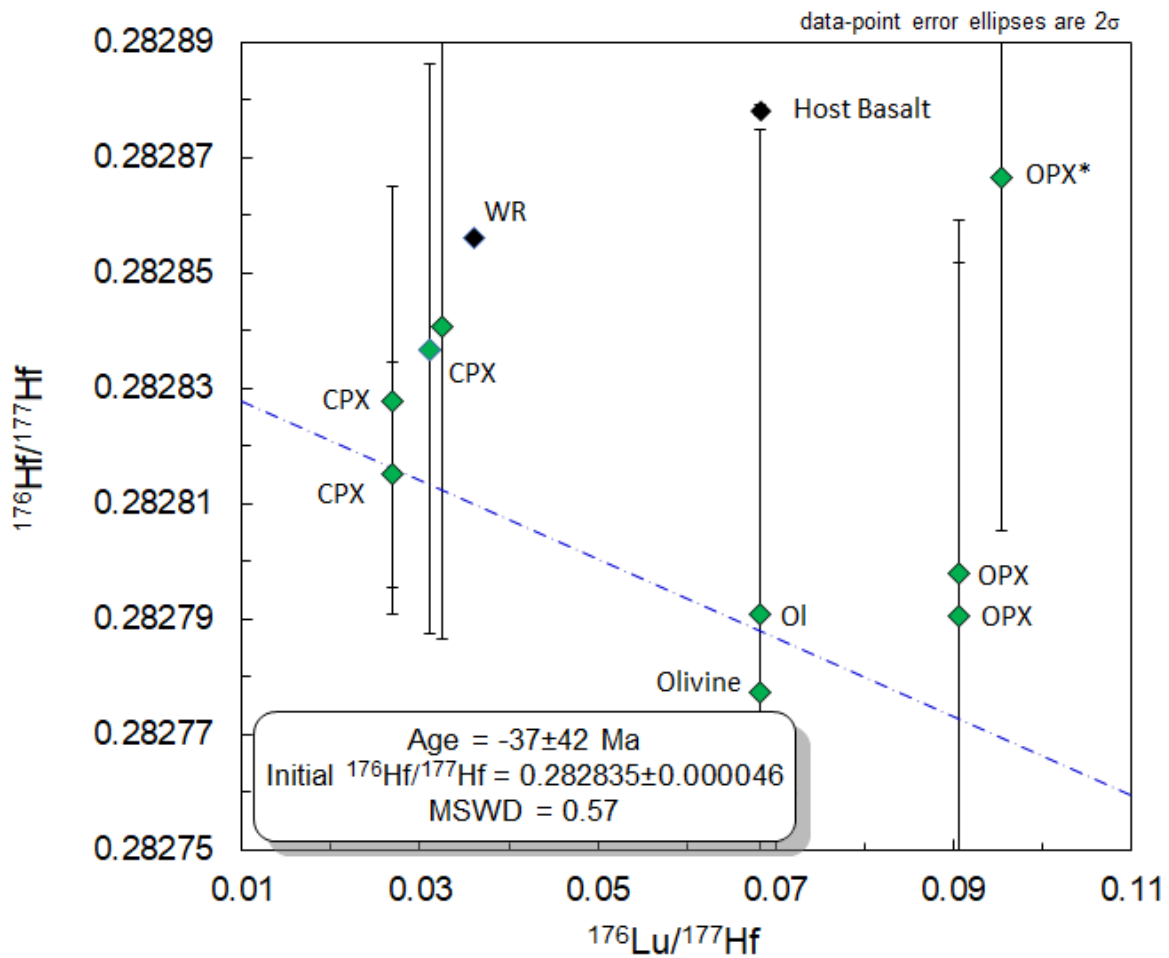


Figure 4.3. Dreiser Weiher mineral isochron. The minerals marked by an * are replicates which had some issues in run. The negative age we round to zero, implying this is a modern age. Note that no mixing line can connect host basalt, whole rock, and any mineral fraction. The mineral fractions are Olivine (Ol), Orthopyroxene (OPX), Clinopyroxene (CPX), Whole Rock (WR), and the host basalt.

abundances that could not be analyzed. The host rock has a $^{143}\text{Nd}/^{144}\text{Nd}$ of 0.512777, while the minerals range from 0.512419 to 0.512557. The host rock also has a slightly higher $^{147}\text{Sm}/^{144}\text{Nd}$ of ca. 0.10 when compared to minerals and whole rock ($^{147}\text{Sm}/^{144}\text{Nd}$ between ca. 0.08 and 0.09). Of note, the WR analyses

from Meerfelder Maar do have some variations associated with it, and the WR digested in autoclaves has a lower $^{143}\text{Nd}/^{144}\text{Nd}$. The Meerfelder Maar Sm-Nd isochron yields an age of -103 ± 350 Ma, an initial $^{143}\text{Nd}/^{144}\text{Nd}$ of 0.51259 ± 0.00020 , and an MSWD of 0.98 (figure 4.6). For $^{87}\text{Sr}/^{86}\text{Sr}$, the Meerfelder Maar mineral separates range from 0.704240 (Ol) to 0.704430 (OPX) in $^{87}\text{Sr}/^{86}\text{Sr}$. The host rock yields an $^{87}\text{Sr}/^{86}\text{Sr}$ of 0.704222 and an $^{87}\text{Rb}/^{86}\text{Sr}$ of 0.2801, which contrasts those of the mineral separates and WR which all are around 0.05.

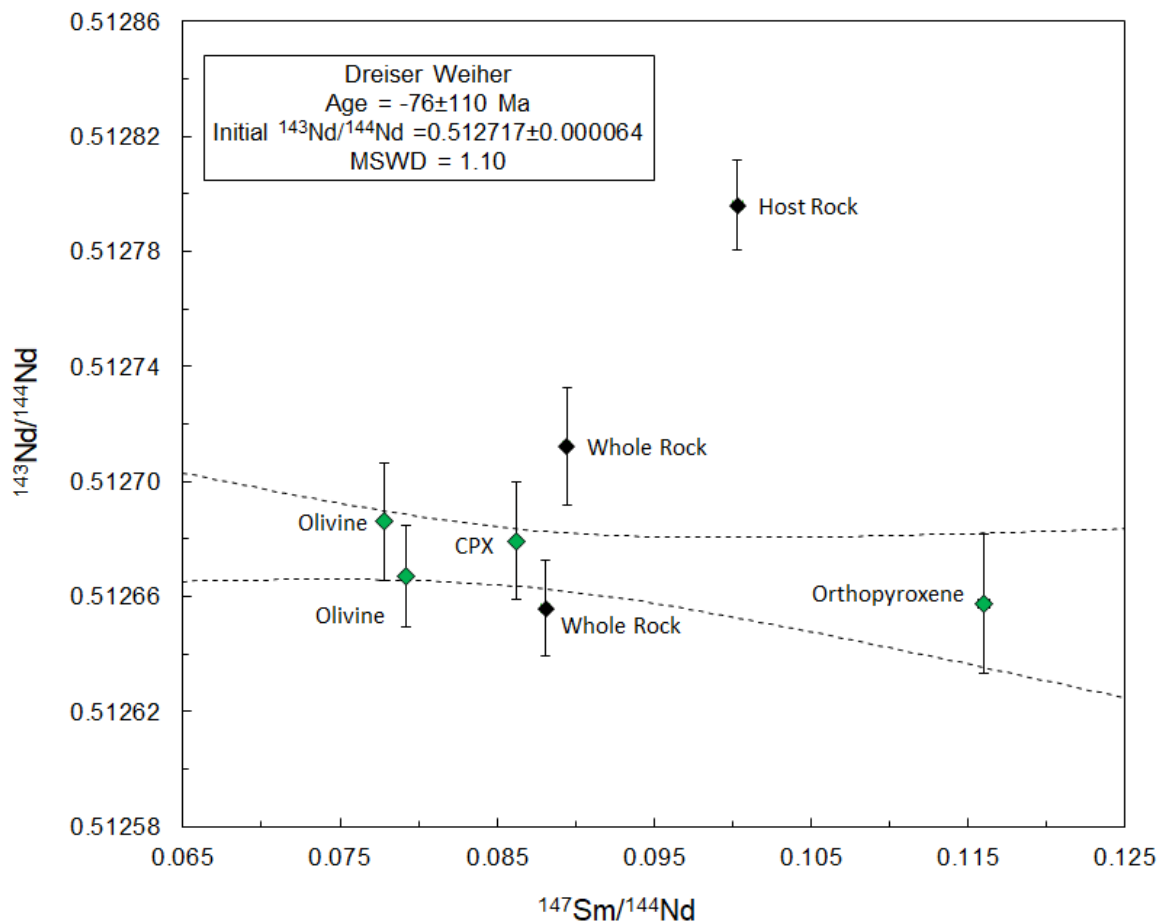


Figure 4.4: Dreiser Weiher mineral separates and Sm-Nd analysis. Note that the negative age is preclude, particularly given the error, with an effective age of 0 – 34 Ma. A mixing line between whole rock, CPX

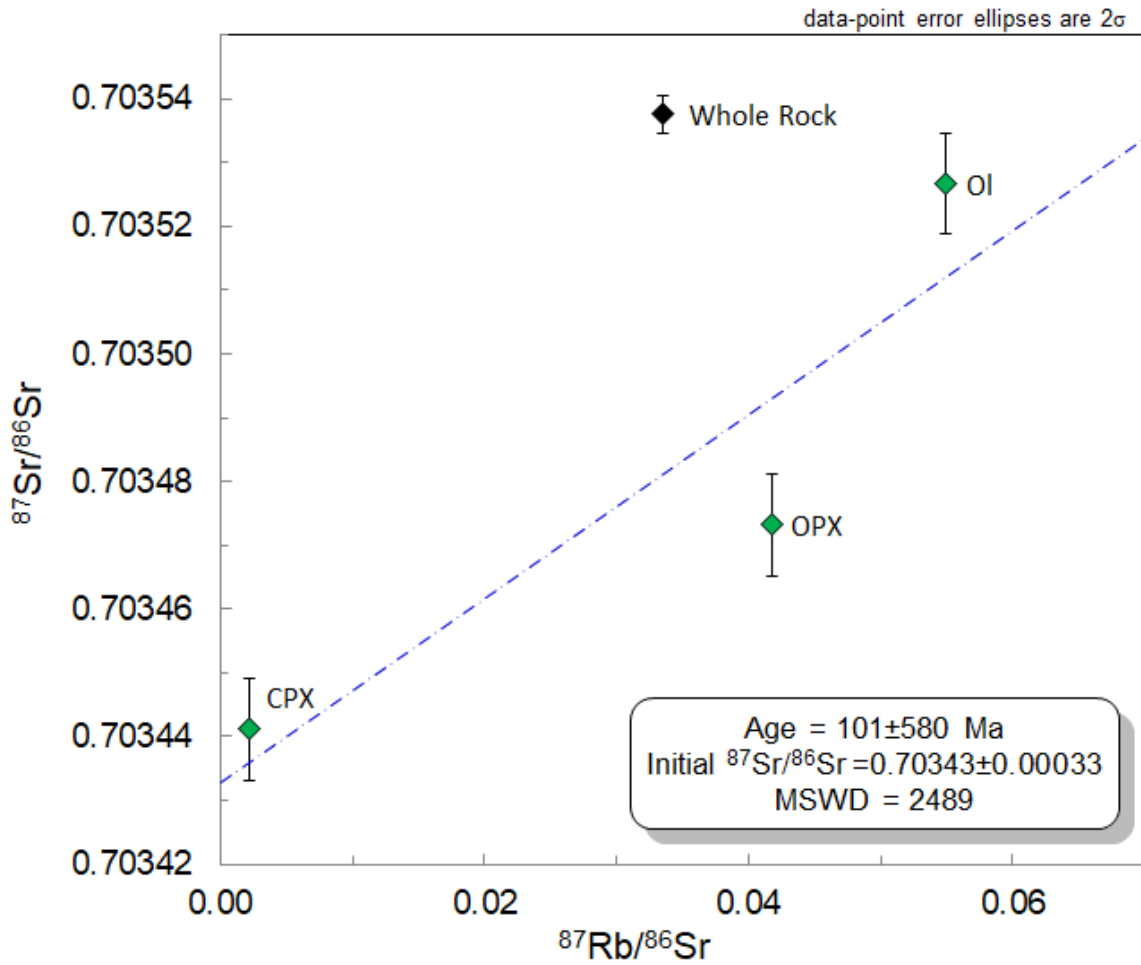


Figure 4.5: Dreiser Weiher mineral isochron. While this yields a non-zero age, the extremely high MSWD makes the data yielded by this suspect, and the age still overlaps with a modern age.

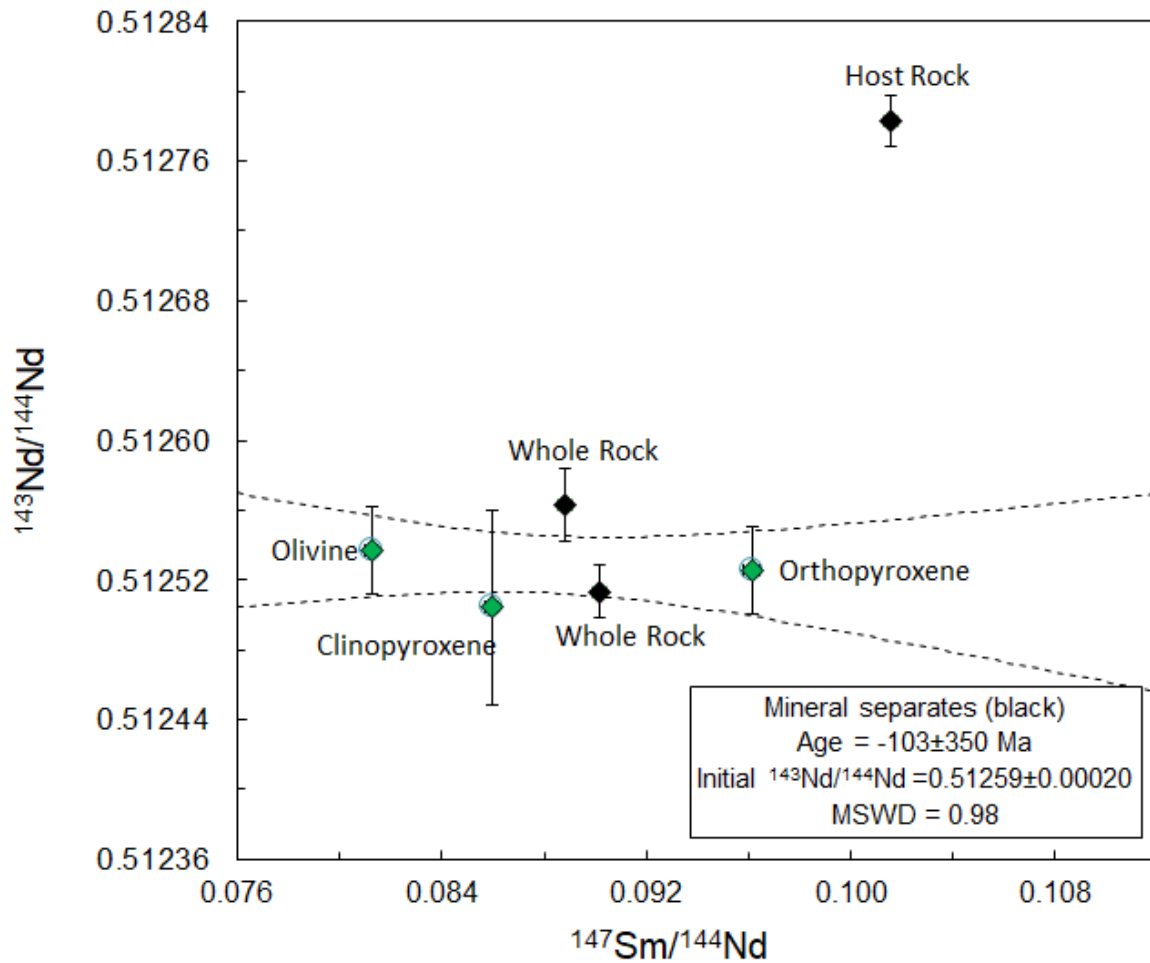
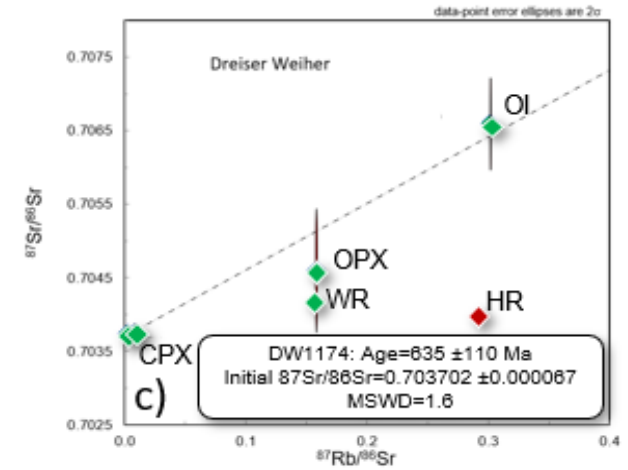
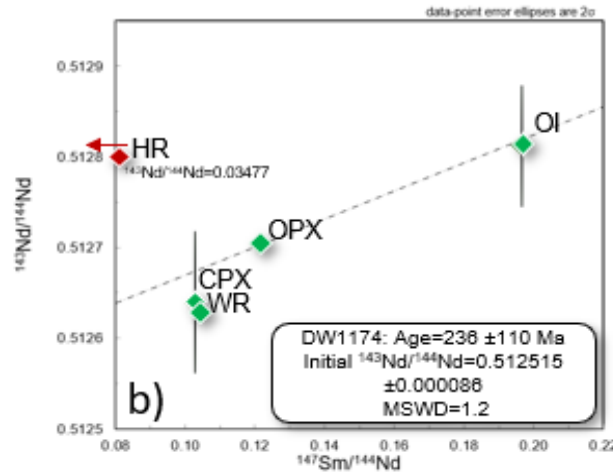
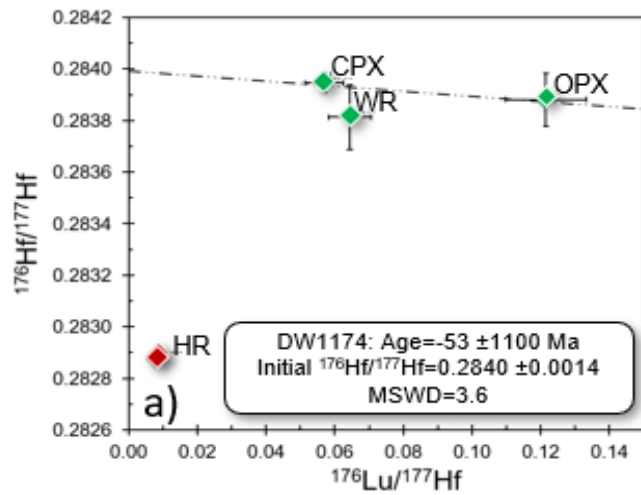


Figure 4.6: Meerfelder Maar mineral isochron. The effect age is from 0 to 247 Ma. While it is possible to draw a mixing line through clinopyroxene, and one portion of the whole rock, and host rock, the range displayed in whole rock precludes this being the case with both whole rock samples, meaning that if a relationship exists, it is present heterogeneously.

Further samples from both localities were investigated for the same properties as in this study in the BSc thesis of C. Gerritzen (figure 4.7), which was conducted under the supervision of M.M. Thiemens. The following discussion will include data from this thesis which in brief summarizes as follows: The data from a Meerfelder Maar peridotite including a Lu-Hf mineral isochron (Age: 8 ± 72 Ma, Initial isotope composition: 0.282868 ± 0.000085 , MSWD: 1.5), a Rb-Sr mineral isochron (Age: -20 ± 49 , initial isotope composition:

Dreiser Weiher



Meerfelder Maar

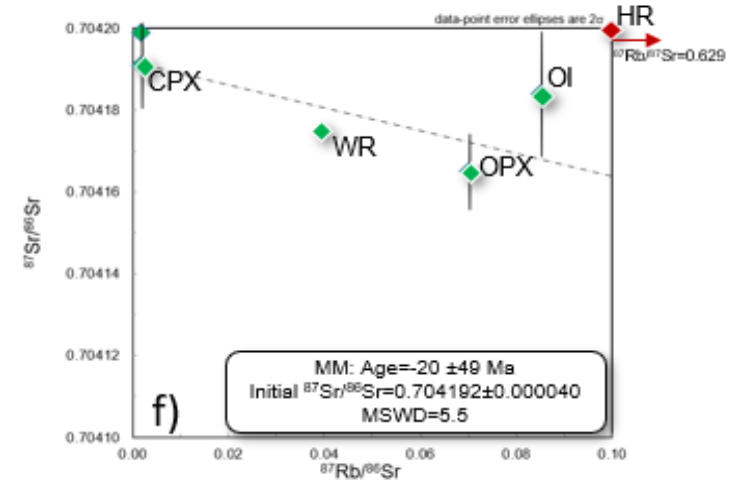
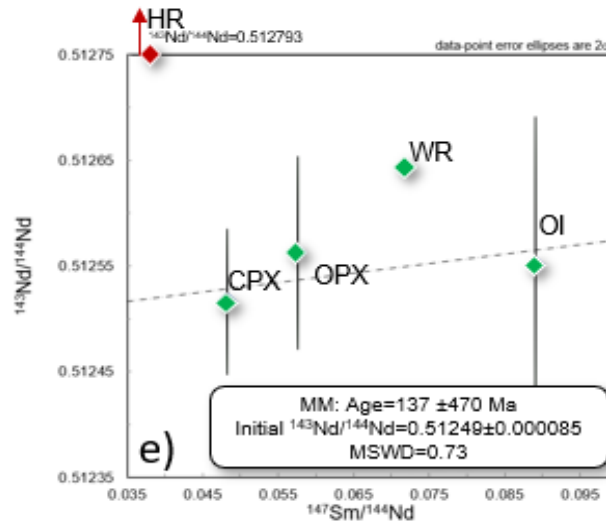
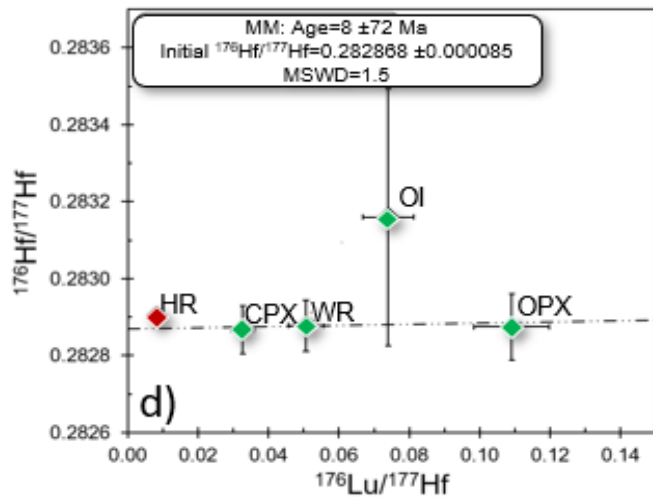


Figure 4.7: Mineral isochrones from Gerritzen, 2018. Lu-Hf, and all three Meerfelder Maar give modern ages within error.

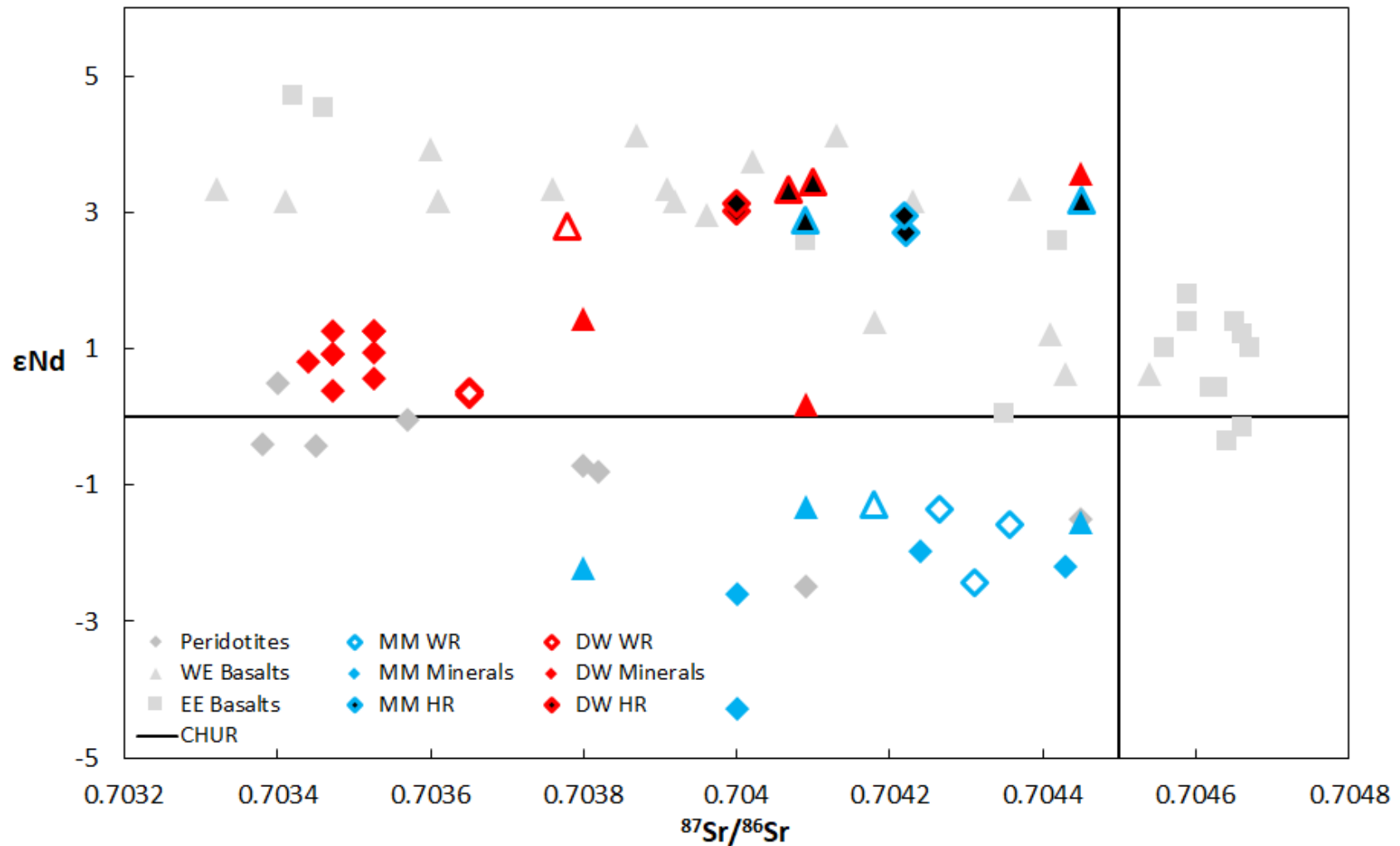


Figure 4.8: A compilation of data (Stosch et al., 1986, grey) (Gerritzen, 2018: triangles, colors matching this study). The minerals all plot closer to CHUR (black line) than the host rocks, which fall within the range of the WE and EE basalt.

0.704192 ± 0.000040, MSWD: 5.5), and a Sm-Nd mineral isochron (Age: 137 ± 2600 Ma, Initial isotope composition: 0.512490 ± 0.000990, MSWD: 73). We will also discuss data from mineral isochrons from a Dreiser Weiher peridotite, including a Lu-Hf mineral isochron (Age: -53 ± 1100 Ma, Initial isotope composition: 0.284000 ± 0.001400, MSWD: 3.6), a Rb-Sr mineral isochron (Age: 635 ± 110 Ma, initial isotope composition: 0.703702 ± 0.000067, MSWD: 1.6), and a Sm-Nd mineral isochron (Age: 236 ± 110 Ma, Initial isotope composition: 0.512515 ± 0.000086, MSWD: 1.2). In plotting the isotope data against 1/concentration she found that the Sm-Nd and Rb-Sr were mixing lines.

4.4.0 Discussion

4.4.1 Direct chronological information - mineral isochrons and model ages

The mineral isochron (excluding the whole rock fraction) for our Dreiser Weiher xenolith yields an age of 0 – 5 Ma via Lu-Hf (figure 4.3), with an initial isotope composition of $^{176}\text{Lu}/^{177}\text{Hf}$ of 0.282835 ± 0.000046 (ϵHf of 1.9). A likewise recent resetting age is implied by the Sm-Nd systematics of the peridotites from Dreiser Weiher and Meerfelder Maar from this study (figure 4.4, 4.6). This age further coincides with recent resetting of Lu-Hf systematics in both the Dreiser Weiher and Meerfelder Maar peridotite as well as that of the Rb-Sr systematics in the former as found in the BSc thesis of C. Gerritzen.

The recent resetting in these peridotites is in accord with previous findings for Meerfelder Maar and Dreiser Weiher peridotites (e.g. Witt-Eickschen, 2007 and references therein). We find, however, that even some vein-free peridotites, which have been suggested to be pristine (Witt-Eickschen *et al.*, 2003), have been thermally reset and – as will be discussed further in the next paragraph – metasomatically overprinted. A classification on the basis of visible veins in

"vein-free" or "veined" might thus lack the needed resolution to be translated directly into "geochemically unaltered" or "altered".

Of note is the extremely radiogenic Hf isotope composition of the Dreiser Weiher peridotite whole rock from Gerritzen (2018) which yielded an ϵ_{Hf} of +37.0. Using this value, chondritic (Bouvier *et al.*, 2008) or depleted mantle (Vervoort and Blichert-Toft, 1999) model ages were calculated according to:

$$t = \frac{1}{\lambda} \left[\frac{\left(\frac{^{176}\text{Hf}}{^{177}\text{Hf}} \right)_i - \left(\frac{^{176}\text{Hf}}{^{177}\text{Hf}} \right)_{\text{sample}}}{\left(\frac{^{176}\text{Lu}}{^{177}\text{Hf}} \right)_i - \left(\frac{^{176}\text{Lu}}{^{177}\text{Hf}} \right)_{\text{sample}}} \right], \text{ wherein } t = \text{time of crystallization, } \lambda = \text{decay}$$

constant, i = the initial values for the mantle from which the peridotite is sourced. These yielded model ages of 1.76 and 1.22 Ga, respectively. These ages concur with Re-Os isotope data which reported a WEVF RE-Os model age of ca. 1.6 Ga (Schmitt and Snow 2002), as well as a Sm-Nd depleted mantle model age of ca. 1.6 Ga found from Eifel xenoliths (Stosch and Lugmair, 1984; Stosch *et al.*, 1986).

The Sm-Nd mineral isochron of this same samples provided an age of 236 ± 110 Ma. Given that the same fraction do not yield a straight line in $^{143}\text{Nd}/^{144}\text{Nd}$ vs. a 1/ppm Nd space, the Sm-Nd isochron was not produced by binary mixing and thus likely has age relevance (e.g., Langmuir *et al.*, 1978). The relatively large uncertainty on this age datum prevents a clear association with a single geologic event. A general relation to the Variscan orogeny or the following Permian extensional regime appears likely, however.

Interestingly, the Rb-Sr isochron of the same sample yields an even older age of 635 ± 110 Ma. While a plot of the same data in $^{87}\text{Sr}/^{86}\text{Sr}$ vs. 1/ppm Sr reveals that binary mixing could have formed this isochron, age relevance cannot a priori be rejected. It should therefore be noted that a similar age has previously been reported for an anhydrous ultramafic nodule (560 Ma, Stosch *et al.*, 1980). Careful observation shows that the Rb/Sr isochron is dominated by the extremely

high Rb/Sr (0.3010) of olivine with its associated radiogenic $^{87}\text{Sr}/^{86}\text{Sr}$ of 0.706478 \pm 0.000051. Considering recently found evidence for the capability of host olivine to lock in the isotope composition of melt inclusions (e.g., Reinhard *et al.*, 2018) and the generally high Rb/Sr of melt, a similar sheltering mechanism of olivine and to a lesser degree opx might have played a role in this peridotite.

4.4.2 Indirect chronological information from recently reset peridotites

In order to understand the nature of imprints in our studied samples, it is of primary importance to discern the distinct signatures imparted in different episodes. The whole rock compositions not falling on the horizontal isochrons indicates an additional component which is not hosted within the main mineral constituents of the samples. The enrichment of incompatible elements on grain boundaries (figure 4.2), suggest that this additional component is hosted on the grain boundaries, which favors a metasomatic overprint by fluid or melt as the cause of the WR – mineral discrepancy. A similar observation has previously been made for instance in peridotites from the Rio grande rift and the Colorado Plateau (Byerly and Lassiter, 2015). Clinopyroxene is the main host for most incompatible elements in peridotite (e.g., Stracke *et al.*, 2011, Byerly and Lassiter 2015), so an overprint by the host rock magma should express itself as a linear array formed by CPX, WR, and HR. As we do not observe this linear array in any isochrons (see Figures 3-7), we preclude the host magma as the impregnating agent. The general isotopic difference between minerals, WR, and HR also speaks against the peridotites being the source of the host basalts. As a final line of evidence, the heterogeneous Hf and Nd isotope signatures obtained from different WR digestions in peridotites from both locations further attests to a heterogeneity that is most compatible with the uneven distribution of a grain boundary component. We thus conclude that the young metasomatic overprint hosted on the grain boundaries of the peridotites is older than the eruption. This

finding is in accord with the observations of Witt-Eickschen *et al.*, (2003), who proposed metasomatic overprints associated to the Cenozoic volcanism for Dreiser Weiher peridotites. The relative chronological order of mineral resetting and overprint cannot be defined with absolute certainty. A resetting of the mineral isochrons before the metasomatic overprint appears more likely, however, given that thermal resetting would most likely incorporate grain boundary material. Given the recurrent regional volcanic activity since ca. 700 ka (Schmincke, 2014), abundant possibility for thermal excesses within the lithospheric mantle was given that might have reset the mineral isochrons of most of our peridotite samples. The same is obviously true for the episode of metasomatism that likely postdates the mineral isochron resetting episode. Possibly, future leaching studies such as for instance conducted by Ionov *et al.* (1993) on peridotite samples from Spitzbergen might help reconstruct the geochemical and isotope geochemical signature of the impregnating agents and thus allow a more detailed comparison with signatures of regional volcanic rocks (e.g., Stosch and Lugmair, 1986; Wörner *et al.*, 1986).

4.5.0 Conclusions

We analyzed peridotites from the West Eifel volcanic field in these studies. We analyzed two peridotites from Meerfelder Maar and two peridotites from Dreiser Weiher. We report largely overprinted, modern ages found, with ages of 0 ± 15 Ma (DW, Lu-Hf), 101 ± 580 Ma (DW, Rb-Sr), and 0 ± 34 Ma (DW, Sm-Nd). From Meerfelder Maar we found an age of $0 - 247$ Ma with Sm-Nd, while the other methods did not yield enough data for isochrons. In one peridotites from Dreiser Weiher, we found a better preserved chronology, with evidence for an overprint by the Variscan orogeny, a heating event ca. 635 Ma, and an origin of the peridotite at 1.5 ± 0.3 Ga, overlapping previously reported Re-Os model ages. Overall, both studies found evidence for metasomatic infiltration as whole rock did not plot on a line consisting of mineral separates. This was supported by the lack of a linear relationship between host rock, whole rock, and minerals (particularly CPX) indicating that the infiltrating agent was not composed of host rock material. Notably, all analyzed peridotites were classified as vein-free anhydrous peridotites. It thus appears that classifications as "vein-free" or "veined" should be treated with care and should not be identified with "geochemically unaltered" or "altered." Nevertheless, interesting and robust information about episodes of metasomatism or melt extraction can be extracted even from suites of such complex samples. This shows the promise of studies such as the one presented here and others performing in-situ analysis of melt fractions trapped within sheltering minerals.

Table 4.1.1: Dreiser Weiher (DW) and Meerfelder Maar (MM) Lu-Hf data								
Locali ty	Type	Hf (ppm)	Lu (ppm)	$^{176}\text{Lu}/^{177}\text{Hf}$	2s.e. on 6th digit	$^{176}\text{Hf}/^{177}\text{Hf}$	2s.e. on 6th digit	ϵ Hf
DW	WR	0.0344	0.0162	0.06705	335	0.282924	124	+5.1
DW	WR	0.0677	0.0148	0.03103	155	0.282837	37	+2.0
DW	WR	0.0344	0.0162	0.06705	335	0.282944	144	+5.8
DW	WR	0.0404	0.0103	0.03616	181	0.282856	56	+2.7
DW	HR	5.0669	0.291	0.008160	41	0.282878	78	+3.5
DW	Ol	0.00719	0.00346	0.06834	342	0.282777	23	-0.1
DW	Ol	0.00719	0.00346	0.06834	342	0.282791	9	+0.4
DW	Ol	0.00921	0.00455	0.03103	155	0.282837	37	+2.0
DW	CPX	0.537	0.123	0.03245	162	0.282841	41	+2.1
DW	CPX	0.588	0.112	0.02697	135	0.282828	28	+1.7
DW	CPX	0.588	0.112	0.02697	135	0.282815	15	+1.2
DW	OPX	0.0281	0.0180	0.09062	453	0.282798	2	+0.6
DW	OPX	0.0281	0.0180	0.09062	453	0.282790	10	+0.4
DW	OPX	0.0466	0.0313	0.09534	477	0.282867	67	+3.1
DW	Spinel	1.000	215.737	101.5455	5.1E+05	12.918755	1.3E+07	n.d.
MM	WR	0.103	0.0292	0.04019	2.0E-04	0.282858	58	+2.8
MM	WR	0.0787	0.0245	0.04413	2.2E-04	0.282866	66	+3.0
MM	WR	0.0801	0.0248	0.04389	2.2E-04	0.282976	176	+6.9
MM	WR	0.0801	0.0248	0.04389	2.2E-04	0.282962	162	+6.4
MM	HR	23.739	1.275	0.007623	3.8E-05	0.282856	56	+2.7
WR (Whole Rock), HR (Host Rock), Ol (Olivine), CPX (Clinopyroxene)								

Table 4.1.2: Dreiser Weiher (DW) and Meerfelder Maar (MM) Sm-Nd-Rb-Sr										
		Sm (ppm)	Nd (ppm)	$^{147}\text{Sm}/^{144}\text{Nd}$	ϵNd	$^{143}\text{Nd}/^{144}\text{Nd}$	Rb (ppm)	Sr (ppm)	$^{87}\text{Rb}/^{86}\text{Sr}$	$^{87}\text{Sr}/^{86}\text{Sr}$
MM	WR	0.250	0.988	0.08942	+1.4	0.512712	0.322	27.783	0.0335	0.703538
MM	WR	0.206	0.835	0.08810	+0.4	0.512657	0.304	28.272	0.0311	0.703651
MM	WR	0.206	0.835	0.08811	+0.3	0.512655	n.d	n.d	n.d	0.703651
MM	HR	10.697	38.049	0.1003	+3.0	0.512793	n.d	n.d	n.d	0.704000
MM	HR	10.698	38.053	0.1003	+3.1	0.512799	n.d	n.d	n.d	0.704000
MM	Ol	0.0180	0.0694	0.09271	+1.3	0.512703	n.d	n.d	n.d	0.703527
MM	Ol	0.0403	0.0694	0.2072	+1.3	0.512703	n.d	n.d	n.d	0.703527
MM	Ol	0.0403	0.185	0.07780	+0.9	0.512686	0.0794	4.179	0.0550	0.703527
MM	Ol	0.0612	0.275	0.07916	+0.6	0.512667	n.d	n.d	n.d	0.703527
MM	CPX	4.726	19.534	0.08625	+0.8	0.512679	0.294	393.658	0.00216	0.703441
MM	OPX	0.135	1.387	0.03483	+0.9	0.512686	n.d	n.d	n.d	0.703473
MM	OPX	0.135	0.521	0.09277	+1.3	0.512702	0.123	8.517	0.0418	0.703473
MM	OPX	0.0826	0.251	0.1160	+0.4	0.512658	n.d	n.d	n.d	0.703473
MM	OPX	0.303	1.387	0.07783	+0.9	0.512686	n.d	n.d	n.d	0.703473
DW	CPX	0.399	1.656	0.08597	-4.3	0.512419	n.d	n.d	n.d	0.704000
DW	CPX	0.399	1.656	0.08594	-2.6	0.512504	n.d	n.d	n.d	0.704000
DW	OPX	0.0496	0.217	0.08124	-2.0	0.512537	0.176	8.218	0.0620	0.704240
DW	OPX	0.109	0.404	0.0961	-2.2	0.512525	0.488	22.967	0.0615	0.704430
DW	HR	10.078	35.407	0.1016	+2.7	0.512777	89.0105	919.281	0.280	0.704222
DW	WR	10.081	35.417	0.1016	+3.0	0.512789	n.d	n.d	n.d	0.704220
DW	WR	0.271	1.071	0.09015	-2.4	0.512513	n.d	n.d	n.d	0.704310
DW	WR	0.306	1.223	0.08883	-1.6	0.512557	0.513	23.802	0.0623	0.704357
DW	WR	0.306	1.224	0.08877	-1.3	0.512569	0.513	38.0491	0.0390	0.704264

WR (Whole Rock), HR (Host Rock), Ol (Olivine), CPX (Clinopyroxene)

Table 4.1.3: Meerfelder Maar (MM) and Dreiser Weiher (DW) data from Gerritzen, 2018											
Description	$\frac{^{87}\text{Rb}}{^{86}\text{Sr}}$	$^{87}\text{Sr} / ^{86}\text{Sr}$	2s.e. on 6th digit	$\frac{^{147}\text{Sm}}{^{144}\text{Nd}}$	$\frac{^{143}\text{Nd}}{^{144}\text{Nd}}$	2s.e. on 6th digit	ϵNd	$\frac{^{176}\text{Lu}}{^{177}\text{Hf}}$	$\frac{^{176}\text{Hf}}{^{177}\text{Hf}}$	2s.e. on 6th digit	ϵHf
MM-OI	0.0701	0.704163	8	0.06	0.512563	749	-1.3	0.07401	0.283160	333	+13.7
MM-OPX	0.0849	0.704179	12	0.09	0.512550	115	-1.6	0.1091	0.282874	85	+3.6
MM-CPX	0.00185	0.704199	17	0.05	0.512517	5619	-1.2	0.03267	0.282867	63	+3.4
	0.00185	0.704190	9								
MM-WR	0.0382	0.704177	13	0.07	0.512564	412	-1.3	0.05067	0.282877	66	+3.4
	0.0463	0.704186	9								
MM-HR	0.629	0.704216	12	0.04	0.512778	783	+2.9	0.008199	0.282829	34	+4.6
	0.631	0.704230	7	0.04	0.512793	840	+3.2	0.008199	0.282903	34	+4.7
DW-1174-OI	0.301	0.706478	51	0.1	0.512640	638	+0.2	0.2254	0.283096	2699	+11.5
DW-1174-OPX	0.158	0.704530	69	0.2	0.512813	548	+3.6	0.1215	0.283881	102	+39.2
DW-1174-CPX	0.00265	0.703745	9	0.12	0.512704	561	+1.4	0.05704	0.283945	39	+41.5
	0.00861	0.703756	11								
DW-1174-WR	0.0147	0.703778	15	0.11	0.512773	115	+2.8	0.06442	0.283813	125	+37.0
DW-1174-HR	0.295	0.704068	8	0.03	0.512801	678	+3.3	0.008109	0.282875	30	+4.0
	0.297	0.704100	8	0.03	0.512806	958	+3.4	0.008106	0.282884	31	+3.7
DW-1174-Sp	0.223	0.704694	177	n.d.	n.d.	n.d.	n.d.	0.00514	0.259465	106887	0.0

WR (Whole Rock), HR (Host Rock), Ol (Olivine), CPX (Clinopyroxene)

Table(s) 4.1.4

B=basanite	L=leucitite	HT=hauyne tephrite	LN=leucite nephelinite	HN=hauyne nephelinite	P=phonolite
ON=olivine nephelinite	MN=melilitite nephelinite	M=melilitite	NL=nepheline leucitite	AOB=alkali olivine basalt	OM=olivine melilitite

East Eifel					
Sample	Locality	Rock type	87Sr/86Sr	143Nd/144Nd	εNd
E 41	Rothenberg	B	0.704640	0.512620	-0.4
E 420	Rothenberg	B	0.704610	n.d.	n.d.
E 216	Roter Berg	B	0.704590	0.512710	+1.4
E 204	Nickenichter Sattel	B	0.704650	0.512710	+1.4
E 392	Hohe Buche	B	0.704670	0.512690	+1.0
E 428	Wannen	B	0.704630	0.512660	+0.4
E 520	Lorenzfelsen	L	0.704590	0.512730	+1.8
E 189	Wingertsberg	HT	0.704700	n.d.	n.d.
E 289	An der Ahl	L	0.704720	n.d.	n.d.
E 292	Hochstein	LN	0.704660	0.512700	+1.2
E 308	Herchenberg	HN	0.704350	0.512640	+0.0
E 306	Perler Kopf	L	0.704660	0.512630	-0.2
LV1505	Dom in Rott	P	0.704590	n.d.	n.d.
LV2803	Brauning	ON	0.704420	0.512770	+2.6
LV 3429	Bell Grube	L	0.704560	0.512690	+1.0
LV 3511	Tiefenstein	L	0.704620	0.512660	+0.4
E 382	Larchenkopf	AOB	0.703420	0.512880	+4.7
E 393	Steinbergskopf	AOB	0.704090	0.512770	+2.6
E 350	Arensberg	AOB	0.703460	0.512870	+4.5
Hornblendite veins	Locality	Rock type	87Sr/86Sr	143Nd/144Nd	εNd
MM214	Meerfelder Maar	am	0.703760	0.512770	+2.6
MM262	Meerfelder Maar	am	0.703730	0.512782	+2.8
MM313	Meerfelder Maar	am	0.703760	0.512795	+3.1
Wall rocks adjacent to hornblendite veins	Locality	Rock type	87Sr/86Sr	143Nd/144Nd	εNd
MM271	Meerfelder Maar	cpx	0.703790	0.512690	+1.0

West Eifel F group					
Sample	Locality	Rock type	87Sr/86Sr	143Nd/144Nd	εNd
Me 9	Steffelner Kopf	LN	0.704540	0.512670	+0.6
ME 41	Beuel, Kirchw.	MN	0.704380	n.d.	n.d.
ME 74	Pulvermaar	MN	0.704410	n.d.	n.d.
ME 92	Buerberg	MN	0.704180	n.d.	n.d.
ME 108	Walsdorf	MN	0.704180	0.512710	+1.4
ME 357	Rockesk. Kopf	LN	0.704230	0.512800	+3.2
ME 358	Hohenfels	MN	0.704430	0.512670	+0.6
NM 359	Kalem	MN	0.704130	0.512850	+4.1
E 368	Ernstberg	NL	0.704410	0.512700	+1.2
West Eifel ONB group					
West Eifel ONB group	Locality	Rock type	87Sr/86Sr	143Nd/144Nd	εNd
ME 76	Wartsgesberg		0.703910	0.512810	+3.4
ME 77	Mosenberg	ON	0.703870	0.512850	+4.1
ME 90	Bad Bertrich	B	0.703920	0.512800	+3.2
Siebengebirge	Locality	Rock type	87Sr/86Sr	143Nd/144Nd	εNd
SG 1	Mehrberg	B	0.703610	0.512800	+3.2
SG 4	Rottbitze	ONB	0.703680	n.d.	n.d.
Westerwald	Locality	Rock type	87Sr/86Sr	143Nd/144Nd	εNd
WW 1	Ahlbach	ONB	0.703500	n.d.	n.d.
WW 6	Wilsenroth	AOB	0.703880	n.d.	n.d.
275781	Mühlenberg	AOB	0.703400	n.d.	n.d.
275782	Pfahlberg	AOB	0.703930	n.d.	n.d.
275783	Tongrube Bong	AOB	0.704160	n.d.	n.d.
Vogelsberg	Locality	Rock type	87Sr/86Sr	143Nd/144Nd	εNd
VOG 2	Hutten	TH	0.703700	n.d.	n.d.
VOG 7	Ober Lais	B	0.703290	n.d.	n.d.
VOG 15	Nied-Otleiden	AOB	0.703980	n.d.	n.d.
VB 27	Gelnhausen	AOB	0.703610	0.512800	+3.2
Niederhessische Senke	Locality	Rock type	87Sr/86Sr	143Nd/144Nd	εNd
NHS 3	Hinerberg	OM	0.703540	n.d.	n.d.
NHS 4	Elbenberg	OM	0.703560	n.d.	n.d.
NHS 5	Grossenritte	B	0.703630	n.d.	n.d.
NHS 6	Hirzheim	B	0.703520	n.d.	n.d.
NHS 9	Westberg	OM	0.703600	0.512840	+3.9

B=basanite		L=leucitite		HT=haunye tephrite	LN=leucite nephelinite	HN=haunye nephelinite	P=phonolite
ON=olivine nephelinite		MN=melilite nephelinite		M=melilitite	NL=nepheline leucitite	AOB=alkali olivine basalt	OM=olivine melilitite
Rhön	Locality	Rock type	87Sr/86Sr	143Nd/144Nd	εNd		
RHO 3	Bauersberg	AOB	0.703540	n.d.	n.d.		
RHO 5	Ginolfs	AOB	0.703960	0.512790	+3.0		
RHO 7	Rother Berg	B	0.703280	n.d.	n.d.		
RHO 8a	Leubach	B	0.703410	n.d.	n.d.		
RHO 11a	Suhl	ON	0.703320	0.512810	+3.4		
RHO 14	Kellerstein	B	0.703490	n.d.	n.d.		
Heldburger Gangschar	Locality	Rock type	87Sr/86Sr	143Nd/144Nd	εNd		
HBG 1a	Bramberg	AOB	0.703480	n.d.	n.d.		
HBG 2a	Zeilberg	B	0.704370	0.512810	+3.4		
Oberpfalz							
OPF 12	Rauher Kulm	AOB	0.703410	0.512800	+3.2		
OPF 14	Wünschenberg	B	0.703510	n.d.	n.d.		
Rhinegraben: Pfalz (PF) and Kaiserstuhl (KS)	Locality	Rock type	87Sr/86Sr	143Nd/144Nd	εNd		
PF 211	Forst	ON	0.703940	n.d.	n.d.		
KS L2	Lützelberg	ON	0.703310	n.d.	n.d.		
Urach (UR)	Locality	Rock type	87Sr/86Sr	143Nd/144Nd	εNd		
XKU 189a	Owen	OM	0.703750	n.d.	n.d.		
XKU 190	Hochbohl	OM	0.704020	0.512830	+3.7		
Hegau (SG)	Locality	Rock type	87Sr/86Sr	143Nd/144Nd	εNd		
XKH 177	Hohenlöwen	OM	0.703760	0.512810	+3.4		
XKH 209	Blauer Stein	OM	0.703690	n.d.	n.d.		
Anhydrous, LREE depleted, high-temperature peridotites	Locality	Rock type	87Sr/86Sr	143Nd/144Nd	εNd		
DWD58	Dreiser Weiher	cpx	0.702300	0.513346	+13.8		
DWK1	Dreiser Weiher	cpx	0.701850	0.513243	+11.8		
Modally metasomatized, equigranular recrystallized peridotites	Locality	Rock type	87Sr/86Sr	143Nd/144Nd	εNd		
MM262	Meerfelder Maar	cpx	0.704090	0.512511	-2.5		
MM278	Meerfelder Maar	cpx	0.704450	0.512561	-1.5		
MM766	Meerfelder Maar	cpx	0.703800	0.512601	-0.7		
MM766	Meerfelder Maar	am	0.703820	0.512597	-0.8		
DW194	Dreiser Weiher	cpx	0.703400	0.512664	+0.5		
DW211	Dreiser Weiher	cpx	0.703380	0.512617	-0.4		
DW284	Dreiser Weiher	cpx	0.703450	0.512616	-0.4		
DW582	Dreiser Weiher	cpx	0.703570	0.512636	-0.0		
Modally metasomatized, porphyroclastic peridotites	Locality	Rock type	87Sr/86Sr	143Nd/144Nd	εNd		
EE158	East Eifel	am	0.704940	0.512482	-3.0		
Pyroxenite veins	Locality	Rock type	87Sr/86Sr	143Nd/144Nd	εNd		
DW327	Dreiser Weiher	cpx	0.703610	0.512803	+3.2		
DW328	Dreiser Weiher	cpx	0.703610	0.512827	+3.7		
DW906	Dreiser Weiher	cpx	0.703730	0.512820	+3.6		
DW918	Dreiser Weiher	cpx	0.704390	0.512687	+1.0		
Wall rock adjacent to pyroxenite vein	Locality	Rock type	87Sr/86Sr	143Nd/144Nd	εNd		
DW328	Dreiser Weiher	cpx	0.703780	0.512782	+2.8		

5.0 Isotope dating of lunar meteorite NWA 6950

The moon, by her comparative proximity, and the constantly varying appearances produced by her several phases, has always occupied a considerable share of the attention of the inhabitants of the Earth.

From the Earth to the Moon

By J. Verne

1865

5.1.0 Introduction

The early history of the Earth-Moon system is shrouded by the dearth of samples linking compositional features with defined ages. Prevalent theory holds that the Moon accreted from the cloud of debris following one giant impact (e.g. Canup and Asphaug, 2001) or several impacts (Rufu *et al.*, 2017) with the proto-Earth. Following its accretion, the Moon was covered with a thick molten layer, the Lunar Magma Ocean (LMO) (Shearer *et al.*, 2006). As the LMO cooled, olivine- and pyroxene-rich cumulates formed and sank, while a floating anorthositic crust formed on the surface (Shearer and Papike, 1999). These cumulates began to mix within the lunar mantle, perhaps as a density driven overturn (Hess and Parmentier, 1995; Papike *et al.*, 1998; Ringwood and Kesson, 1976). The mixing of these primary cumulates created mantle domains within the lunar mantle which subsequently gave rise to suites such as the low-Ti and high-Ti mare basalts (Elkins-Tanton *et al.*, 2011; Sprung *et al.*, 2013; Snyder *et al.*, 1992).

The existence of lunar samples rich in incompatible elements such as potassium (K), the rare earth elements (REE), and phosphorous (P) was one of the major puzzle pieces which led to the LMO hypothesis and the definition of a KREEP reservoir in the lunar mantle (Hubbard *et al.*, 1971). The hypothesis holds that these samples formed from residual liquid from the LMO, forming primarily between the lunar mantle and the anorthosite crust (Snyder, 1992; Warren, 1990). The subsequent lunar mantle overturn could lead to KREEP being retained in the mantle (Laneuville *et al.*, 2013). KREEP occurs as a component in multiple rock types on the Moon, primarily amongst breccias, in the form of KREEP-basalts and possibly in Mg-suite rocks. Its occurrence has been documented in return samples from all Apollo missions (Meyer 1977). Gamma ray spectroscopy from Apollos 15 and 16 suggested a concentration of KREEP in Mare Imbrium and Oceanus Procellarum (Metzger *et al.*, 1973), which was confirmed already by the first global element maps of the Moon (Lawrence

et al., 1998). The cause of this massive KREEP concentration has been suggested to be the result of the Imbrium impact (Haskin, 1998).

The germanically inspired term urKREEP (Warren and Wasson, 1979) refers to the KREEP rich material generated from LMO crystallization. urKREEP is thought to have been one of the products of the initial lunar differentiation whose formation marks the termination of magma ocean crystallization. This component is critical for any thermal and tectonic model of lunar evolution, as nearly all heat-liberating radioactive elements in the Moon are concentrated within it. A complete understanding of lunar evolution is thus inescapably bound to depicting and understanding the history of the urKREEP component which is highly enriched in incompatible elements.

KREEP magmatism may have been the result of large impacts (Hiesinger *et al.*, 2003; Gaffney and Borg 2014) or radiogenic heat build-up from the urKREEP reservoir leading to KREEP basalt eruption (Nemchin *et al.*, 2012). The lunar crust continued to accrete material up to ca. 1.2 Ga (e.g. Hiesinger *et al.*, 2011), with impact related magmatism extending until 3.4 Ga (Culler *et al.*, 2000; Glikson 2014) and basalt magmatism to 3.2 Ga (Glikson, 2014). Early basalt magmatism, dubbed crypto-mare magmatism, began as early as 4.35 Ga (Joy *et al.*, 2011; Sokol *et al.*, 2008; Terada *et al.*, 2007). Voluminous basalt magmatism continued from 3.9 to 3.1 Ga (e.g. Hiesinger *et al.*, 2003).

Often counted amongst the KREEP-related rocks are specimens of the Mg-suite, so called due to their high Mg number (the ratio of Mg to Fe) (e.g., Gaffney & Borg, 2014; Shearer *et al.*, 2015). The Mg-suite rocks are crustal rocks located in or near the Procellarum KREEP terrane, with an age range of 4.5 to 4.1 Ga (Shearer *et al.*, 2015 and references therein). These samples are thought to have formed during the interaction between urKREEP and rising Mg-rich cumulates during lunar mantle overturn, creating a Mg-rich KREEP hybrid (Elardo *et al.*, 2011; Nemchin *et al.*, 2012; Taylor, 2009). The Mg-suite thus stands separate from KREEP-rich basalts, as the former are plutonic in origin.

Furthermore, several studies of Mg-spinels have argued that KREEP is not required for Mg-suite petrogenesis (Pieters *et al.*, 2014; Prissel *et al.*, 2014)

Attempts to understand the origin and evolution of the lunar magma ocean are fueled by geochemical and petrological modeling to reproduce the distinct isotopic and trace element features of actual lunar samples (Borg *et al.*, 2009; Shearer *et al.*, 2006; Sprung *et al.*, 2013). Of note, recent careful experimental work (Elardo *et al.*, 2011; Rapp and Draper, 2018) lends great support to these mostly theoretical models (e.g., Elkins-Tanton *et al.*, 2011; Snyder *et al.*, 1992). Most sample suites we observe on the Moon can be explained by being generated from distinct cumulate sources within the lunar mantle by melting, where degrees of melting and source characteristics determine the chemical composition of the different lunar sample suites (Leitzke *et al.*, 2016; Snyder *et al.*, 2000; Sprung *et al.*, 2013; Thiemens *et al.*, Under Review). As the Moon has been subjected to heavy bombardment and associated heating, meaningful chronological studies require addressing the distinct susceptibility of minerals or isotopic systems to heating and shock events. Many studies have thus used minerals such as zircon that are highly resistant to alteration (e.g. Barboni *et al.*, 2017; Nemchin *et al.*, 2009) or baddeleyite (Shaulis *et al.*, 2017). Lunar zircon grains are thought to primarily originate from KREEP-rich magmas (Dickinson and Hess, 1982), providing an age limit for latest residual melts that places time constraints on KREEP evolution throughout LMO cooling and differentiation.

The suite of lunar samples available from the Apollo missions is supplemented by lunar meteorites. Amongst these are the Northwest Africa (NWA) 773 clan of meteorites, which includes 773, 2700, 2727, 2977, 3160, 3170, 3333, 6950, 7007, 8127, 10656, 10985, 11616, 11703, and 11767. This clan of lunar meteorites is considered related based on their common ages (Shaulis *et al.*, 2017), similar petrology, and shared brecciation histories (Fagan *et al.*, 2003, 2014; Jolliff *et al.*, 2003; North-Valencia *et al.*, 2014). The 773 meteorite clan is

notable for being enriched in incompatible elements (i.e., are KREEP-rich). The samples are composed of multiple lithological types, and of particular relevance to this study is the magnesian gabbro NWA 6950. This sample has recently been dated to 3100 ± 16 Ga via Pb-Pb dating of baddeleyite (Shaulis *et al.*, 2017), putting it amongst the youngest dated lunar igneous rocks.

5.2.0 Methods

An aliquot of 159 mg was taken from 765 mg of NWA 6950 for isotope composition measurements including neutron dosimetry utilizing the ^{178}Hf - ^{180}Hf neutron dosimeter of Sprung *et al.* (2010; 2013). A whole rock (WR) sample was chosen which appeared as vein free as possible. The remaining material was split into fine ($<125\mu\text{m}$) and coarse ($>125\mu\text{m}$) fractions. The samples were density separated in diiodomethane (methylene iodide, density 3.32 g/cm^3). The fine grain fraction was separated as two fractions, with densities greater or less than 3.32 g/cm^3 , with the material which stayed in suspension combined with the floating material. The coarse grained fraction was subdivided threefold, as 73.5 mg had a density of 3.32 g/cm^3 . We split these samples into the material which sank (density $> 3.32\text{ g/cm}^3$), stayed in suspension (density $\approx 3.32\text{ g/cm}^3$), and material which floated atop (density $< 3.32\text{ g/cm}^3$). These three fractions were handpicked to remove grains with shocked material, leading to 10 fractions being analyzed from the meteorite.

Mixed isotope tracers of ^{149}Sm - ^{150}Nd , ^{180}Hf - ^{176}Lu , and ^{87}Rb - ^{84}Sr , were added to each sample prior to overnight digestion at 120°C in 1:1 cHf - cHNO_3 . Ion-exchange chromatography was performed to purify the samples. All samples first underwent a chemical separation on Biorad AG 50W x8 200-400 mesh resin, where Rb, Sr, a REE fraction and a Hf-rich fraction were separated. Hafnium was further purified on Triskem Ln Resin, and then in a third column on Biorad AG 1 x8. Lutetium was further purified on AG 50W x8 200-400. The

Rb and Sr cuts from column 1 were purified on Triskem Sr spec, and were subsequently ready for analysis. Samarium and Nd were further separated from a REE-rich fraction on Triskem Ln Resin. The element separations are performed from a chemistry based on an aggregate of the methods used in Sprung *et al.* (2013) and Bast *et al.* (2015), detailed in Tusch *et al.* (in prep).

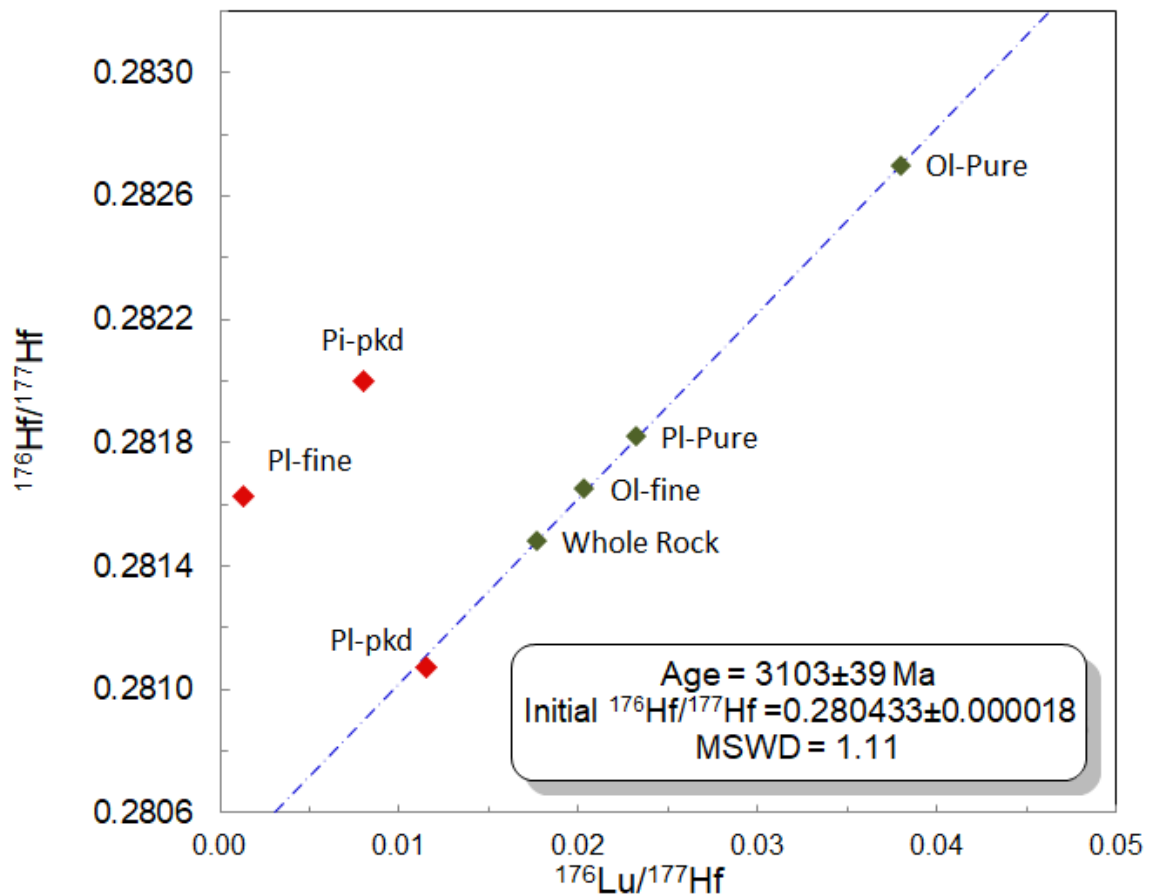


Figure 5.1: Lu-Hf mineral isochron of NWA 6950. The fine grained, low density component appears to be dominated by the shock-melt fraction, given its discordance with the remaining mineral fractions. The initial Hf correlates to $\epsilon\text{-Hf} 2.46 \pm 0.64$

Samples were analyzed on the Thermo Scientific Neptune Plus MC-ICP-MS at Universität zu Köln. Analytical protocols, typical uncertainties, and further details can be found in Münker *et al.* (2001). Procedural blank contributed uncertainties were negligible, with typically measured blanks of 10

pg (Hf), 5 pg (Lu), less than 200 pg (Sr), 50 pg (Rb), and less than 1 pg for Sm and Nd.

5.3.0 Results

The mineral fractions are mainly distinguished by density because obtaining pure mineral fractions was impossible due to the friable nature of the rock. The density $> 3.3 \text{ g/cm}^3$ is subsequently referred to as “Ol” for its high olivine contents. The density fraction at ca. 3.3 g/cm^3 is further labelled “Pi” (for pigeonite). The density fraction $< 3.3 \text{ g/cm}^3$ is henceforth addressed as “Pl” for its enrichment in plagioclase. The fine grained separates are identified via a “-fn” suffix. The picked fractions of the mineral separates are identified with a “-pkd” suffix. Note that purified (i.e., hand-picked) fractions are the least prone to be affected by pieces of shock melt that were easily discernible by their black colour.

The fraction analyzed for neutron dosimetry yielded no non-radiogenic Hf isotope compositions outside of terrestrial values. The radiogenic $^{176}\text{Hf}/^{177}\text{Hf}$ measurements for NWA 6950 thus are free of resolvable neutron capture effects (see Sprung *et al.*, 2010;2013; Gaffney and Borg, 2014)

Values are all reported in tables 5.2a, 5.2b, 5.2c. The purified Ol fraction has the highest $^{176}\text{Hf}/^{177}\text{Hf}$ and $^{176}\text{Lu}/^{177}\text{Hf}$ (0.0380 ± 0.00056 , 0.282699 ± 0.000015 , respectively), and forms the upper end of a linear array including (in order of decreasing isotope and parent-to-daughter ratios) Pl-pure, Ol-fn, bulk rock, and Pl-pkd (0.0232 ± 0.00081 , 0.2818 ± 0.000015). The remaining, non-purified fractions plot off the array towards higher $^{176}\text{Hf}/^{177}\text{Hf}$ (figure 5.1). Plotting the isotope ratio of fractions that correlate well in Lu-Hf isochron space against $1/\text{Hf}$ (figure 5.2) forms a well-correlated linear trend, though this does not exclude binary mixing as the cause of linearity in Lu-Hf isochron space. Plotting the the $^{176}\text{Hf}/^{177}\text{Hf}$ vs. $^{176}\text{Lu}/^{177}\text{Hf}$ trend as a true isochron, we obtain an

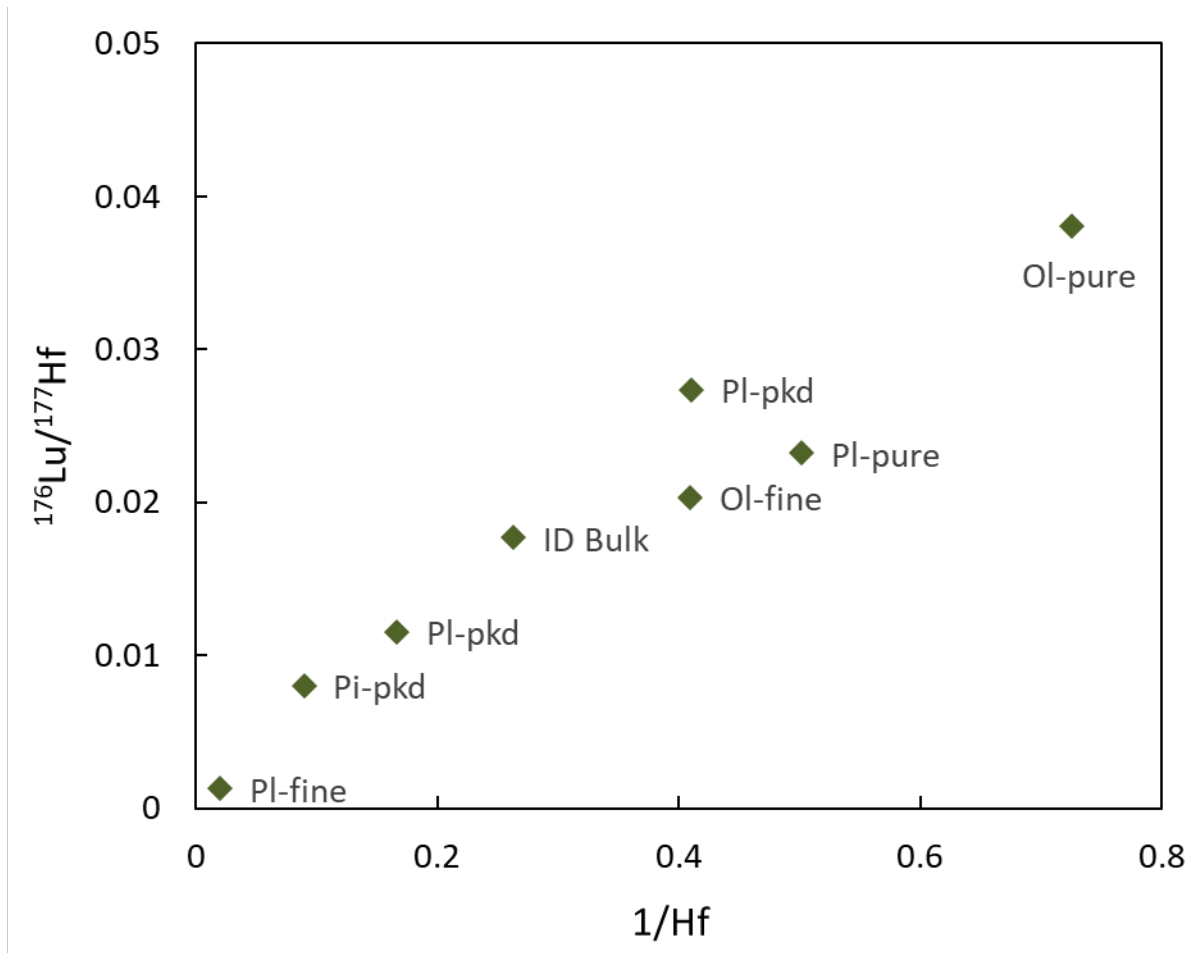


Figure 5.2: A plot of $^{176}\text{Lu}/^{177}\text{Hf}$ yields a linear correlation. We do not preclude the data, however, given the good agreement between the age found via the Lu-Hf isochron and previous Pb-Pb studies.

associated age of 3.103 ± 0.039 Ga (2. S.D.) with an initial isotope composition of 0.280433 ± 0.000018 (2. S.D., equivalent to an ϵHf_t of -12.5 ± 0.6) and an MSWD of 1.1 (figure 5.1). This age is in perfect agreement with the recently published Pb-Pb age of 3.100 ± 0.016 for baddeleyite from the same meteorite (Shaulis *et al.*, 2017). Excluding the whole rock fraction gives an age of 3.087 ± 0.044 , and decreases the MSWD to 0.113, giving an initial isotope composition of 0.280443 ± 0.000023 (ϵHf_t of -12.1 ± 0.6).

The minerals form a well-defined line in $^{143}\text{Sm}/^{144}\text{Nd}$ vs $^{147}\text{Sm}/^{144}\text{Nd}$ space whose slope is equivalent to an age of 3.104 ± 0.45 Ga (MSWD = 1.1, $^{143}\text{Nd}/^{144}\text{Nd}_t = 0.50828 \pm 0.00051$, $\epsilon\text{Nd}_t = -6.3 \pm 0.2$) barring PI-pure ($^{143}\text{Nd}/^{144}\text{Nd}$ 0.512004 \pm 0.000007, $^{147}\text{Sm}/^{144}\text{Nd}$ 0.1573) (figure 5.3). The Pi-pkd has the highest

$^{143}\text{Nd}/^{144}\text{Nd}$ (0.512461 ± 0.000008) and $^{147}\text{Sm}/^{144}\text{Nd}$ (0.2038), with the Ol-pure fraction plotting just below it on the trendline. The Ol-fine and remaining fractions then form a trend, with the Pl-pkd at the lowest ratios. The whole rock plots beneath the isochron formed by the minerals, though overlapping within

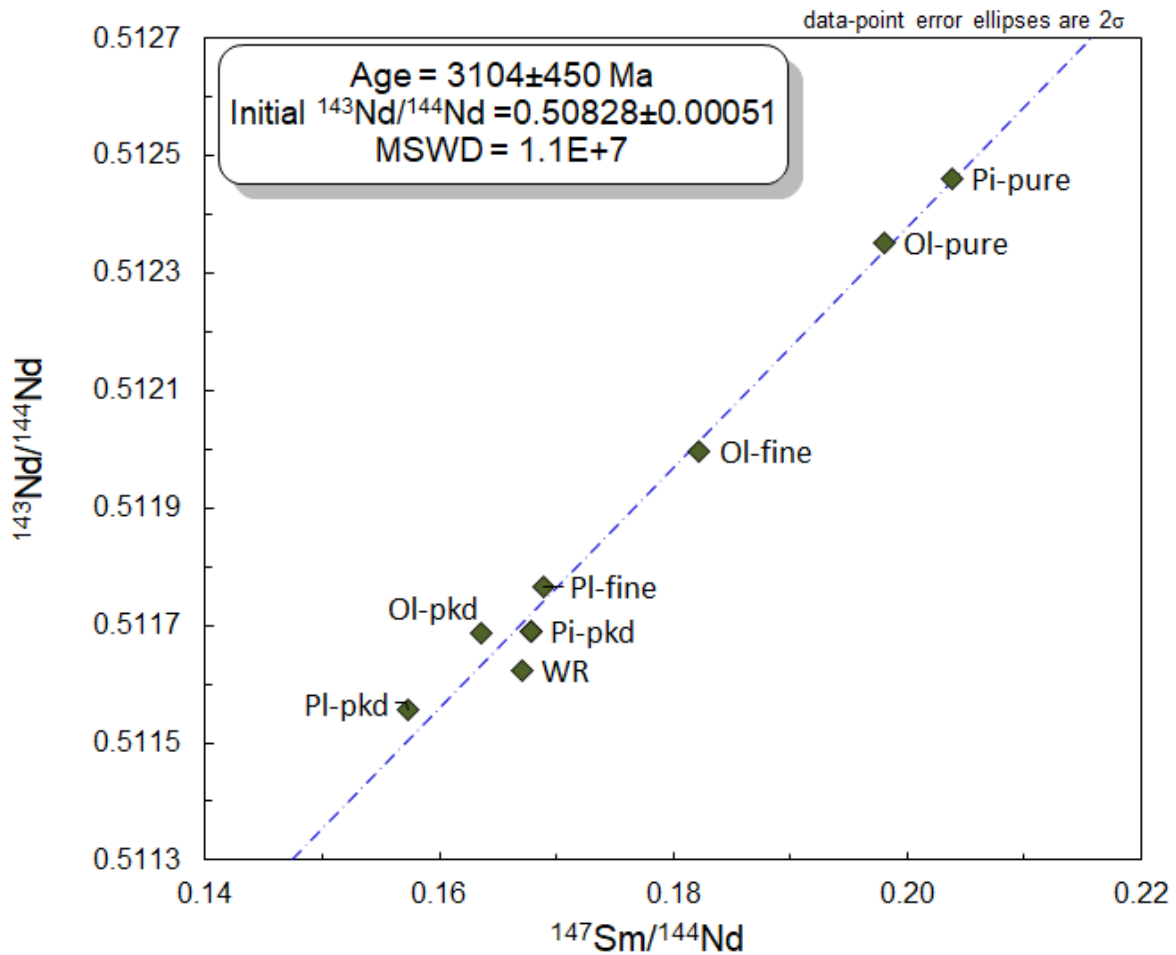


Figure 5.3: A Sm-Nd isochron using whole rock (WR), both fine grain fractions, Ol-fine, Ol-pure, and Pi-Pure. The initial isotope composition correlates to an ϵNd of -4.94.

error. $^{143}\text{Nd}/^{144}\text{Nd}$ vs $1/\text{Nd}$ does not form a well-defined mixing line, but plots along a general linear array (figure 5.4). We thus assign age relevance to the isochron that is formed by picked fractions. The age and initial isotope composition associated with this isochron are fully consistent with our Lu-Hf findings and the Pb-Pb age for baddeleyite (Shaulis *et al.*, 2017). The Ol-pure fraction is the most depleted in Nd (4.3 ppm), while the remaining fractions

range between 8 and 27 ppm. The Pl-pkd, WR, and Ol-pure all form one isochron. Including all fractions, including shock melt compromised fractions, create anisochron. Pi-pure does not plot on either line.

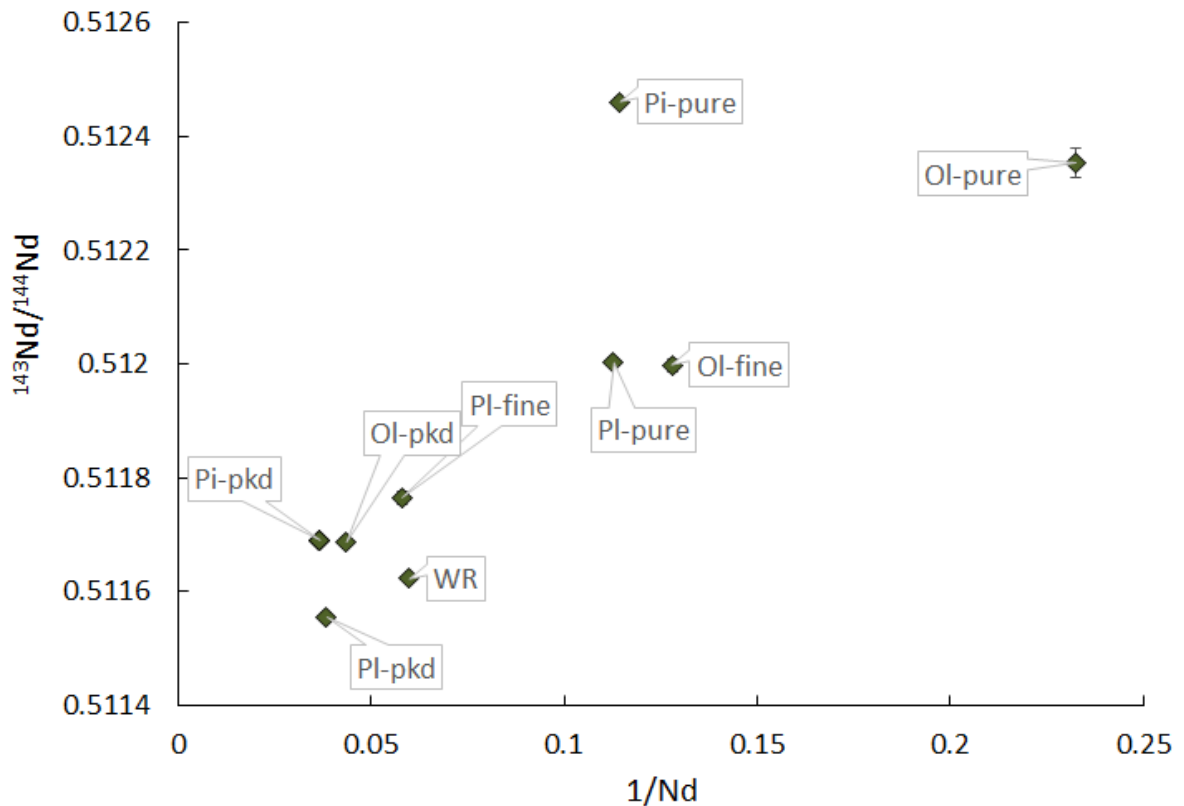


Figure 5.4: A plot of Nd isotope composition against $1/Nd$. Most of the samples fall on a general linear array, although the purified pigeonite portion is clearly not part of a mixing relationship.

The $^{87}Sr/^{86}Sr$ vs. $^{87}Rb/^{86}Sr$ bear a linear relationship between Pl-fn, Pl-pure, and Pl-pkd, with Pl-fn having an $^{87}Sr/^{86}Sr$ of ca. 0.712. The remaining separates all plot together, in an $^{87}Sr/^{86}Sr$ representative of terrestrial values (above average lunar, from 0.70900 to 0.71100) (figure 5.5). A plot of $^{87}Sr/^{86}Sr$ vs $1/Sr$ does not yield a mixing line, but the samples besides Pl-pure and Pl-pkd (which have an $^{87}Sr/^{86}Sr$ between 0.707 and 0.708) all follow a general trend, from Ol-pkd at the lowest end ($^{87}Sr/^{86}Sr = 0.7095$, $1/Sr = 0.032$) to Pl-fine at the highest ($^{87}Sr/^{86}Sr = 0.712$, $1/Sr = 0.011$) (figure 5.6).

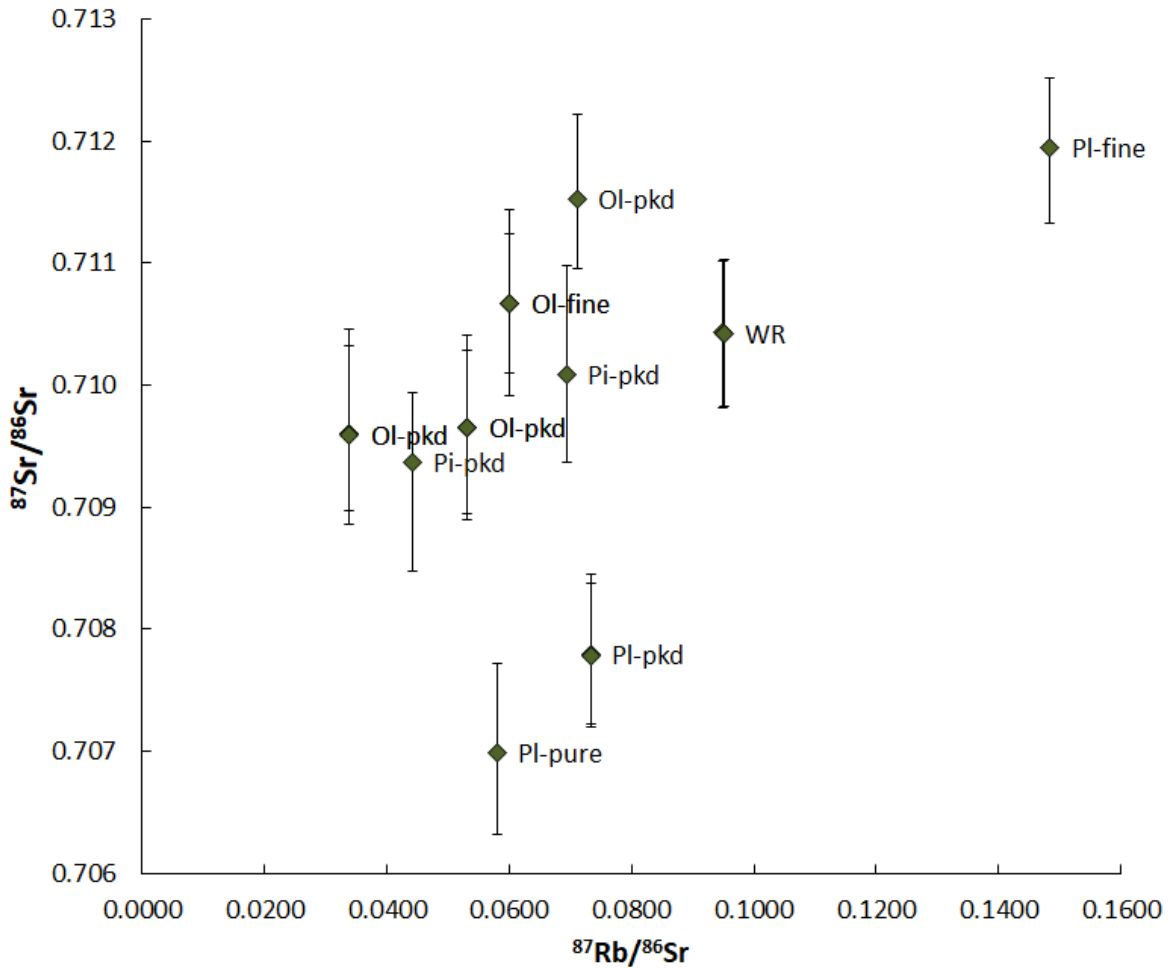


Figure 5.5: Plot of $^{87}\text{Sr}/^{86}\text{Sr}$ vs $^{87}\text{Rb}/^{86}\text{Sr}$ of all mineral fractions shows the separation of the Pl fractions from the remaining material; that is, all samples plot together, while the Pl fractions form an independent array. Of note is that samples fall into the field of terrestrial crustal rocks, perhaps indicative of later alteration.

5.4.0 Discussion

5.4.1 The age of NWA 6950

The age obtained from our Lu-Hf mineral isochron of 3.101 ± 0.039 Ga (figure 5.1) is in excellent agreement with the previously reported Pb-Pb age for baddeleyite (Shaulis *et al.*, 2017) of 3.100 ± 0.016 Ga. This perfect overlap and the scatter displayed by other fraction demonstrates that our careful avoiding of fractions that might possibly be influenced by the presence of shock melt

paid out. Note, that the influence of (trace element-rich) shock melt in the excluded fractions is very likely given their exceedingly high Hf contents, i.e., 1.5 to 13.5 times that of the vein-free whole rock sample. We concur with Shaulis *et al.* (2017) that the ca. 3.1 Ga age found in their and our data is the pristine crystallization age of NWA 6950. Despite being less precise, the Sm-Nd isochron formed by pure mineral fractions yields a consistent age of 3.052 ± 0.057 Ga thus further corroborating our conclusion.

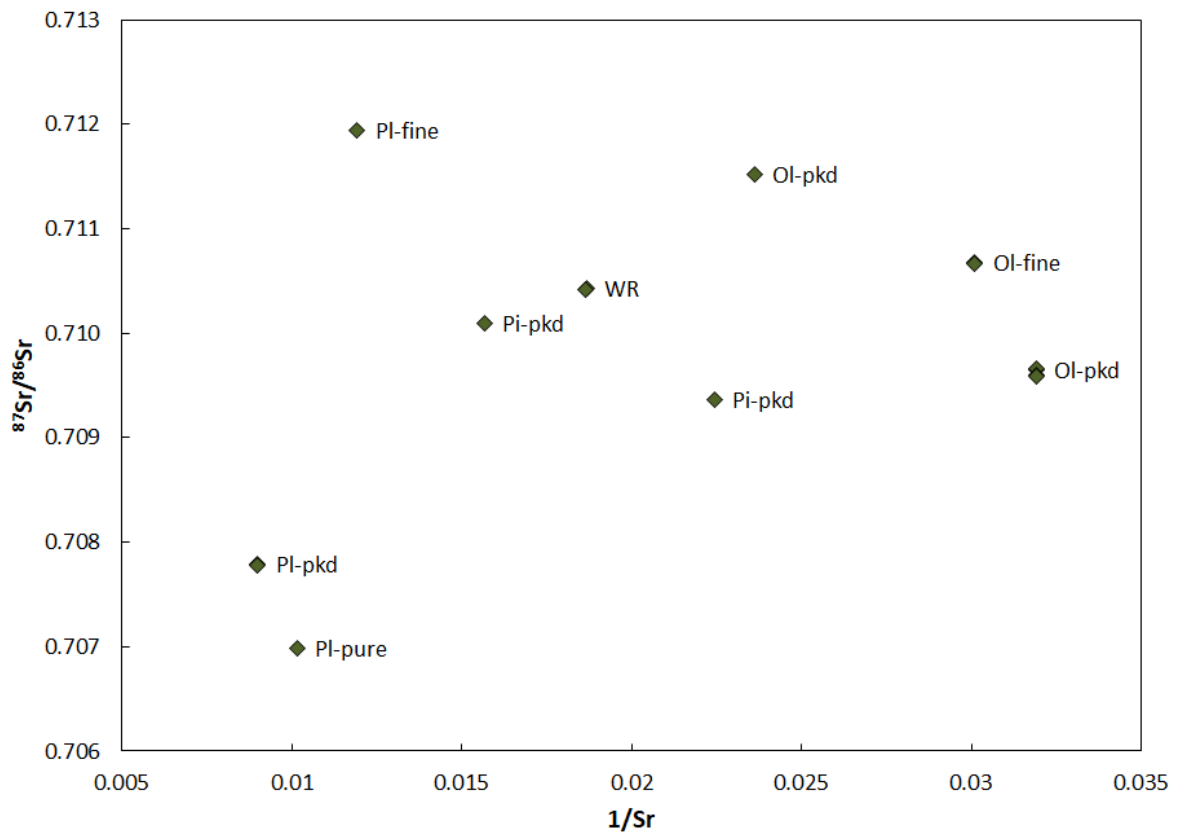


Figure 5.6: While $^{87}\text{Sr}/^{86}\text{Sr}$ against $1/\text{Sr}$ does not yield a mixing line, there is a general trend for all samples excluding the low density, coarse grained samples. This seems to represent a general migration of the samples from lunar values ($<^{87}\text{Sr}/^{86}\text{Sr}$ 0.7090) towards terrestrial compositions ($>^{87}\text{Sr}/^{86}\text{Sr}$ 0.709)

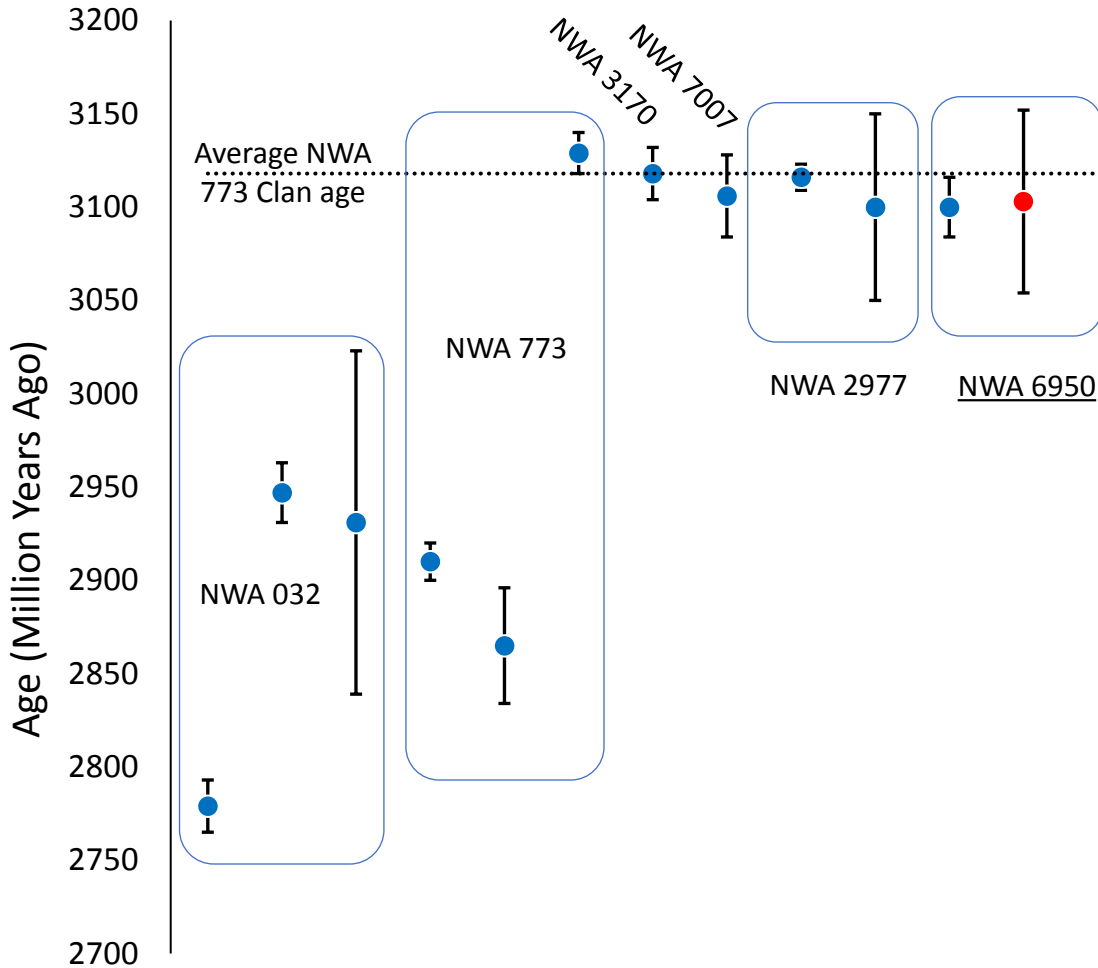


Figure 5.7: NWA 773 Clan dates. NWA 032 has the youngest suite of ages, though these have all been through more easily reset systems (Ar-Ar, Sm-Nd, and Rb-Sr). NWA 773 has been dated with the Sm-Nd, Rb-Sr, and Pb-Pb methods. The remaining samples have been dated with Pb-Pb. Our study (in red) agrees with previous data. Data taken from Fernandes *et al.*, 2003; Borg *et al.*, 2009; Shaulis *et al.*, 2017; Zhang *et al.*, 2010; Nyquist *et al.*, 2009).

5.4.2 Age spectra within the NWA 773 clan

The other ages found for the NWA 773 meteorite clan are reported in figure 5.7. Possibly, NWA 6950 might be slightly younger than the majority of previously dated meteorites, although the uncertainties of all these ages significantly overlap at an average age of 3.118 Ga (Pb-Pb: Shaulis *et al.*, 2017; Zhang *et al.*, 2010; Sm-Nd: Nyquist *et al.*, 2009) Exceptions to this can be found

in age data from systems which are more susceptible to resetting such as Ar-Ar or Rb-Sr (e.g. Borg *et al.*, 2014 with the possible exception of Sm-Nd, e.g. McCulloch and Black, 1984). The age of NWA 773 has been measured as 2.91 ± 0.010 Ga (^{40}Ar - ^{39}Ar dating, Fernandes *et al.*, 2003) and 2.865 ± 0.031 Ga (Sm-Nd dating, Borg *et al.*, 2004, later revised to 2.993 ± 0.033 Ga in Borg *et al.*, 2009), while the more robust Pb-Pb dating of baddeleyite in NWA 773 yielded an age of 3.129 ± 0.011 Ga (Shaulis *et al.*, 2017). The related meteorite NWA 032 yielded an Ar-Ar age of 2.779 ± 0.014 (Fernandes *et al.*, 2003), and Rb-Sr and Sm-Nd ages of 2.947 ± 0.016 , and 2.931 ± 0.092 Ga (Borg *et al.*, 2009), respectively. Altogether, these age data therefore imply that the NWA 773 family precursor rocks formed at ca. 3.1 Ga, but experienced some form of heating event at ca. 2.9 Ga or even later (Fernandes *et al.*, 2003). Note that the Sm-Nd systematics of NWA 6950 including all mineral fractions irrespective of their possible contamination with shock melt also yields an errorchron age of 2.915 ± 0.200 Ga. The typical ca. 2.9 Ga disturbance of Sm-Nd systematics in the NWA 773 clan is thus also a feature in NWA 6950. Considering that this datum is strongly affected by the presence of shock melt, it appears likely that the ca. 2.9 Ga event represents an impact on the lunar surface. The Rb-Sr mineral isochron gives an age of 1.462 ± 0.083 Ga, although it requires excluding the picked low-density fraction. In general, the Rb-Sr systematics of NWA 6950 exhibit surprisingly radiogenic $^{87}\text{Sr}/^{86}\text{Sr}$ for lunar rocks. Most likely, this finding reflects hot-desert weathering of the sample, possibly associated with incorporation of terrestrial Sr via capillary fluids (see for instance Crozaz *et al.*, 2003). Thus, if the Rb-Sr age bears any relevance, it is of a resetting event long after sample crystallization.

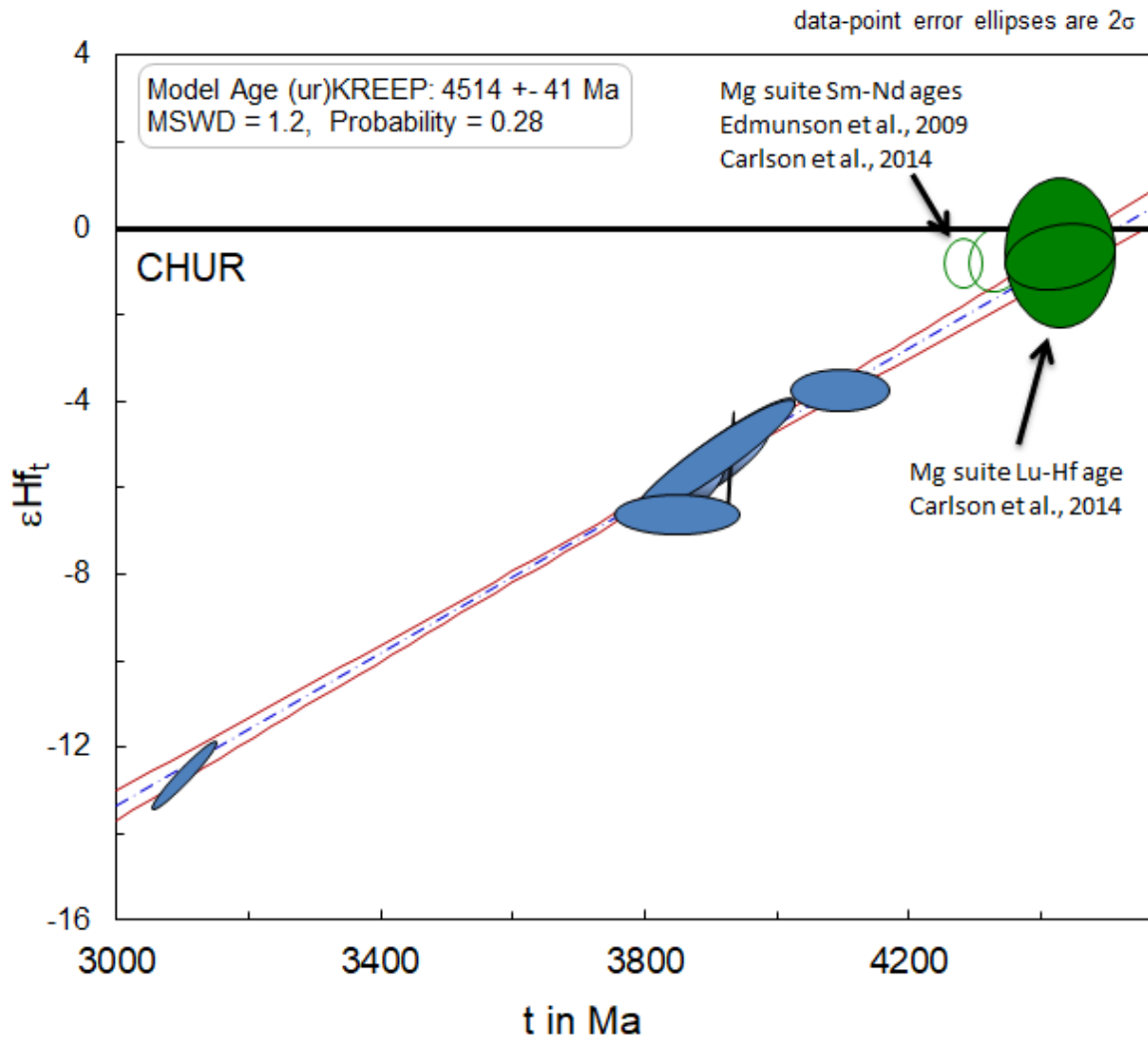


Figure 5.8: ϵHf_t of KREEP-rich whole rocks, with our study. Of note is that Mg-suite samples do not fall on the KREEP evolution line, indicating that they do not represent primary KREEP samples. The intercept of this line at CHUR (ϵHf_i 0) is at 4.51 Ga \pm 0.02, defining a minimum age of LMO crystallization.

5.4.3 NWA 6950 and the evolution of (ur)KREEP

As discussed above, the overlap of baddeleyite Pb-Pb age data (Shaulis *et al.*, 2017) with the Lu-Hf and Sm-Nd isochron age data for the most pristine minerals as well as the preponderance of 3.1 Ga age data within the NWA 773 clan strongly suggests that our NWA 6950 sample provides pristine isotope information with respect to the Lu-Hf and the Sm-Nd systems. A strong kinship

to KREEP has previously been suggested for samples of the NWA 773 clan (e.g., Borg *et al.*, 2009), anchoring the Sm-Nd evolution of KREEP at ca. 2.9 Ga. In an analogous manner, NWA 6950 provides a perfect anchor for the Lu-Hf evolution of KREEP at ca. 3.1 Ga. Our data, in conjunction with data for older pristine KREEP basalts (Gaffney and Borg, 2014) and KREEP-rich breccias (Sprung *et al.*, 2013) (figure 5.8) thus depict a perfectly defined evolution of the KREEP reservoir over 1.4 Ga (MSWD = 1.2), departing from a chondritic evolution at 4.51 ± 0.04 Ga, or 50 my after solar system formation. As a model age for the crystallization of the LMO, this age signifies a minimum age estimate for the formation of the Moon. This finding concurs with recent studies (e.g. Barboni *et al.*, 2017) which find a model age of 4.51 Ga and our own results for the Hf-W model age of the moon (Thiemens *et al.*, under review). Notably, and in contrast to earlier suggestions (Gaffney and Borg, 2014), Mg-suite samples 77215 and 78238 plot off this evolution line and are displaced towards more radiogenic Hf isotope compositions. Interestingly, this offset vanishes assuming the Lu-Hf isochron age of norite 77215 of Carlson *et al.* (2014) to represent the true age of both samples. Hence, a) (ur)KREEP components are either do not dominating the isotopic inventory of Mg-suite rocks or b) these rocks formed from an entirely different source, or c) the Lu-Hf isochron age of these samples represents their crystallization age and formation from a source whose isotopic inventory was dominated by KREEP and their Sm-Nd isochron ages do not reflect Lu-Hf closure but merely that of the Sm-Nd system after protracted cooling.

An analogous treatment of the Sm-Nd isochron initial and age using KREEP rich rocks yields a KREEP formation model age of 4.344 ± 0.095 Ga and a $^{147}\text{Sm}/^{144}\text{Nd}$ of (ur)KREEP of 0.168 ± 0.001 , in good agreement with the $^{146}\text{Sm}-^{142}\text{Nd}$ lunar mantle isochron age of 4.397 ± 0.015 Ga (Boyet and Carlson, 2007; Brandon *et al.*, 2009; Nyquist *et al.*, 1995) as well as previous Sm-Nd model ages for KREEP-rich samples (e.g., 4.360 ± 0.060 Ga, Lugmair and Carlson, 1978) or

combinations of KREEP-rich (including NWA 773) and other crustal samples (4.398 ± 0.045 Ga, Borg *et al.*, 2015). The obtained $^{147}\text{Sm}/^{144}\text{Nd}$ of (ur)KREEP is strikingly similar to actually measured compositions of KREEP-rich breccias (e.g., Sprung *et al.*, 2013; 2014) and somewhat lower than a previously suggested value for (ur)KREEP (e.g., Gaffney & Borg, 2014).

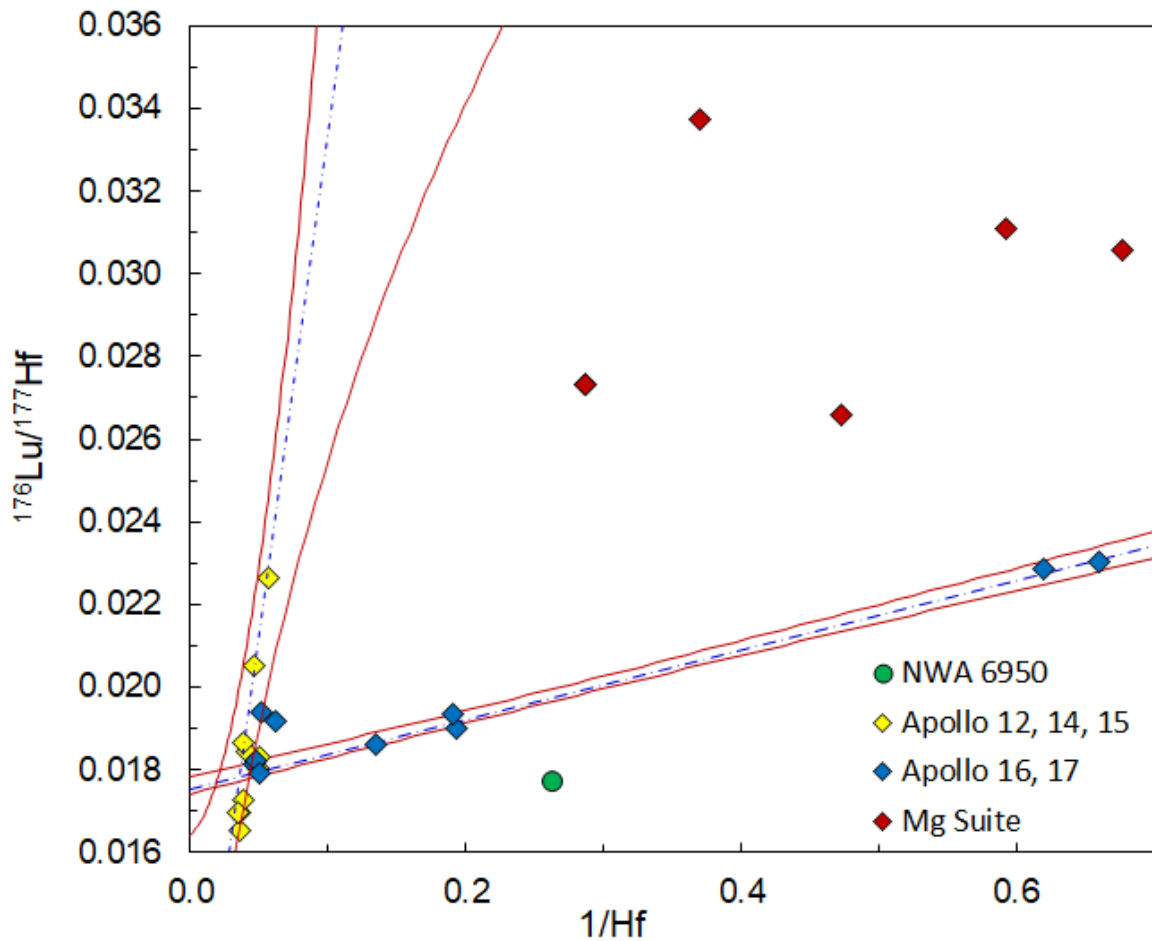


Figure 5.9: $^{176}\text{Lu}/^{177}\text{Hf}$ vs $1/\text{Hf}$. The two trendlines represent mixing of KREEP with a REE-rich (possibly phosphate, sub-vertical) and an ilmenite-rich component. The intercept of the two lines provides a new estimate for the $^{176}\text{Lu}/^{177}\text{Hf}$ of KREEP. The Mg-suite samples do not plot on either line, and similarly do not correspond with either mixing line. NWA 6950 bears an identical $^{176}\text{Lu}/^{177}\text{Hf}$ signature to KREEP, while being depleted in Hf. Data from Carlson *et al.*, 2014; Gaffney *et al.*, 2014; Münker, 2010; Sprung *et al.*, 2014; Unruh and Tatsumoto, 1984.

5.4.4 NWA 6950 representing KREEP evolution

It has been recognized that KREEP-rich breccias from Apollo 16 and 17 which are mixtures of a KREEP-component with other lunar rock types, form a rough trend $^{176}\text{Lu}/^{177}\text{Hf}$ vs. $1/\text{Hf}$ space which was used to estimate the $^{176}\text{Lu}/^{177}\text{Hf}$ of KREEP (Sprung *et al.*, 2013; 2014). Interestingly, KREEP-rich samples from Apollo 12, 14, and 15 provide a distinct line from that of Apollo 16 and 17 samples (figure 5.9). The sub-vertical trend defined by Apollo 12, 14, 15 samples in part is made up of several analyses of the same sample (e.g., 14310) likely indicating that it might be caused by sample heterogeneity possibly in conjunction with having analyzed too small, not representative sample amounts. Obviously, the intersection of these two lines at a $^{176}\text{Lu}/^{177}\text{Hf}$ of ca. 0.0181 provides a reasonable estimate for the $^{176}\text{Lu}/^{177}\text{Hf}$ composition of the KREEP end member in that it is close to the actually measured $^{176}\text{Lu}/^{177}\text{Hf}$ of KREEP rich rocks. Note that this value is near identical to that proposed by Sprung *et al.* (2013; 2014), which is higher than a previous estimate (0.0154, Gaffney and Borg, 2013).

NWA 6950 does not plot on either line, but at a virtually identical $^{176}\text{Lu}/^{177}\text{Hf}$ while being depleted in Hf. NWA 6950 possesses a coarse grained cumulate texture (Shaulis *et al.*, 2017). A plausible petrogenetic scenario for NWA 6950 could thus involve its formation as a cumulate from a KREEP-basalt-liquid whose trace element composition is dominated by a portion of trapped, coexisting liquid in a similar fashion to the likely dominance of trapped coexisting LMO liquid in LMO cumulates (e.g., Fonseca *et al.*, 2014; Snyder *et al.*, 1992; Sprung *et al.*, 2013). Considering the virtually identical $^{176}\text{Lu}/^{177}\text{Hf}$ of NWA 6950 and the inferred (ur)KREEP, it is likely that NWA 6950 is also representative of KREEP isotopically.

Applying the same principles to the Mg suite samples (Carlson *et al.*, 2014) implies that their trace element compositions are not KREEP-dominated as their loose trend does not converge on a $^{176}\text{Lu}/^{177}\text{Hf}$ reasonable for KREEP. While their trace element compositions differs strongly from KREEP, their

formation from an isotopically KREEP-like source at the 4421 Ma Lu-Hf age datum of norite 77215 (Carlson *et al.*, 2014) remains possible.

5.4.5 Differing model ages

Taken at face value, the Sm-Nd and Lu-Hf model ages for KREEP differ outside their statistical uncertainties. It has long been recognized for the Earth's mantle, that secular evolution curves of initial isotope compositions rather depict apparent, less extreme daughter-to-mother element ratios than for instance mantle or the crustal rocks display. The reason for this systematic are interactions between imperfectly closed systems, i.e., isotopic exchange and mixing between recycled components in the mantle or juvenile crust with preexisting crust (Albarede, 1989). Even though the actively convecting terrestrial mantle obviously is prone to blend enriched and depleted components (e.g., Stracke, 2012) far better than the early stagnating lunar mantle (e.g., Zhang *et al.*, 2013), some degree of interaction between lunar mantle components might be possible. Further, increasingly extreme radiogenic isotope disparities such as for instance between the strongly depleted sources of low-Ti mare basalts and KREEP-like, enriched portions in the lunar mantle, to name two extremes, imply that the amount of one component that is needed to change the isotope composition of the other decreases over time. The dominance, that the initial ϵ_{Hf} of NWA 6950 has, being a singular sample that is at least ca. 700 Myr younger than all others is striking: A one ϵ -unit lower initial isotope composition for this sample would cause the Lu-Hf model age to decrease by 75 Myr and to overlap the Sm-Nd model age within the larger uncertainties of the latter. Further, prolonged isotopic exchange of the residual LMO liquid with late-stage ilmenite cumulates perhaps due to tidal heating beneath an insulating anorthositic crust (e.g., Meyer *et al.*, 2010; Elkins-Tanton *et al.*, 2011) would have differing effects on the Lu-Hf and the Sm-Nd systems.

While these late-stage cumulates can reach Sm/Nd that are >40% higher than chondritic, their Lu/Hf exceeds that of CHUR by less than 10% (see supplementary files of Sprung *et al.*, 2013). In concert with the much slower radiogenic ingrowths in the Sm-Nd systems compared to those in the Lu-Hf system, a seemingly delayed departure of $^{143}\text{Nd}/^{144}\text{Nd}$ from chondritic may simply be mimicked by the inferior resolution and a stronger buffering of late-stage cumulates in the case of the Sm-Nd system.

Future Lu-Hf work on other meteorites of the NWA 773 clan might prove critical in deciding if the $^{176}\text{Hf}/^{177}\text{Hf}$ signature of NWA 6950 was rendered more radiogenic than pure KREEP, despite all indications to the contrary. Given the geochemical uncertainties inherent to the model age comparison discussed above, interpreting the presently observed disparity in light of a true geologic or rather selenologic relevance appears premature.

One issue is the extended time scale of solidification required to rectify the old ages for crystallization found (e.g., this study, chapter 6, and Barboni *et al.*, 2017) and the younger ages found in previously mentioned sources, particularly for Sm-Nd (e.g. Borg *et al.*, 2014). The > 100 million year timescale is considerable, and maintaining a liquid LMO for so long does not work with most traditional models (see summary in Elkins-Tanton *et al.*, 2011). One potential method is tidal heating of the Moon by the Earth (Meyer *et al.*, 2010). This would act to slow LMO crystallization, hold portions of the lunar crust above their closure temperatures, and even remelt portions of the crust (Meyer *et al.*, 2010). Therefore, LMO solidification could be decoupled from mineral closure temperatures, and the ages found via isotope systems could represent tidal heating resetting systems (Elkins-Tanton *et al.*, 2011). This would be more than sufficient to extend crystallization for 200 Ma (Elkins-Tanton *et al.*, 2011). Of note, given heterogeneities amongst the Mg-suite rocks, tidal heating could explain the overlapping ages of FANs and Mg-suite, as well as their secondary signature (Edmunson *et al.*, 2009; Elkins-Tanton *et al.*, 2011; Nyquist *et al.*, 1995)

5.5.0 Conclusions

This study finds ages for NWA 6950 which concur with previous studies. We found ages of 3.103 ± 0.045 Ga (Lu-Hf) and 3.104 ± 0.45 Ga (Sm-Nd), in good agreement with the Pb-Pb age of 3.100 ± 0.016 found by Shaulis *et al.*, (2017) as well as the weighted average age found for the NWA 773 clan of 3.115 ± 0.007 Ga. The Sm-Nd age of 4.344 ± 0.095 Ga is in good agreement with other literature values, which we explain as a consequence of long lasting volcanism. We used the Lu-Hf composition of the sample to extend an urKREEP evolution line, and find a lunar crystallization age of 4.51 ± 0.2 Ga, in perfect agreement with the age we find via a completely different method in the next chapter. This is strong evidence for an old Moon.

Table 5.2a: Lu-Hf isotope data for NWA 6950

Sample Type	$\frac{176\text{Lu}}{177\text{Hf}}$	2 SD error	$\frac{176\text{Hf}}{177\text{Hf}}$	2s.e. on 6th digit	ppm Hf	ϵHf
WR	0.01770	0.0009	0.281483	15	3.798	+24.9
Ol-fine	0.02030	0.0006	0.281650	15	2.444	+30.9
Pl-pure	0.02320	0.0008	0.281822	15	1.993	+37.0
Ol-pure	0.03800	0.0006	0.282699	15	1.379	+68.3
Pi-pure	0.02730	0.0011	0.282037	15	2.436	+44.7
Ol--fine	0.02030	0.0006	0.281655	15	3.798	+31.1
Ol-fine	0.02030	0.0006	0.281644	15	3.798	+30.7
Pl-fine	0.001300	0.0006	0.281629	470	51.085	+30.1
Pi-pkd	0.008000	0.0006	0.281999	720	11.163	+43.3
Pl-pkd	0.01150	0.0012	0.281075	30	6.0197	+10.4

WR: Whole Rock Ol: Olivine, Pl: Plagioclase, Pi: Pigeonite

	ppm Sm	ppm Nd	$\frac{147\text{Sm}}{144\text{Nd}}$	2 s.d. on 4th digit	$\frac{143\text{Nd}}{144\text{Nd}}$	2 s.d. on 6th digit
WR	4.615	16.688	0.1671	2.0	0.511623	8.0
Pl-fine	4.816	17.240	0.1689	2.0	0.511765	11.0
Ol-fine	2.356	7.818	0.1822	2.0	0.511998	11.0
Pi-pure	2.945	8.736	0.2038	2.0	0.512461	7.0
Ol-pure	1.410	4.303	0.1981	2.0	0.512353	26.0
Pl-pure	2.461	8.866	0.1678	2.0	0.512004	7.0
Pi-pkd	7.578	27.297	0.1678	2.0	0.511691	8.0
Pl-pkd	6.787	26.084	0.1573	2.0	0.511555	8.0
Pi-pkd	7.578	27.297	0.1678	2.0	0.511691	8.0
Pi-pkd	7.578	27.297	0.1678	2.0	0.511691	8.0
Ol-pkd	6.218	22.964	0.1636	2.0	0.511688	8.0
WR: Whole Rock Ol: Olivine, Pl: Plagioclase, Pi: Pigeonite						

	Rb ppm	Sr ppm	$\frac{87\text{Rb}}{86\text{Sr}}$	2 s.d. on 4th digit	$\frac{87\text{Sr}}{86\text{Sr}}$	2 s.d. on 6th digit
Whole Rock	1.756	53.559	0.0949	8.4	0.710427	6.2
Whole Rock	1.763	53.575	0.0952	8.8	0.710417	5.7
Pl-fine	4.295	83.809	0.148	8.1	0.711940	7.6
Ol-fine	0.690	33.237	0.0601	10.8	0.710674	5.7
Ol-fine	0.690	33.228	0.0601	8.0	0.710667	5.8
Pl-pkd	2.819	111.203	0.0734	8.2	0.707792	6.7
Pl-pkd	2.819	111.211	0.0733	9.5	0.707780	7.3
Pl-pure	1.976	98.447	0.0581	10.3	0.706989	8.8
Pi-pkd	1.530	63.812	0.0694	12.5	0.710092	5.7
Pi-pure	0.682	44.569	0.0443	8.1	0.709364	7.0
Ol-pkd	1.040	42.300	0.0711	9.9	0.711524	7.6
Ol-pure	0.575	31.324	0.0532	10.8	0.709648	6.3
Ol-pure	0.575	31.320	0.0532	8.9	0.709656	7.3
Ol-pure	0.366	31.323	0.0338	10.3	0.709598	8.6
Ol-pure	0.366	31.321	0.0338	12.2	0.709591	6.3
WR: Whole Rock Ol: Olivine, Pl: Plagioclase, Pi: Pigeonite						

6.0 New Evidence for an Old Moon

*Science demands a terrible price –
that we accept what experiments tell us about the universe,
whether we like it or not.*

Existence

By D. Brin

2012

6.1.0 Introduction

The Moon likely formed in the aftermath of a giant impact between the proto-Earth and an erstwhile planetary body (Canup, 2012). Extreme chemical and isotopic similarities between the Earth and the Moon (Melosh, 2014) have led to a growing consensus that Earth and Moon share a common chemical ancestry. This similarity in chemical signatures imply either that the bulk silicate Earth (BSE) is the major source of Moon-forming impact debris (Armytage *et al.*, 2012; Dauphas *et al.*, 2014; Weyer *et al.*, 2005; Zhang *et al.*, 2012) or that proto-Earth and the impactor had virtually identical chemical compositions (Dauphas *et al.*, 2014). Beyond chemical constraints on the Moon forming giant impact event, there is an ongoing controversy regarding its exact timing, with some researchers arguing that the Moon formed early (i.e., 30 to 100 Myrs after Solar System formation – SSF) (Barboni *et al.*, 2017, Bottke *et al.*, 2015; Jacobson *et al.*, 2014; Yin *et al.*, 2014), whereas others contend the Moon formed up to 200 Myrs after SSF (Borg *et al.*, 2011; Carlson *et al.*, 2014; Connelly and Bizzarro, 2016; Snape *et al.*, 2016).

Constraining lunar formation requires knowing the crystallization age of the lunar magma ocean (LMO), the result of the Moon’s high-energy impact formation. Central to this controversy are small but resolvable excesses in the ^{182}W abundance in lunar basalts when compared to the Earth, which average a value of $+0.25 \epsilon^{182}\text{W}$ units (Kruijer *et al.*, 2015; Kruijer and Kleine, 2017; Touboul *et al.*, 2015). The excess ^{182}W in lunar samples stems from the decay of short-lived ^{182}Hf to ^{182}W (8.9 Myrs half-life, Vockenhuber *et al.*, 2004). This signature, if it evolved in-situ, places lunar formation between 30 and 60 Myrs after SSF when sufficient ^{182}Hf was still present. However, this interpretation is at odds with the apparent observation that BSE and the silicate Moon have virtually overlapping ratios of Hf (mother) to W (daughter), with a Hf/W of 24.9 and 25.8, respectively (König *et al.*, 2011; Münker, 2010). These apparently identical

parent to daughter ratios imply that their different $\epsilon^{182}\text{W}$ cannot be related to the *in situ* decay of ^{182}Hf . An alternate explanation invoked for this dichotomy is that the Earth and Moon received a disproportionate and variable contribution of late accretion components with a chondritic Hf/W (~1) and lower ^{182}W than BSE (Kruijer *et al.*, 2015). Because the Moon is less massive than Earth, it received a commensurately smaller contribution from late accretion, and has thus retained a higher $\epsilon^{182}\text{W}$ than BSE (Kruijer *et al.*, 2015; Kruijer and Kleine, 2017; Touboul *et al.*, 2015). The Moon therefore constitutes a suitable highly-siderophile element (HSE) poor end-member in such late accretion models and a possible analogue to a proto-Earth that was essentially devoid of late accretion components (König *et al.*, 2011). In addition to this view, the apparent decrease in ^{182}W values measured in terrestrial rocks over geologic time has been explained by the protracted mixing of late veneer material into the terrestrial mantle that lowered $\epsilon^{182}\text{W}$ to its present-day value (Rizo *et al.*, 2016; Touboul *et al.*, 2015; Willbold *et al.*, 2011). This interpretation of lunar ^{182}W systematics implies that the Moon must have formed after the Hf-W system was extinct, i.e., it cannot have formed prior to 60 Myrs after solar system formation (SSF) (Kruijer *et al.*, 2015; Kruijer and Kleine, 2017).

Any accurate interpretation of ^{182}W data measured in lunar samples relies on a precise knowledge of the Hf/W value in lunar mantle reservoirs and by inference of the silicate Moon. Unfortunately, lunar Hf/W systematics are poorly constrained, as data of sufficient precision are scarce. This also extends to other highly incompatible elements (e.g., Th and U) that are commonly used as proxies for W behaviour during dry terrestrial mantle melting (König *et al.*, 2011). In previous lunar studies, W was treated as a perfectly incompatible element (i.e., having a similar behaviour as U or Th) during lunar differentiation. This treatment might be incorrect, as lunar mantle melting occurs at more reducing conditions than in the terrestrial mantle, implying that W may behave differently to incompatible elements like U and Th (Fonseca *et*

al., 2014; Leitzke *et al.*, 2016; Leitzke *et al.*, 2017). In fact, even previous observations that ratios of W with U or Th appear to be variable in lunar samples suggest that W may behave differently to highly incompatible elements like U or Th during lunar magmatism (Palme and Rammensee, 1981), in line with recent results of experimental studies (Fonseca *et al.*, 2014; Leitzke *et al.*, 2016; Leitzke *et al.*, 2017).

6.2.0 Methods and Results

To provide robust constraints on the Hf/W value of the silicate Moon, and ultimately understand the observed $\epsilon^{182}\text{W}$ excess recorded in lunar samples, we performed high-precision concentration measurements of W, Th, U, and other high field strength elements (HFSE) by isotope-dilution on a representative sample suite covering most relevant lithological units on the nearside of the Moon. Our samples include low- and high-Ti basalts, ferroan-anorthosites (FAN), and KREEP-rich rocks. Results are reported in table 6.1.

6.2.1 Sample selection

Lunar samples were provided by the Curation and Analysis Planning Team for Extraterrestrial Materials (CAPTEM), and selected to represent the major lithological units of the Moon as sampled by the NASA Apollo missions. Characterizing their chemical composition, our particular focus lay on the quantification of any inherent U/W, Th/W, and Hf/W variability as inferred from the few previous studies available. Some sample duplicity with previous studies allows for an additional quality assessment. In total, lunar samples from Apollo 11 (3), Apollo 12 (6), Apollo 14 (3), Apollo 15 (6), Apollo 16 (4), and Apollo 17 (4) were analyzed. Of these, 7 were Apollo 11 or Apollo 17 high-Ti mare basalts and soils, 14 were low-Ti mare basalts from Apollo 12 and 15, 2 Apollo 16 ferroan-

anorthosites (FAN), as well as 7 KREEP-rich samples including a meteorite and KREEP-rich breccias and KREEP-basalts from the Apollo 14, 16, and 17 missions.

6.2.2 Sample Preparation

To obtain high precision data, we measured all elements of interest by isotope dilution and added several isotope tracers to ca. 100 mg (250 mg for anorthosites) of each sample prior to digestion. The mixed isotope tracers included ^{229}Th - ^{233}U - ^{236}U and ^{183}W - ^{180}Ta - ^{180}Hf - ^{176}Lu - ^{94}Zr mixed solutions. Samples were digested in 3 ml of double distilled HF and 3 ml of distilled HNO_3 for 24 hours at 120 °C. Prior to drydown, 0.5 ml of perchloric acid were added to ensure sample-spike equilibrium for Th. Samples were re-dissolved with concentrated HNO_3 and trace 0.5M HCl-0.5M HF to ensure re-dissolution of HFSE. These sample solutions were subsequently dried down again, and re-dissolved in 6 ml 6 M HCl- 0.06 M HF to ensure sample-spike equilibrium for HFSE. These samples were then aliquoted, with 10% of the solution being used for conventional trace element analysis, 20% for W isotope dilution measurements, and 70% for high field strength and U-Th element analysis. For a first batch of samples, an additional aliquot of 10% for U-Th was taken. The anorthosite samples were aliquoted with 85% to a combined HFSE, W, and U-Th aliquot, and 15% for trace element analysis.

The trace element aliquot was dried down, dissolved in concentrated HNO_3 , and then dried down again. This residue was subsequently dissolved in 1 ml concentrated HNO_3 , with 4 ml MQ H_2O added, and then diluted with MQ H_2O to 50 ml. Conventional trace elements on these aliquots were performed at the Quadrupole ICP-MS laboratory at the Institut für Geowissenschaften at CAU zu Kiel using the procedure of Garbe-Schönberg 1993.

Ion-exchange chromatography generally consists of a stationary and a mobile phase. Our stationary phase are commercially available ion exchange resins which separate inorganic anions and cations. Initially all samples are dissolved in a mobile phase, i.e., acids. By adding the mobile phase containing the sample to the stationary phase the sample interacts with both phases and according to the partition coefficient the different components of the sample solution partition into the different phases (Schönbächler *et al.*, 2014). For isotope measurements we separated Lu, Hf, Rb, Sr, Sm, and Nd in a clean laboratory environment with columns specifically calibrated for this purpose. Separation of the elements of interest from their matrix is important for an interference free measurement of the isotopic and element abundance and composition.

For the separation we used 3 different types of columns: Biorad AG 50 W x8 200 400 mesh (columns 1 and 4), Triskem Ln Resin (column 2), Biorad AG 1x8 (column 3). For a purer separation other columns were later used for separation of Rb, Sr, Sm, and Nd (Biorad AG 50W x8 and Triskem Ln Resin).

As the first step column 1 is cleaned with one full Reservoir of 6M HCl and rinsed twice with MQ (H₂O) as a backwash. One full reservoir of 2M HF is used as a second cleaning step and two full reservoirs afterwards of 6M HCl. After the column cleaning 3 times 2ml MQ are added to backwash again. For conditioning we used 2ml 1M HCl-1-2vol% H₂O₂. The samples are loaded in 2ml 1M HCl-1-2% H₂O₂. 0.5ml and afterwards 2ml of 1M HCl 1-2% H₂O₂ is used to collect a Hf-bearing cut. Matrix-1 is eluted with 2 times 4ml 1.5M HCl. With 4ml 1.5M HCl we collected Rb. Matrix-2 eluted with 10ml 1.5M HCl was combined with Matrix1. Sr was then collected with 8ml 1.5M HCl. Matrix-3 combined with one and two is eluted with 8ml 1.5M HCl. The second to last step is the collection of HREE, containing also the Lu-cut, in 8ml 2.5M HCl. The LREE are collected with 6ml HCl.

The pre-cleaning of column 2 is performed sequentially with 1rv 6M HCl, 1rv 2M HF, 1rv 6M HCl, 1rv 2M HF, and 2ml MQ (H₂O). To condition we used two times 2ml of 1M HCl-2% H₂O₂. We loaded the columns directly with the Hf-cut from column 1. With 3 times 4.7ml, 7ml and two times 5ml 1M HCl-2vol% H₂O₂ we collected the Ti-cut. After the Ti-cut we rinsed the columns with two times 2ml 1M HCl and eluted the Hf afterwards with two times 2 ml, and 6ml 2M HF.

Column 3 is cleaned with 5ml 3M HNO₃ and half a reservoir of 2M HF. The Hf cut from column 2 is loaded onto column 3. The Matrix is eluted in three times 2ml of 2M HF. The final Hf-cut is collected in two times 2ml and 6ml of 6MHCl. This cut is then dried down and afterwards we added 0.56M HNO₃-0.24M HF: H₂O₂ (9:1). The samples have been put on a HP at 90° for ca. 1 h before running on the mass spectrometer.

On column 4 we loaded the HREE cut from column 1 that contained Lu in 1ml of 1M HCl. The Matrix is collected into the LREE beaker from the column cut in 1ml, 10ml and 1ml of 1M HCl. Lu is eluted in 2ml and 10ml of 6M HCl. The LREE cuts from column 1 and 4 contain Sm and Nd. These elements are separated with different columns.

The Rb and Sr cuts from column 1 were dried down. After the samples were completely dry we added 0.3 ml 3M nitric acid on each sample. For clean Rb and Sr cuts we used columns containing Triskem Sr spec that have been calibrated for this purpose. First the columns need to be cleaned 7 times with 300µl 3 N HNO₃ and 7 times with 300µl 0.06 N HNO₃. Seven times 300µl 3N HNO₃ has been used for conditioning of the columns. After conditioning the Rb-cut in 300µl 3N HNO₃ is loaded onto the columns. Rb is then eluted again in 7 times 300µl 3N HNO₃. Seven times 0.06 N HNO₃ is used to rinse the Rb-Matrix. Before loading the Sr-cut we reconditioned the columns with 7 times 0.06N HNO₃. The Sr-cut from column 1 in 300µl 3 N HNO₃ is loaded on to the

columns and collected in the Rb-cuts. The Sr-Matrix is also collected into the Rb-tubes and therefore rinsed in 7 times 300µl 0.06 N HNO₃. Finally, the Sr-cut is eluted in 7 times 300 µl 0.06 N HNO₃. The columns were then cleaned again for future use as in the precleaning steps.

Both element cuts for each sample are then dried down and afterwards dissolved again in 0.5 ml of 0.14 HNO₃:H₂O₂ (9:1). This mixture had to be dried down again and before measurement we added 0.14 N HNO₃ on all Rb and Sr- samples.

For the Sm-Nd chemistry we dissolved the LREE-cut in 350 µl 0.25 N calibrated HCl for one hour. The samples are then transferred into 1ml Eppendorf vials. For the ion exchange separation we only loaded the upper 300 µl (0,3ml) of each sample in columns.

The columns were equilibrated with half a reservoir of density-calibrated 0.25 N HCl, twice. A molarity of 0.25 N HCl yields about 75% Nd with < 10% Ce. The samples were loaded in 0.3 ml 0.25 N HCl (calibrated). They were then washed two times in 0.25 ml 0.25 N HCl to collect the Sm-cut. Subsequently the samples were rinsed in 3ml 0.25N HCl and afterwards the collection of Nd was done in 2 ml 0.25 N HCl. Samples that contain only a little Nd can be rinsed in 2.5 ml 0.25 N HCl and collected in 2.5 ml 0.75 N HCl to yield a 90% Nd cut with about 25 % Ce. After the final collection the Sm and Nd-cuts were dried down. Prior to measurement 0.14N HNO₃-H₂O₂ (9:1) was added to each sample.

Our protocol for separating individual HFSE and U-Th cuts from lunar samples is a modified protocol based on Münker *et al.* (2001), Kleine *et al.* (2004) and Münker (2010). During the protocol, individual cuts containing a matrix, HRRE, Zr-Nb, Ta, Hf and U-Th were separated from the HFSE aliquot.

Tungsten was separated from the W isotope dilution step via a separate set of anion exchange resin microcolumns (after Kleine *et al.* 2004, Table 4).

In our HFSE protocol, the sample aliquots were dissolved in 3N HCl and loaded onto a Ln Spec resin column. Matrix and LREE were eluted in 3M HCl. An HREE fraction containing most Lu was eluted with 6N HCl, followed by elution of an HFSE cut containing Ti-Zr-Nb-Hf-Ta-U-Th in 2N HF. A quantitative Zr/Nb aliquot was taken from this fraction (see Münker *et al.* 2001). The remaining HFSE cut was loaded onto a Bio-Rad column containing AG 1 x8 100-200 mesh resin. The U-Th fraction was collected in 2N HF, and a Ti-Zr-Hf fraction was collected in 6N HNO₃/0.2N HF. A clean Ta fraction was subsequently collected in 6N HNO₃/0.2N HF/1%H₂O₂. The Ti-Zr-Hf fraction was dried down overnight and loaded onto the stage I Ln Spec resin column in 3 N HCl. After cleanup in 6N HCl and MQ H₂O, Ti was eluted using a 1N HNO₃ 2% - H₂O₂ mixture (Bast *et al.* 2015), and some Zr in 6N HCl -0.06N HF. Hf was finally eluted in 2N HF.

U-Th separation was performed in two ways, following a modified protocol of Luo *et al.* (1997). For the first batch of samples, a full aliquot was used, whereas for the other batches the U-Th fraction from the 2N HF elution step above was taken. After drydown, the U and Th bearing cuts were dissolved in 1.5N HNO₃, before being loaded onto columns containing Tru-Spec resin (200-400 mesh). Modifying the chemistry of Luo *et al.* (1997), all major elements were initially eluted in 1.5N HNO₃. After removal of rare earth elements in 3N HCl, Th was subsequently eluted in 0.2N HCl. Finally, U was eluted in 0.1N HCl/0.3N HF.

Given the low concentrations of elements of interest in anorthosites, we performed a different separation protocol for these samples. Ca. 70% of the 85% HFSE aliquots of anorthosites were loaded on anion exchange resin in 1N HCl/0.5N HF solution. The eluted matrix cut and an additional fraction rinses

in 0.5N HCl/0.5NHF contained most of the Rb-Sr, Sm-Nd and U-Th. A fraction containing Ti/Zr/Hf was collected in 6NHCl/0.06NHF, from which Hf was further purified using Ln Spec resin (see above). A W fraction was subsequently eluted in 6N HNO₃/0.2N HF, followed by Ta elution in 6 N HNO₃ / 0.2N HF / 1% H₂O₂. After drydown, the Ta cut was loaded on the same anion resin column for cleanup, and the Ta was again eluted in 6N HNO₃/0.2N HF / 1% H₂O₂ after cleanup in 6N HNO₃/0.2N HF. The remaining 15% of the anorthosite HFSE aliquots were loaded on Ln Spec resin in 3N HCl. Two fractions containing HREE and Zr/Nb were eluted from the column in 6N HCl and 2N HF as described above. The advantage of this approach is that a larger W fraction is collected, thus avoiding low sample-to-blank ratios during W ID measurements.

6.2.3 Analytical protocols

All isotope dilution measurements were performed using the Neptune MC-ICP-MS at Cologne. Detailed descriptions of the analytical protocols for HFSE measurements, analytical uncertainties and further references are given in Münker (2010). For ²²⁹Th/²³²Th measurements, we used an SEM ion counter equipped with an RPQ system on mass ²²⁹Th. The Th cuts were doped with the NBL CRM 112A U standard for mass bias correction, and the ion counter was calibrated with concentration-matched IRM-035 and IRM 036 standards for ion counter yield corrections. For U measurements, mass bias was corrected using the measured ²³³U/²³⁶U of the spiked U cuts and the certified ²³³U/²³⁶U from Richter *et al.* (2010) for the doped IRM-3636 double spike that was used for preparation of the mixed U-Th tracer. Our external precision and accuracy for elemental ratios determined by isotope dilution involving U and Th typically is better than ±1% for both U/W and Th/W (2σ r.s.d.). Typical blanks during the course of the measurements were below 50 pg for W, 66 pg for U, 32 pg for Th,

and 30 pg for Hf. These blanks proved negligible, with total blank-uncertainty-including propagated errors of less than $\pm 1\%$.

6.2.4 Results - modeling constraints

Measured HFSE and HFSE/U-Th ratios are distinct for different sample groups and mineralogy, with only small variations in U/W and Hf/W between samples from the same lithology. High-Ti basalts are particularly heterogeneous, with samples from the three measured localities showing distinct Hf/W and U/W values. Apollo 17 High-Ti breccias both have similar values, with Hf/W ranging from 31 to 35, at a constant U/W of 1.9. This is distinct from Apollo 17 high-Ti mare basalts, where U/W correlates positively with Hf/W. The Apollo 11 high-Ti mare basalts both have Hf/W of 42 and U/W of 2.2. Unique amongst all samples are the Apollo 17 high-Ti mare basalts, which bear exceptionally high Hf/W ratios, between 120 and 150. Likewise, the low-Ti basalts plot as particularly distinctive groups according to mission site. The Apollo 12 ilmenite basalts have similar U/W to the Apollo 12 olivine and pigeonite basalts, of 2.07 and 2.2, respectively. However, they are distinct in their Hf/W, with both pigeonite-bearing basalts near 30 and ilmenite-basalts of 43-48. The Apollo 15 quartz-normative and olivine-normative low-Ti basalts have different U/W, ranging from an average of 2.45 in the former to 1.7 in the latter. The Hf/W of the two low-Ti basalt groups also vary from 45 (quartz-normative) to 30 (olivine normative). Whereas the olivine-normative low-Ti basalts of both Apollo 15 and Apollo 12 have identical Hf/W, their U/W differ significantly, from amongst the lowest values (1.63) measured to the highest (2.53). The KREEP-rich samples have a very narrow range in Hf/W of ca. 20. The U/W of KREEP samples has the largest spread, with most samples ranging from of 1.6 to 2.7, and minimum and maximum values of 0.5 and 3.5, respectively.

6.2.5 Lunar Magma Ocean fractionation and partial melting modeling

The Lunar Magma Ocean (LMO - Smith *et al.*, 1970; Warren, 1985; Wood *et al.*, 1970) crystallization model utilized in this study is based on the cumulate crystallization sequence of Snyder *et al.* (1992). It has been previously shown (Fonseca *et al.*, 2014) that the results of this and other LMO crystallization models (e.g., Elardo *et al.*, 2011; Elkins-Tanton *et al.*, 2011) are in good agreement. The same starting composition used in Fonseca *et al.* (2014) after Münker (2010) was chosen to evaluate the general HFSE-W-U-Th systematics of a crystallizing LMO. For W, an additional mass balance between the estimate of its content in the bulk silicate Moon after core formation was done following Steenstra *et al.* (2016), considering different core mass fractions (1-3% of the total mass of the Moon). The LMO crystallization model is divided into four main steps: (i) equilibrium crystallization of olivine and orthopyroxene (until 78% solidification), (ii) fractional crystallization of plagioclase, olivine, and pigeonite (until 86% solidification), (iii) fractional crystallization of clinopyroxene, plagioclase, and pigeonite (until 95% solidification), and (iv) crystallization of pigeonite, plagioclase, clinopyroxene, and ilmenite (until 99.5% solidification). The remaining 0.5% after LMO crystallization is a liquid residue strongly enriched in incompatible trace elements and called urKREEP, which reflects its characteristic enrichments in K, REE, and P (Meyer *et al.*, 1971; Warren and Wasson, 1979). The LMO crystallization model assumes that various amounts of trapped instantaneous residual liquid (TIRL, i.e. coexisting melt at the time of crystallization) are part of lunar mantle cumulates in order to take into account major element variation observed in lunar mare basalts (Snyder *et al.*, 1992). The model also considers that at the moment plagioclase appears on the liquidus, 98% of the crystallizing plagioclase floated to the uppermost portion of the LMO to form the lunar crust with only 2% being entrained in the cumulates, in order to account for the Al content of lunar basaltic samples (Snyder *et al.*, 1992). Following LMO crystallization, the

layered lunar mantle underwent a density driven mantle overturn which mixed the different cumulate layers, producing new hybrid mantle domains that served as the source for partial melts that crystallized to form the lunar mare basalts (e.g., Hess and Parmentier, 1995). To understand the implications of these processes for the trace element inventory of mare basalts thus involved aggregate modal fractional melting models of hybrid lunar mantle domains. The mixing proportions of different primary LMO cumulates in the hybridized lunar mantle sources, their mineral assemblages, as well as the amount of trapped instantaneous residual liquid (TIRL) were constrained from the Lu–Hf and Sm–Nd isotope patterns of lunar basalts (Sprung *et al.*, 2013). We have also assumed that a small proportion of residual metal may be required at the lunar mantle source to reproduce the values observed for high-Ti basalts, which is in agreement with the extremely reduced nature of the lunar mantle and the depletion in Ni observed for lunar olivine (e.g., Karner *et al.*, 2000; Nicholis and Rutherford, 2009). A lunar magma ocean equilibrated at ca. IW –1 was assumed throughout the entire modelling, in agreement with the current estimates of oxygen fugacity for the lunar mantle (Papike 2005; Nicholis and Rutherford, 2009). Trace element crystal/silicate melt partition coefficients for different pyroxenes, plagioclase, and olivine (Table 6.2) were selected taking into account the variation of TiO₂ exhibited by lunar mare basalts and the changing composition of the LMO during crystallization (see Leitzke *et al.*, 2016) as well as the effect of fO₂ on the partitioning behavior of W (see Fonseca *et al.*, 2014; Leitzke *et al.*, 2017). Ilmenite/silicate melt trace element partition coefficients are an average of the high-Ti experiments listed in Dygert *et al.* (2013), and reported in table 6.2. Liquid metal/silicate melt W partition coefficients are from Righter *et al.* (2010) and Steenstra *et al.* (2016), which cover a wide range of values (15-100).

6.2.6 Results

As shown in Figure 1, these groups of samples are compositionally distinct, as expected from radiogenic isotope evidence and geochemical modelling (Sprung *et al.*, 2013). Low-Ti mare basalts display a narrow range in U/W and Hf/W between 1.5 and 2.5 and between 30 and 50, respectively. In contrast, high-Ti basalts have Hf/W as high as 150, and slightly more fractionated U/W, with values between 0.5 and 2.2. Finally, the KREEP-rich rocks and FAN samples exhibit the lowest Hf/W range of the studied sample suite, between ca. 5 (FAN) and 23 (KREEP-rich), while their U/W shows the largest range amongst all samples, with values approaching zero for FAN and as high as 3.5 for the KREEP-rich rocks.

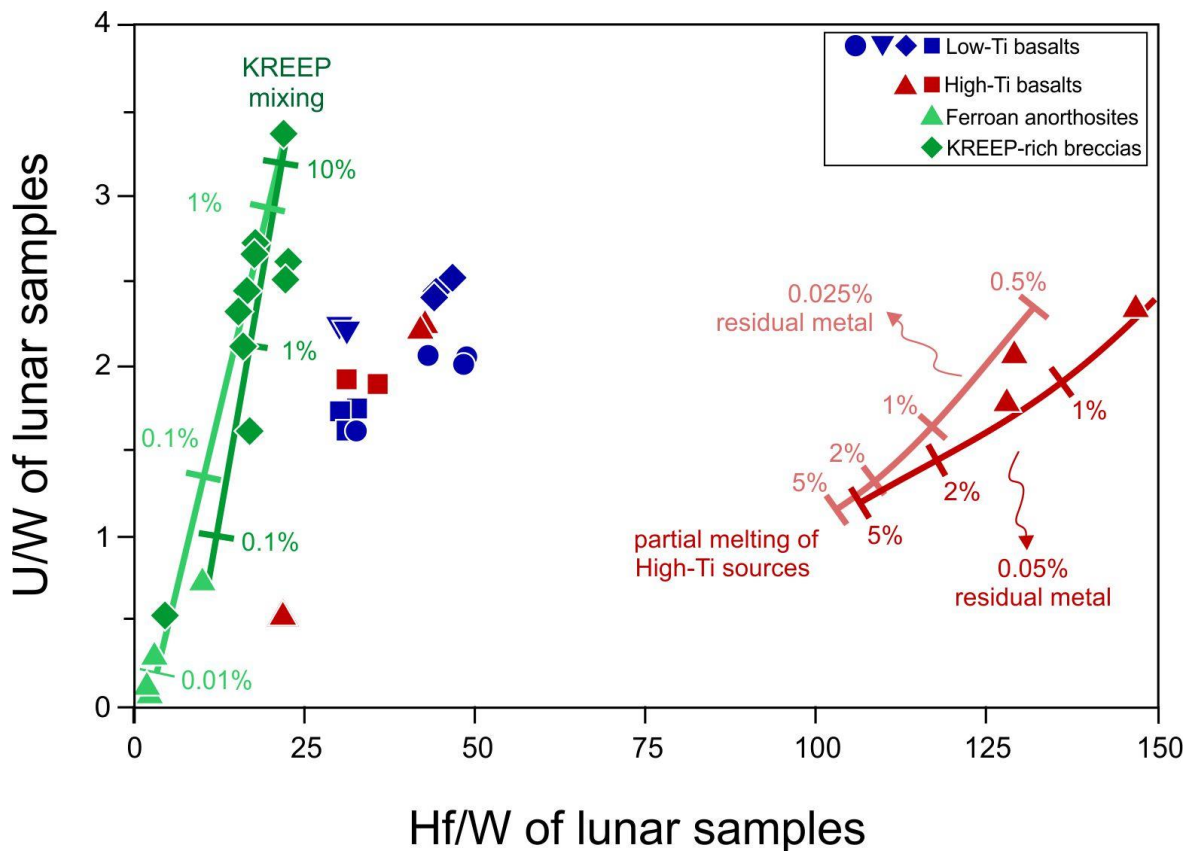


Figure 6.1 - New U/W vs. Hf/W data measured in lunar samples compared to crystallization and melting models for the LMO²⁸. Measured compositions of lunar highland breccias straddle mixing lines between a KREEP-enriched end-member²⁴ and Ferroan anorthosite compositions as determined in this study.

Contamination with meteoritic components rich in W produces virtually identical trajectories and raises the absolute W content as evident in sample 65015. Apollo 17 high-Ti mare basalts: The source mineral assemblage is defined by a mixture of LMO cumulates whose proportions provide a compositional match to the Hf and Nd isotope systematics of Apollo 17 mare basalts^{24-26,28}. Low-Ti mare basalts: Melting models following the same principle would result in compositions identical to our data for degrees of melting >10% because residual source components that preferentially incorporate W over Hf or W are absent.

6.4.0 Discussion

Several key observations can be derived from our high precision W-U-Th-HFSE data. For example, when combined, the FAN and KREEP-rich rocks form a clear linear array in Hf/W vs. U/W space (Fig. 1). This array can directly be linked to early lunar crust formation, i.e., likely the result of mixing between a FAN end-member that has exceedingly low Hf/W and U/W, and a KREEP-like component having elevated U/W and a Hf/W of around 20 (i.e., lower than both bulk silicate Moon and Earth's mantle (grey lines in Figure 1)). Interestingly, our results for these KREEP-rich samples corroborate previously modelled U/W and Hf/W values for KREEP using a fO_2 -sensitive set of partition coefficients (Fonseca *et al.*, 2014), which predicted that KREEP has an elevated U/W and a lower Hf/W value than the bulk silicate Moon depending on fO_2 . Our data thus show that the LMO crystallization model (Snyder *et al.*, 1992), as well as the mineral/melt partitioning data (Rizo *et al.*, 2016; Willbold *et al.*, 2011) used here, are sufficiently robust for mass balancing these elements.

Our new results for lunar mare basalts have the best potential to constrain the Hf/W of the silicate Moon. In defining which lunar mantle reservoirs of LMO cumulates were involved in the genesis of mare basalts, radiogenic Hf-Nd isotope data are the most powerful proxies to constrain their

source mineral assemblages (Sprung *et al.*, 2013). If applied to the mare basalt groups investigated in this study, these source mineral assemblages allow us to model the geochemical relation between basalt and mantle compositions for trace elements of interest. For example, Hf-Nd isotope data can clearly identify late-crystallizing mare basalt sources comprising Ti-rich oxide phases and clinopyroxene, a characteristic that is absent from low-Ti mare basalt source regions (Sprung *et al.*, 2013). Even at the low fO_2 of the lunar mantle, such oxide phases and clinopyroxene preferentially incorporate Hf over W and U (Leitzke *et al.*, 2016; Dygert *et al.*, 2013). Moreover, the mantle source of the Apollo 17 high-Ti mare basalts is the most likely lunar mantle source to contain residual metal during partial melting, owing to its reduced nature (Fonseca *et al.*, 2014; Leitzke *et al.*, 2016). Residual metal in lunar mantle sources would undoubtedly retain W and not Hf, and thus generate higher Hf/W in co-existing mare basalts. When modelling high-Ti mare basalts with small fractions of residual metal, the high-Ti samples that exhibit the highest Hf/W in our sample suite are perfectly reproduced (see melting curves shown in red in Figure 1). The extreme Hf/W displayed by Apollo 17 high-Ti mare basalts, and their co-variation with U/W (Figure 1), and therefore directly reflect the combined effects of residual Ti-rich oxides, pyroxene, and metal in the mantle sources of Apollo 17 high-Ti basalts. An unfortunate consequence of this feature is that any inferred U-W-Hf systematics strongly depend on the degree of partial melting that is not well constrained for Apollo 17 basalts. Thus, Apollo 17 high-Ti mare basalts cannot be used to infer the Hf/W of the bulk silicate Moon, as done previously (Kruijer and Kleine, 2017).

In contrast to the mantle sources of previously discussed sample types, those of low-Ti mare basalts are straightforward to model, as these are not overprinted by KREEP components and are essentially devoid of both Ti-rich oxides and metal (Sprung *et al.*, 2013). Thus, incompatible element ratios in low-Ti basalts are far more likely to mirror their lunar mantle sources, as their sources lack

phases that fractionate W from U, Th, or HFSE significantly. Moreover, low-Ti basalts are thought to result from higher-degrees of partial melting compared to high-Ti basalts (Day *et al.*, 2007; Day *et al.*, 2008; Day and Walker, 2015; Wade and Wood, 2005), and the U/W and Hf/W measured in these basalts should be virtually identical to those in their respective sources. Interestingly, there are clearly resolvable differences between the different groups of low-Ti basalt samples (Figure 1). This heterogeneity in Hf/W and U/W values in distinct low-Ti mantle sources is in perfect agreement with the isotopic heterogeneity documented by previously published Hf-Nd isotope data (Sprung *et al.*, 2013). Moreover, these variations in Hf/W and U/W observed in our lunar samples are consistent with previous experimental studies that predict that W is less incompatible than Hf during LMO crystallization and partial melting of lunar mantle cumulates (Fonseca *et al.*, 2014; Leitzke *et al.*, 2016).

Importantly, the mafic cumulates that comprise the mantle sources of low-Ti basalts are expected to retain W over Hf and U during LMO crystallization at reducing conditions (crystal/silicate melt partitioning values shown in). Therefore, the LMO cumulates, and by inference, the measured Hf/W of low-Ti lunar mantle sources (30.2 to 48.7) record minimum estimates of the Hf/W in the bulk LMO as well as of the silicate Moon. Altogether, our data therefore clearly show that the Hf/W of the silicate Moon must lie between 30 and 50, which is clearly higher than the value estimated for the BSE (25.8) (Münker, 2010).

In summary, low-Ti mare basalt have been shown above to allow the most reliable estimates of Hf/W in the lunar mantle, and the Hf/W of the lunar mantle can be clearly shown to be resolvably higher than that of Earth's mantle. There are three scenarios illustrated in Figure 2 that can explain this feature:

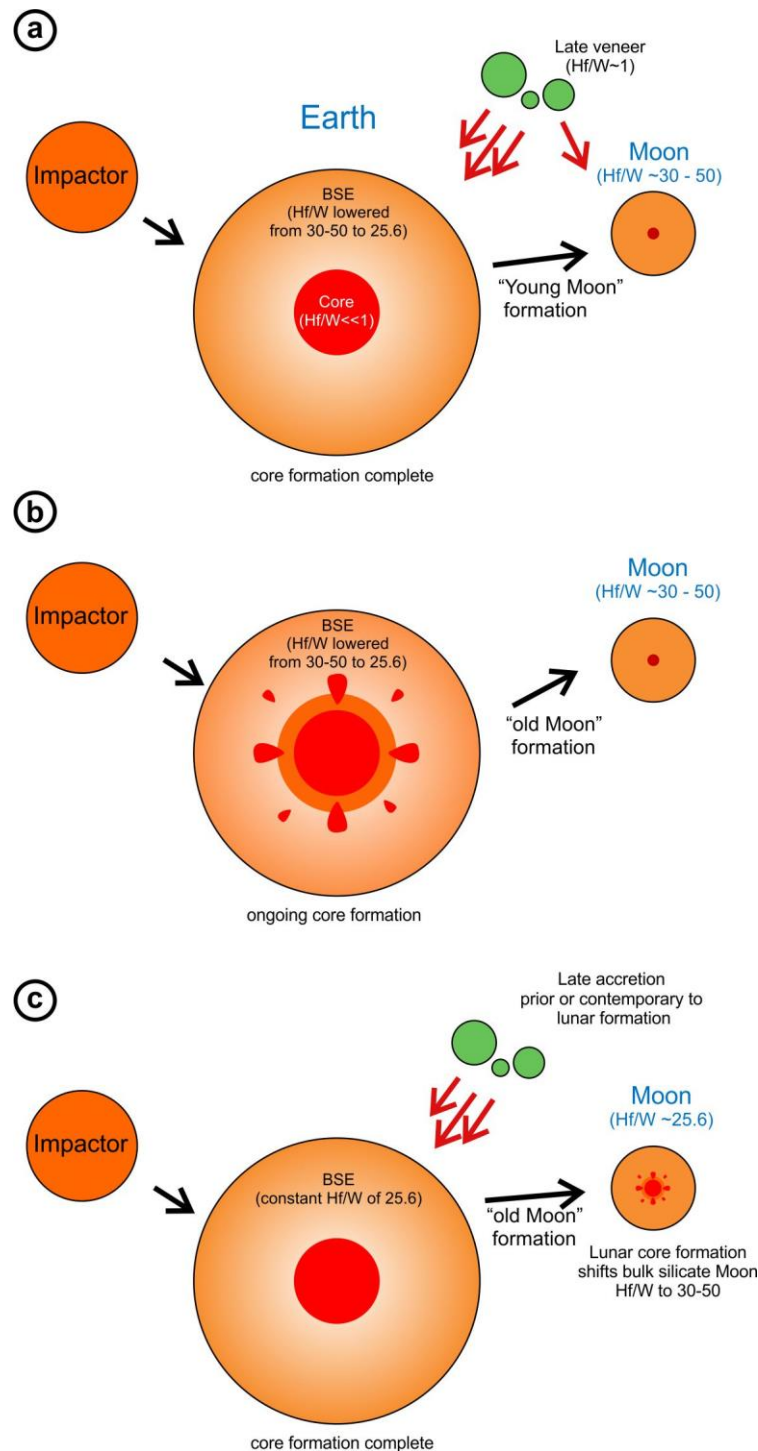


Figure 6.2 - Possible scenarios to account for the higher Hf/W ratio of the Bulk Silicate Moon (BSM). (a) Conventional model, where a late veneer of chondritic material (Hf/W~1) lowers the Hf/W of silicate Earth from ca. 30-50 to 25.6 after ^{182}Hf became extinct, but the Moon is less affected and preserves its original Hf/W. (b) The Moon forming event takes place while Earth's core is still forming and ^{182}Hf is extant. Increasingly oxidised conditions in silicate Earth lowered its

Hf/W after Moon formation. (c) The formation of a small lunar core took place while ^{182}Hf was still extant, and W was scavenged from the BSM increasing its Hf/W. In models (b) and (c), formation of the Moon must have occurred during the lifetime of ^{182}Hf , i.e., within the first 60 Myrs after solar system formation.

A first, traditional scenario (Fig. 2a) explains the different Hf/W by variable proportions of added late veneer. It has been suggested by several studies (Kruijer *et al.*, 2015; Kruijer and Kleine, 2017; Touboul *et al.*, 2015) that the Moon received a considerably lower proportion of late veneer than the BSE. The lower $\epsilon^{182}\text{W}$ and Hf/W of the BSE are then explained by the addition of a higher amount of unradiogenic W through late accretion to Earth than to the Moon. In a second scenario (Fig. 2b), the Moon forming event could have taken place amidst ongoing terrestrial core formation, when ^{182}Hf was still present. If the Moon formed that early, core formation has certainly been taking place at more reducing conditions than during its final stages (Wade and Wood, 2005; Wood *et al.*, 2006). Under such more reducing conditions, the Hf/W of BSE at the time of the giant impact would have been higher than at present, because W would have been more efficiently extracted into the growing core (Wade and Wood). This model obviates the need for late accretion to explain the lunar excess in $\epsilon^{182}\text{W}$, because the Moon preserved a higher Hf/W than the silicate Earth, leading to less radiogenic $\epsilon^{182}\text{W}$ in the BSE and more radiogenic $\epsilon^{182}\text{W}$ in the silicate Moon. In the third scenario (Fig. 2c), core formation in the Moon could have scavenged sufficient W into the lunar core to elevate the Hf/W of BSM to its higher present-day value. This process has been invoked previously, for example, to explain the depletion of Cr (Walter *et al.*, 2000) as well as that of other siderophile elements in the lunar mantle (Steenstra *et al.*, 2016). If the lunar core, and by inference the Moon, formed while the Hf-W system was extant, the silicate Moon would inevitably develop ^{182}W higher than the present day terrestrial value. Collectively, the two last scenarios imply that late accretion

was either of no consequence to the W budget and isotope composition of the silicate Moon, or that it was contemporaneous to the Moon forming event.

A simple strategy to further evaluate the three models described above is to test the simplest hypothesis to explain why the Hf/W of the silicate Moon is higher than that of BSE, i.e., lunar core formation (model III). If lunar core formation will raise the Hf/W of the silicate Moon to values as high as those shown here (i.e., 30-50), then the first two hypotheses are potentially superfluous. While there is plenty of evidence that the Moon has a small core, its exact composition and formation conditions are not well understood. However, the mass of the lunar core is much better constrained. Based on a recent re-evaluation of lunar seismic data (Garcia *et al.*, 2011, Khan *et al.*, 2013, Weber *et al.*, 2011) the lunar core comprises 1-3 % of the total mass of the Moon. The question remains whether such a small core could have scavenged sufficient W to shift the Hf/W of the silicate Moon to values as high as reported here. A simple mass balance (Rai and Van Westrenen, 2014) can be made to model the Hf/W of the silicate Moon after lunar core formation. This model assumes that Hf is perfectly lithophile, and that its abundance in the bulk Moon and the BSE are identical. The Hf-W contents of the modelled silicate Moon can be calculated assuming closed-system core formation, over a range of realistic $D_W^{core/mantle}$ (15-100), initial Hf/W of BSE (25.8), and different core mass fractions (1-3 %). The results of the modelling are depicted in Figure 3, showing that that lunar core formation can indeed reproduce the range of Hf/W of the lunar mantle if one assumes $D_W^{core/mantle}$ higher than 60, and a core mass fraction of at least 1.5%, i.e., in line with recent estimates³⁷⁻³⁹. A more massive core (3% mass fraction), would permit smaller $D_W^{core/mantle}$ (ca. 30) to reproduce the Hf/W range of 30-50 reported here. It is thus clear from the results of this model that lunar core formation can viably generate the Hf/W of BSM using

realistic values of $D_W^{core/mantle}$ and core mass fractions (Rai and Van Westrenen, 2014).

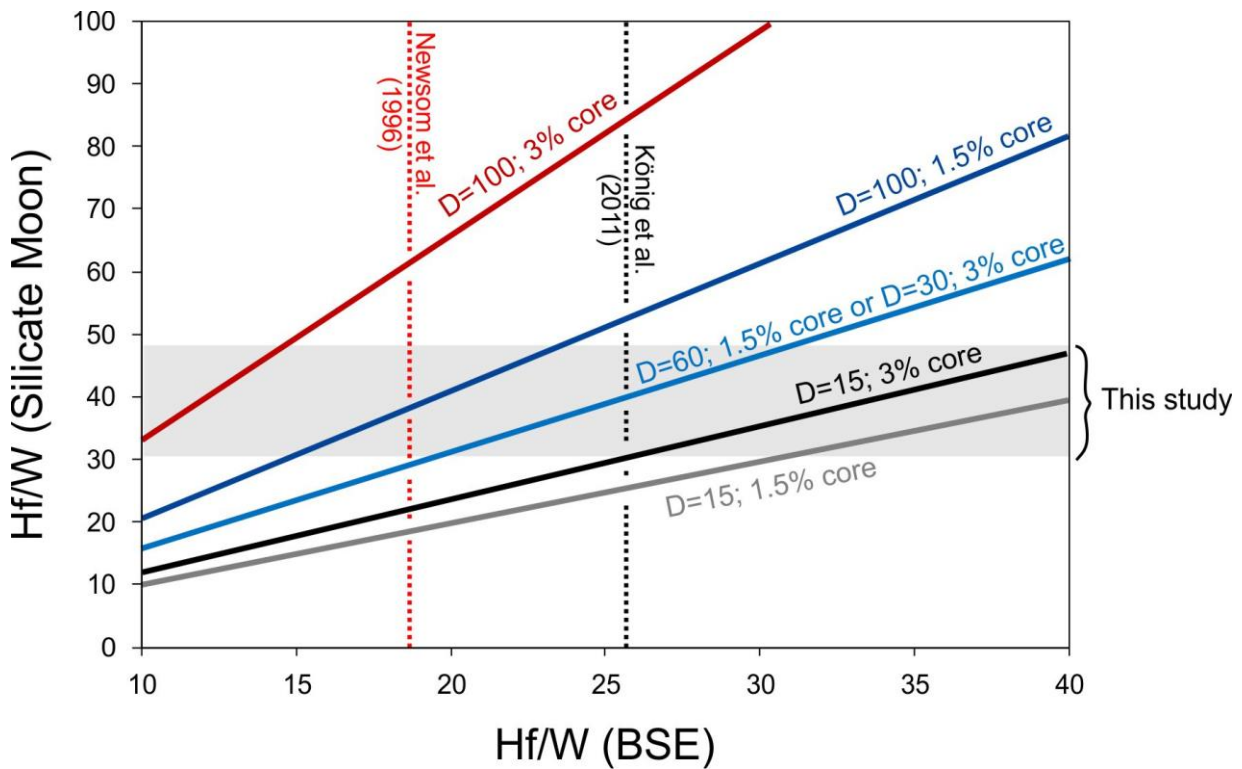


Figure 6.3 - The effect of lunar core formation on the Hf/W of the Silicate Moon. The models assume different metal–silicate partition coefficients for W ($D_W^{core/mantle}$ between 15–100), and different mass fractions of the lunar core (1–3%). The initial Hf/W of the Bulk Moon is assumed to be the same as that of the Bulk Silicate Earth. The lunar Hf/W value is reached with $D_W^{core/mantle}$ values between 30 and 60, and core mass fractions between 1 to 3% of the mass of the Moon.

6.5.0 Conclusions

In conclusion, we prefer a simple model, wherein the difference in Hf/W between the silicate Moon and the silicate Earth is the result of lunar core formation. Figure 4 illustrates variations of lunar ^{182}W systematics as a function of Hf/W and age. The range of Hf/W measured in our study, combined with recent estimates for the lunar $\epsilon^{182}\text{W}$ requires lunar differentiation to have occurred between 40.5 and ca. 60 Myrs after solar system formation. We can thus unambiguously explain the ^{182}W excess in lunar samples as being the consequence of in-situ decay of ^{182}Hf to ^{182}W . The combination of a robust set of experimental partitioning data with high precision HFSE analysis is thus in favour of an “old Moon,” while simultaneously diminishing the role of late accretion in creating the $\epsilon^{182}\text{W}$ signature of the Moon. In addition to helping settle the ongoing strife between “old” and “new” Moon scenarios, this method can also be used to unravel formation timescales of other planetary bodies, being of key importance to future sample return missions.

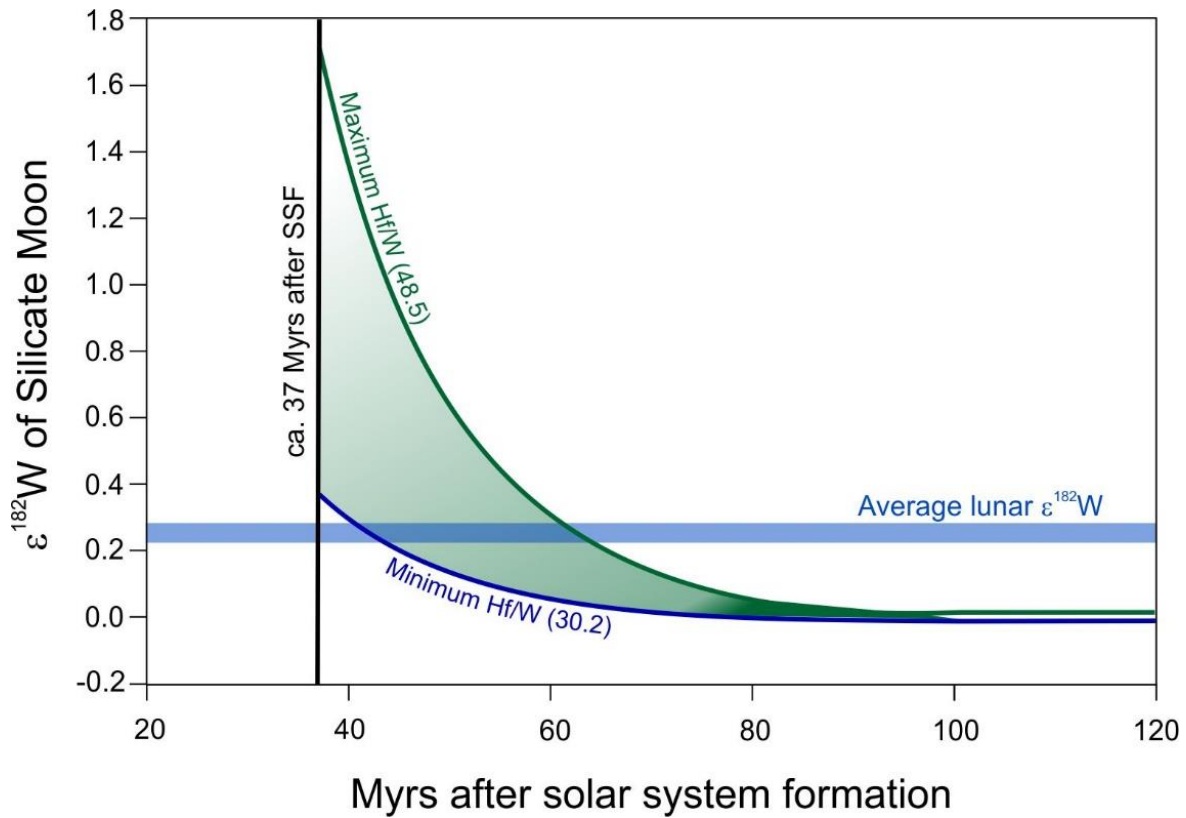


Figure 6.4 - Tungsten isotope composition (as $\epsilon^{182}\text{W}$) of the silicate Moon, modelled as a function of its Hf/W and formation age in comparison to the range of Hf/W in low-Ti mare basalts. The intersection with the mean reported pre-exposure $\epsilon^{182}\text{W}$ of the BSM provides the age at which the Moon must have formed to explain its $\epsilon^{182}\text{W}$ difference to Earth by in-situ decay of ^{182}Hf .

Table 6.1: Lunar Samples and Previous Data

Sample Name	Sample Type	W (ppm)	Th (ppm)	U (ppm)	Hf (ppm)	Zr (ppm)	Nb (ppm)	Ta (ppm)	W/U	Th/U	Zr/Nb	Zr/Hf	Sample weight (g)
10017	Ilmenite Basalt (high K)	0.382	3.404	0.858	16.3	491	30.4	1.82	0.446	3.97	16.1	30.05	0.099
10020	Ilmenite Basalt (low K)	0.331	0.667	0.180	7.31	201	17.5	1.10	0.545	3.69	11.5	27.50	0.107
10057	Ilmenite Basalt (high K)	0.386	3.56	0.856	16.2	490	30.7	1.81	2.217	4.17	16.0	30.18	0.101
12004	Olivine Basalt	0.115	0.959	0.260	3.49	114	7.78	0.406	2.256	3.69	14.7	32.76	0.103
12022	Ilmenite Basalt	0.0881	0.677	0.182	4.29	121	6.68	0.359	2.065	3.72	18.1	28.16	0.100
12051	Ilmenite Basalt	0.127	0.804	0.208	4.04	121	7.67	0.427	1.637	3.87	15.7	29.89	0.105
12053	Pigeonite Basalt	0.122	1.04	0.272	3.76	122	8.50	0.446	2.233	3.83	14.4	32.48	0.102
12054	Glass-coated Ilmenite Basalt	0.123	0.977	0.255	5.30	153	8.91	0.499	2.077	3.83	17.2	28.90	0.100
12063	Ilmenite Basalt	0.0850	0.661	0.172	4.10	115	6.62	0.376	2.028	3.84	17.4	28.14	0.099
14163	Bulk Soil Sample	1.49	13.0	3.50	23.2	931	63.7	2.89	2.344	3.71	14.6	40.14	0.104
14305	Crystalline Matrix Breccia	1.28	16.4	4.33	28.3	1163	73.6	3.26	3.383	3.79	15.8	41.03	0.103
14310	Feldspathic Basalt ?	1.21	10.9	2.98	20.1	817	51.4	2.31	2.462	3.66	15.9	40.66	0.104
15058	Pigeonite Basalt	0.0592	0.576	0.150	2.76	98	6.62	0.366	2.531	3.84	14.8	35.43	0.107
15065	Gabbroic Basalt	0.0895	0.863	0.216	3.96	139	10.0	0.522	2.412	4.00	14.0	35.17	0.102
15495	Vuggy Porphyritic Pigeonite Basalt	0.0692	0.670	0.169	3.07	110	6.80	0.380	2.448	3.96	16.2	35.90	0.103
15545	Olivine-normative Basalt	0.0810	0.491	0.132	2.53	85	6.15	0.374	1.635	3.71	13.8	33.37	0.105
15555	Olivine-normative Basalt	0.0633	0.432	0.112	2.09	70	5.01	0.304	1.770	3.86	14.0	33.58	0.106
15556	Vesicular Olivine-normative Basalt	0.0882	0.512	0.154	2.67	89	6.38	0.392	1.750	3.31	14.0	33.39	0.102
60025	Ferroan Anorthosite	0.00204	0.000661	0.000159	0.00371	0.141	0.0296	0.00128	0.5499	4.16	4.8	38.03	0.251
65015	Poikilitic Impact Melt Breccia	3.37	7.35	1.90	15.5	640	36.6	1.60	0.2175	3.88	17.5	41.24	0.103
67075	Crushed Ferroan Anorthosite	0.0117	0.039	0.00872	0.119	3.93	0.255	0.0125	0.743	4.52	15.4	33.14	0.250
68015	Glassy Polymict Breccia	0.549	4.45	1.17	8.92	360	23.8	0.974	2.128	3.80	15.1	40.35	0.066
72275	Fragmantal Polymict Breccia	0.924	5.84	1.51	15.9	658	31.0	1.40	1.638	3.86	21.2	41.38	0.103
73275	Micropoikilitic Impact melt Breccia	0.550	5.23	1.39	12.2	486	29.5	1.43	2.527	3.76	16.5	39.95	0.104
74255	Ilmenite Basalt	0.0636	0.450	0.132	8.21	221	25.9	1.43	2.071	3.42	8.52	26.92	0.103
74275	Oriented Ilmenite Basalt	0.0590	0.466	0.138	8.67	233	28.6	1.50	2.341	3.37	8.14	26.87	0.104
75035	Ilmenite Basalt	0.0906	0.546	0.163	11.6	322	32.9	1.93	1.796	3.35	9.78	27.74	0.102
79035	Soil breccia	0.165	1.16	0.315	5.88	182	15.8	0.961	1.912	3.68	11.5	30.91	0.106
79135	Regolith Breccia	0.189	1.34	0.368	5.88	190	15.0	0.901	1.948	3.63	12.7	32.23	0.100

Table 6.2: Selected crystal/silicate melt partition coefficients

Element	Olivine	Orthopyroxene	Clinopyroxine	Pigeonite	Plagioclase	Ilmenite
W	5.0E-03	5.9E-03	4.7E-02	5.9E-03	5.9E-04	7.5E-02
Nb	8.1E-05	1.3E-03	1.4E-03	1.3E-03	3.4E-04	5.9E-01
Ta	5.4E-05	7.6E-04	9.9E-04	7.6E-04	2.5E-04	9.9E-01
Zr	3.3E-04	1.6E-03	1.0E-02	1.6E-03	3.6E-04	3.0E-01
Hf	3.9E-04	5.0E-03	2.4E-02	5.0E-03	2.2E-04	4.1E-01
U	1.3E-05	5.1E-04	1.3E-03	5.0E-04	4.2E-04	3.9E-03
Th	4.0E-06	2.6E-05	1.3E-03	2.6E-05	1.9E-04	6.0E-04

The partition coefficients used for trace element modeling. Note that partition coefficients for W are always higher than Hf in the relevant mineral constituents of low-Ti mare basalt

Appendix 1.0 Lunar Samples Gallery

*Looking at these stars suddenly dwarfed my own troubles
and all the gravities of terrestrial life.*

The Time Machine

By H.G. Wells

1895

A1.1 Apollo 11

Sources for mineralogical percents listed with each sample. Each picture is scaled to 3cm as the size from first to last digit of the sample numbers (8 digits)



Sample 10017.395

Type: Fine-grained, vesicular, ilmenite basalt. Grains vary from fine to medium sized.

Minerals: clinopyroxene (51%), plagioclase (21.5%), and ilmenite (20.2%), Mesostasis (6.1%).

Source: Kushiro & Nakamura, 1970



Sample 10020.250:

Type: Fine grained ilmenite basalt.

Minerals: Pyroxene (54.8%), Olivine (4.8%), Plagioclase (21.4%), Ilmenite (17%), Glass Silicate (0.9%)

Source: Haggerty *et al.* 1970



Sample 10057.279

Type: Fine grained imenite basalt

Minerals: Pyroxene (50.8%), Plagioclase (24%), Opaques (15.5%), Cristobalite (1.05%), Mesostasis (8.04%)

Source: Beaty & Albee 1978

A1.2 Apollo 12



Sample 12004.163

Type: Porphyritic olivine basalt.

Minerals: Olivine (12.5%), Pyroxene (63.6%), Plagioclase (14.4%), Ilmenite (9.1%), Mesostasis (3%)

Source: Papike *et al.* 1976



Sample 12022.333

Type: Ilmenite basalt

Minerals: Olivine (19.5%), Pyroxene (56%), Plagioclase (12.2%), Opaques (9%), Mesostasis (2.3%)

Source: Neal *et al.* 1994



Sample 12051.244

Type: Medium-grained subophitic ilmenite basalt

Minerals: Pyroxene (60.4%), Plagioclase (30.7%), Ilmenite (5.3%), Chrom+usp (1.4%), mesostasis (1.2%)

Source: Neal *et al.* 1994



Sample 12053.285

Type: Porphyritic pigeonite basalt

Minerals: Pyroxene (67.1%), Plagioclase (21.1%), Ilmenite (3.9%), Chrom+usp (1.6%), mesostasis (4.6%)

Source: Neal *et al.* 1994



Sample 12054.143

Type: Medium-grained ilmenite basalt

Minerals: Olivine (10.8%), Pyroxene (62.1%), Plagioclase (27.9%), Ilmenite (5.2%), Chromite (2%), Mesostasis (2%)

Source: Neal *et al.* 1994



Sample 12063.337

Type: Ilmenite bearing medium-grained porphyritic olivine, pyroxene basalt

Minerals: Olivine (2.8%), Pyroxene (64.6%), Plagioclase (21.6%), Ilmenite (4.6%), chrom+usp (3.4%), mesostasis (2.5%)

Source: Neal *et al.* 1994

A1.3 Apollo 13

No samples returned.

A1.4 Apollo 14



Sample 14163.945

Type: Bulk soil sample

Soil Content: Agglutinates (45.7%), Basalt (2.8%), Breccia (31%), Anorthosite (2.9%), Plagioclase (5.1%), Pyroxene (2.6%), Glass (10%)

Source: Simon *et al.* 1981



Sample 14305.674

Type: Crystalline matrix breccia

Composition: Seriate matrix with 30% lithic clasts, including olivine gabbro-norite, VHK basalt, ferrobasalt

Source: Taylor *et al.* 1983



Sample 14310.689

Type: KREEP rich feldspathic basalt

Minerals: Plagioclase (68%), Pyroxene (31%), Opaque (0.5%), Mesostasis (0.5%)

Source: Carlson *et al.* 1978

A1.5 Apollo 15



Sample 15058.302

Type: Pigeonite basalt

Minerals: Olivine (1.8%), Pyroxene (66.3%), Plagioclase (27.1%), Opaques (2.8%), Silica (2.1%)

Source: Rhodes & Hubbar 1973

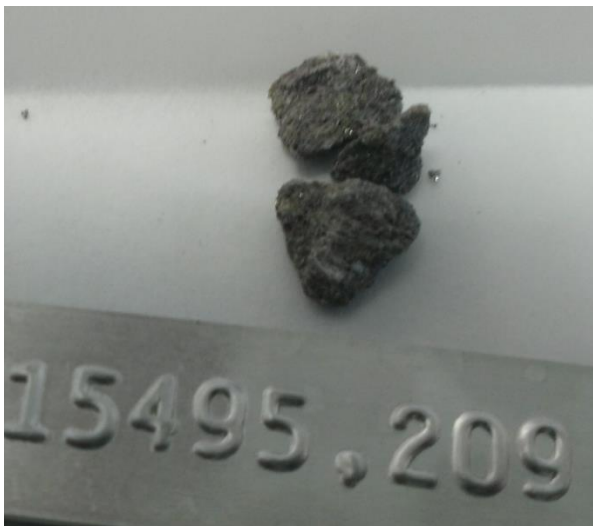


Sample 15065.189

Type: Coarse-grained gabbroic basalt

Minerals: Olivine (1.3%), Pyroxene (63%), Plagioclase (31.6%), Opaques (2.2%), Silica (1.9%)

Source: Longhi *et al.* 1972



Sample 15495.209

Type: Vuggy porphyritic pigeonite basalt

Minerals: Pyroxene (60%), Plagioclase (40%)

Source: Butler 1971



Sample 15545.103

Type: Olivine-normative basalt

Mineralogy: Olivine (8.2%), Pyroxene (61.4%), Plagioclase (23.5%), Ilmenite (6%), Silica (0.5%)

Source: Papike *et al.* 1976



Sample 15555.1070

Type: Olivine-normative basalt

Mineralogy: Olivine (12.1%), Pyroxene (52.4%), Plagioclase (30.4%), Opaques (2.7%), Mesostasis (2.3%)

Source: Longhi *et al.* 1972



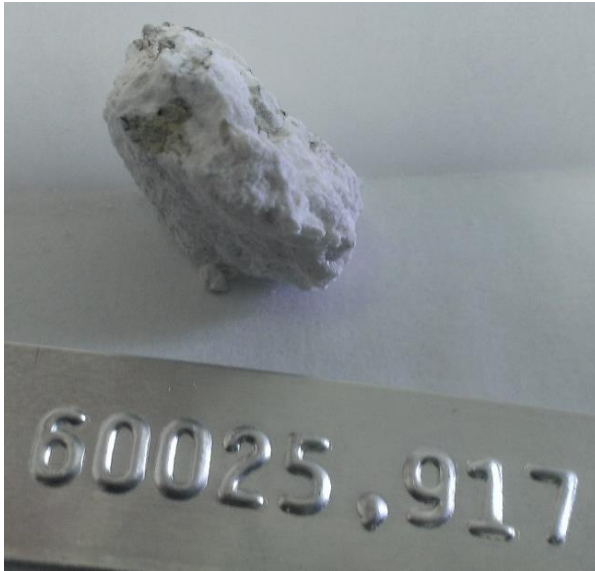
Sample 15556.250

Type: Vesicular olivine-normative basalt

Mineralogy: Olivine (0.1%), Pyroxene (57%), Plagioclase (38%), Ilmenite (2%), Spinel (1%), Mesostasis (1%), Silica (1%)

Source: McGee *et al.* 1979

A1.6 Apollo 16



Sample 60025.917

Type: Coarse-grained cataclastic anorthosite

Mineralogy: Plagioclase (74%), Olivine (20%), Orthopyroxene (5%), Augite (1%), Chromite (0.05%), Ilmenite (0.02%)

Source: James *et al.* 1991



Sample 65015.295

Type: KREEP rich poikilitic impact melt breccia

Mineralogy: Plagioclase (61%), Low-Ca pyroxene (29%), High-Ca pyroxene (6%), Olivine (1%), Opaques (3%)

Source: Simonds *et al.* 1973



Sample 67075.31

Type: Friable ferroan anorthosite

Mineralogy: Plagioclase (99%), Pyroxene (1%)

Source: Steele & Smith 1973



Sample 68115.297

Type: Polymict breccia

Description: Sample is dominated by flow-banded glass. It is largely composed of impact melts, with large varieties of recrystallized textures. Inclusions are plagioclase dominated

Source: Ryder & Norman 1980

A1.7 Apollo 17



Sample 72275.629

Type: Feldspathic breccia with aphanitic matrix

Description: Sample is approximately 60% light porous matrix and 40% clasts. Clasts are primarily aphanitic microbreccia.

Source: Lunar Sample compendium



Sample 73275.93

Type: Impact melt breccia

Description: Sample is a micropoikilitic impact melt breccia with minor vesicularity

Source: Lunar Sample compendium



Sample 74255.215

Type: Vesicular porphyritic coarse-grained ilmenite bearing basalt

Mineralogy: Olivine (3.2%), Pyroxene (48.6%), Opaques (38.6%), Plagioclase (18%), Mesostasis (1.8%)

Source: Brown *et al.* 1975



Sample 74275.349

Type: Fine-grained high-Ti mare basalt with significant armalcolite

Mineralogy: Olivine (13%), Pyroxene (36%), Opaques (31%), Plagioclase (19%)

Source: Brown *et al.* 1975



Sample 75035.240

Type: Ilmenite basalt, representing a lava flow

Mineralogy: Pyroxene (45.4%), Plagioclase (32.7%), Ilmenite (13.8%), Silica (6.2%), Mesostasis (1.9%)

Source: Brown *et al.* 1975



Sample 79035.190

Type: Regolith breccia, potentially contaminated by terrestrial moisture

Mineralogy: Agglutinate (33%), Breccia (2%), Mare lithics (14%), Highland lithics (10%), Mineral fragments (25%)

Source: Simon *et al.* 1990



Sample 79135.173

Type: Regolith breccia

Mineralogy: Agglutinate (14%), Breccia (2%), Mare lithics (4%), Highland lithics (8%), Mineral fragments (33%)

Source: Simon *et al.* 1990

Appendix 2.0 References

Science is magic that works.

Cat's Cradle

By Kurt Vonnegut

1963

- Adams, F. C. (2010). The Birth Environment of the Solar System. <https://doi.org/10.1146/annurev-astro-081309-130830>
- Agnor, C. B., & Hamilton, D. P. (2006). Neptune's capture of its moon Triton in a binary-planet gravitational encounter. *Nature*, 441(7090), 192–194. <https://doi.org/10.1038/nature04792>
- Albarede, F. (1989). Sm/Nd constraints on the growth rate of continental crust. *Tectonophysics*, 161(3–4), 299–305. [https://doi.org/10.1016/0040-1951\(89\)90160-1](https://doi.org/10.1016/0040-1951(89)90160-1)
- Albarède, F. (2009). Volatile accretion history of the terrestrial planets and dynamic implications. *Nature*, 461(7268), 1227–1233. <https://doi.org/10.1038/nature08477>
- Alibert, C., Norman, M. D., & McCulloch, M. T. (1994). An ancient Sm-Nd age for a ferroan noritic anorthosite clast from lunar breccia 67016. *Geochimica et Cosmochimica Acta*, 58(13), 2921–2926. [https://doi.org/10.1016/0016-7037\(94\)90125-2](https://doi.org/10.1016/0016-7037(94)90125-2)
- Allaby (2008) A Dictionary of Earth Sciences (3 ed.) Edited by MICHAEL ALLABY Next Edition: 4 ed. Latest Edition (4 ed.) Publisher: Oxford University Press Print Publication Date: 2008 Print ISBN-13: 9780199211944 Published online: 2008 Current Online Version: 2008 DOI: 10.1093/acref/9780199211944.001.0001 eISBN: 9780191726613
- Ampferer, O. (1925). Über Kontinentverschiebungen. *Die Naturwissenschaften*. *Nature*, 198(4886), 1145–1145. <https://doi.org/10.1038/1981145e0>
- Armstrong, R. M. G., Georg, R. B., Williams, H. M., & Halliday, A. N. (2012). Silicon isotopes in lunar rocks: Implications for the Moon's formation and the early history of the Earth. *Geochimica et Cosmochimica Acta*, 77, 504–514. <https://doi.org/10.1016/j.gca.2011.10.032>
- Ballhaus, C., Laurenz, V., Münker, C., Fonseca, R. O. C., Albarède, F., Rohrbach, A., Lagos, M., Schmidt, M.W., Jochum, K-P., Stoll, B., Weis, U., Helmy, H. M. (2013). The U/Pb ratio of the Earth's mantle—A signature of late volatile addition. *Earth and Planetary Science Letters*, 362, 237–245. <https://doi.org/10.1016/j.epsl.2012.11.049>
- Ballmer, M. D., Lourenço, D. L., Hirose, K., Caracas, R., & Nomura, R. (2017). Reconciling magma-ocean crystallization models with the present-day structure of the Earth's mantle. *Geochemistry, Geophysics, Geosystems*. <https://doi.org/10.1002/2017GC006917>
- Barboni, M., Boehnke, P., Keller, B., Kohl, I. E., Schoene, B., Young, E. D., & McKeegan, K. D. (2017). Early formation of the Moon 4.51 billion years ago. *Science Advances*, 3(1), 1–9. <https://doi.org/10.1126/sciadv.1602365>
- Bast, R., Scherer, E. E., Sprung, P., Fischer-Gödde, M., Stracke, A., & Mezger, K. (2015). A rapid and efficient ion-exchange chromatography for Lu-Hf, Sm-Nd, and Rb-Sr geochronology and the routine isotope analysis of sub-ng amounts of Hf by MC-ICP-MS. *Journal of Analytical Atomic Spectrometry*, 30(11), 2323–2333. <https://doi.org/10.1039/c5ja00283d>
- Beard, B. L., Taylor, L. A., Scherer, E. E., Johnson, C. M., & Snyder, G. A. (1998). The source region and melting mineralogy of high-titanium and low-titanium lunar basalts deduced from Lu-Hf

isotope data. *Geochimica et Cosmochimica Acta*, 62(3), 525–544. [https://doi.org/10.1016/S0016-7037\(97\)00373-6](https://doi.org/10.1016/S0016-7037(97)00373-6)

Beaty D.W. and Albee A.L. (1978) Comparative petrology and possible genetic relations among the Apollo 11 basalts. *Proc. 9th Lunar Planet. Sci. Conf.* 359-463.

Bédard, J. H. (2018). Stagnant lids and mantle overturns: Implications for Archaean tectonics, magmagenesis, crustal growth, mantle evolution, and the start of plate tectonics. *Geoscience Frontiers*. <https://doi.org/10.1097/ID.0000000000000646>

Binder, A. D. (1982). The mare basalt magma source region and mare basalt magma genesis. *Journal of Geophysical Research*, 87, A37–A53. <https://doi.org/10.1029/JB087iS01p00A37>

Bizzarro, M., Baker, J. A., & Haack, H. (2005). Mg isotope evidence for contemporaneous formation of chondrules and refractory inclusions. *Nature* (431), 275–278.

Borg, L. E., Connelly, J. N., Boyet, M., & Carlson, R. W. (2011). Chronological evidence that the Moon is either young or did not have a global magma ocean. *Nature*, 477(7362), 70–73. <https://doi.org/10.1038/nature10328>

Borg, L. E., Gaffney, A. M., & Shearer, C. K. (2014). A review of lunar chronology revealing a preponderance of 4.34-4.37 Ga ages. *Meteoritics and Planetary Science*, 50(4), 715–732. <https://doi.org/10.1111/maps.12373>

Borg, L. E., Gaffney, A. M., Shearer, C. K., DePaolo, D. J., Hutcheon, I. D., Owens, T. L., Ramon, E., Brennecke, G. (2009). Mechanisms for incompatible-element enrichment on the Moon deduced from the lunar basaltic meteorite Northwest Africa 032. *Geochimica et Cosmochimica Acta*, 73(13), 3963–3980. <https://doi.org/10.1016/j.gca.2009.03.039>

Borg, L. E., Shearer, C. K., Asmerom, Y., & Papike, J. J. (2004). Prolonged KREEP magmatism on the Moon indicated by the youngest dated lunar igneous rock. *Nature*, 432(7014), 209–211. <https://doi.org/10.1038/nature03070>

Bottke, W. F., Marchi, S., Swindle, T., Scott, E. R. D., Weirich, J. R., & Levison, H. (2015). Supplementary Material for Dating the Moon-forming impact event with asteroidal meteorites, 321(April), 321–324. <https://doi.org/10.1126/science.aaa0602>

Bouvier, A., Vervoort, J. D., & Patchett, P. J. (2008). The Lu-Hf and Sm-Nd isotopic composition of CHUR: Constraints from unequilibrated chondrites and implications for the bulk composition of terrestrial planets. *Earth and Planetary Science Letters*, 273(1–2), 48–57. <https://doi.org/10.1016/j.epsl.2008.06.010>

Bouvier, A., & Wadhwa, M. (2010). The age of the Solar System redefined by the oldest Pb-b age of a meteoritic inclusion. *Nature Geoscience*, 3(9), 637–641. <https://doi.org/10.1038/ngeo941>

Boyet, M., & Carlson, R. W. (2007). A highly depleted moon or a non-magma ocean origin for the lunar crust? *Earth and Planetary Science Letters*, 262(3–4), 505–516. <https://doi.org/10.1016/j.epsl.2007.08.009>

- Brandon, A. D., Lapen, T. J., Debaille, V., Beard, B. L., Rankenburg, K., & Neal, C. (2009). Re-evaluating $^{142}\text{Nd}/^{144}\text{Nd}$ in lunar mare basalts with implications for the early evolution and bulk Sm/Nd of the Moon. *Geochimica et Cosmochimica Acta*, 73(20), 6421–6445. <https://doi.org/10.1016/j.gca.2009.07.015>
- Brennan, (1983) *The Stones of Time: Calendars, Sundials, and Stone Chambers of Ancient Ireland, Inner traditions*
- Brown G.M., Peckett A., Emeleus C.H., Phillips R. and Pinsent R.H. (1975a) Petrology and mineralogy of Apollo 17 mare basalts. *Proc. 6th Lunar Sci. Conf.* 1-13.
- Büchel and Mertes, (1982). Die Eruptionszentren des Westeifeler Vulkanfeldes [The Eruption Centers of the West Eifel Volcanic Field]. *Hubertus Zeitschrift der Deutschen Geologischen Gesellschaft Band 133* (1982), p. 409 – 429 published: Jan 1, 1982
- Butler P. (1971) *Lunar Sample Catalog, Apollo 15*. Curators' Office, MSC 03209
- Calzada-Diaz, A., Joy, K. H., Crawford, I. A., & Nordheim, T. A. (2015). Constraining the source regions of lunar meteorites using orbital geochemical data. *Meteoritics and Planetary Science*, 50(2), 214–228. <https://doi.org/10.1111/maps.12412>
- Cameron, A. G. W., & Truran, J. W. (1977). The supernova trigger for formation of the solar system. *Icarus*, 30(3), 447–461. [https://doi.org/10.1016/0019-1035\(77\)90101-4](https://doi.org/10.1016/0019-1035(77)90101-4)
- Cameron, A. G. W., & Ward, W. R. (1976). The origin of the Moon. *Lunar Science*, 7, 120–122.
- Canup, R. M. (2012). Forming a moon with an Earth-like composition via a giant impact. *Science*, 338(6110), 1052–1055. <https://doi.org/10.1126/science.1226073>
- Canup, R. M. (2014). *Lunar-forming impacts : processes and alternatives Subject Areas*. Published by the Royal Society
- Canup, R. M., & Asphaug, E. (2001). Origin of the Moon in a giant impact near the end of the Earth's formation. *Nature*, 412(6848), 708–712. <https://doi.org/10.1038/35089010>
- Carlson, R. W., Borg, L. E., Gaffney, A. M., & Boyet, M. (2014). Rb-Sr, Sm-Nd and Lu-Hf isotope systematics of the lunar Mg-suite: The age of the lunar crust and its relation to the time of Moon formation. *Philosophical Transactions of the Royal Society A: Mathematical, Physical and Engineering Sciences*, 372(2024). <https://doi.org/10.1098/rsta.2013.0246>
- Carlson I.C. and Walton W.J.A. (1978) *Apollo 14 Rock Samples*. Curators Office. JSC 14240
- Carlson, R. W., & Lugmair, G. W. (1979). SmNd constraints on early lunar differentiation and the evolution of KREEP. *Earth and Planetary Science Letters*, 45(1), 123–132. [https://doi.org/10.1016/0012-821X\(79\)90114-6](https://doi.org/10.1016/0012-821X(79)90114-6)
- Chou, C.-L., (1978) Fractionation of Siderophile Elements in the Earth's Upper Mantle *Journal: in: Proceedings of the 9th Lunar and Planetary Science Conference, vol. 1, 219-230.*

- Condie, C. K., & Kröner, A. (2013). Geological Society of America Special Papers When did plate tectonics begin? Evidence from the geologic record. [https://doi.org/10.1130/2008.2440\(14\)](https://doi.org/10.1130/2008.2440(14))
- Connelly, J. N., & Bizzarro, M. (2016). Lead isotope evidence for a young formation age of the Earth–Moon system. *Earth and Planetary Science Letters*, 452, 36–43. <https://doi.org/10.1016/j.epsl.2016.07.010>
- Connelly, J. N., Bizzarro, M., Krot, A. N., Nordlund, Å., Wielandt, D., & Ivanova, M. A. (2012). The absolute chronology and thermal processing of solids in the solar protoplanetary disk. *Science*, 338(6107), 651–655. <https://doi.org/10.1126/science.1226919>
- Connelly, J. N., Bollard, J., & Bizzarro, M. (2017). Pb–Pb chronometry and the early Solar System. *Geochimica et Cosmochimica Acta*, 201, 345–363. <https://doi.org/10.1016/j.gca.2016.10.044>
- Connolly, H. C., & Desch, S. J. (2004). On the origin of the “kleine Kügelchen” called Chondrules. *Chemie Der Erde*, 64(2), 95–125. <https://doi.org/10.1016/j.chemer.2003.12.001>
- Crawford, I. A. (2015). Lunar resources: A review. *Progress in Physical Geography*, 39(2), 137–167. <https://doi.org/10.1177/0309133314567585>
- Crozaz, G., Floss, C., & Wadhwa, M. (2003). Chemical alteration and REE mobilization in meteorites from hot and cold deserts. *Geochimica et Cosmochimica Acta*, 67(24), 4727–4741. <https://doi.org/10.1016/j.gca.2003.08.008>
- Cuk, M., & Stewart, S. T. (2012). Making the Moon from a Fast-Spinning by Resonant Despinning, 1047(2012), 1047–1053. <https://doi.org/10.1126/science.1225542>
- Culler, T. S., Becker, T. A., Muller, R. A., & Renne, P. R. (2000). Lunar Impact History from ⁴⁰Ar/³⁹Ar Dating of Glass Spherules. *Science*, 287, 1785–1788.
- Daly, R. A. (1946). Origin of the Moon and Its Topography. *Proceedings of the American Philosophical Society*, Vol. 90, No. 2 (May, 1946), pp. Published by: American Philosophical Society Stable URL: <https://www.jstor.org/stab>, 90(2), 104–119.
- Dauphas, N., Burkhardt, C., Warren, P. H., & Teng, F. Z. (2014). Geochemical arguments for an impactor. *Philosophical Transactions of the Royal Society A: Mathematical, Physical and Engineering Sciences*, 372(August), 20130244. <https://doi.org/10.1098/rsta.2013.0244>
- Dauphas, N., & Pourmand, A. (2011). Hf-W-Th evidence for rapid growth of Mars and its status as a planetary embryo. *Nature*, 473(7348), 489–492. <https://doi.org/10.1038/nature10077>
- Davies, M. B. (2014) *Protostars and Planets VI* (Tucson, AZ: University of Arizona Press) pp 787–808
- Day, J. M. D., Pearson, D. G., & Lawrence, A. T. (2007). Highly Siderophile Element Constraints on Accretion and Differentiation of the Earth-Moon System, 315(March).
- Day, J., Puchtel, I., Walker, R., James, O., and Taylor, L. (2008). Osmium Abundance and isotope systematics of lunar crustal rocks and mare basalts In *Lunar Planet. Sci. Conf.*, volume 39, 1071.

- Day, J. M. D., & Walker, R. J. (2015). Highly siderophile element depletion in the Moon. *Earth and Planetary Science Letters*, 423, 114–124. <https://doi.org/10.1016/j.epsl.2015.05.001>
- Delano, J. W. (1986). Pristine lunar glasses: Criteria, data, and implications. *Journal of Geophysical Research: Solid Earth*, 91(B4), 201–213. <https://doi.org/10.1029/JB091iB04p0D201>
- Delano, J. W. (2009). Scientific, exploration of the moon. *Elements* (Vol. 5). <https://doi.org/10.2113/gselements.5.1.11>
- Denis, C. M. M., Demouchy, S., & Shaw, C. S. J. (2013). Evidence of dehydration in peridotites from Eifel Volcanic Field and estimates of the rate of magma ascent. *Journal of Volcanology and Geothermal Research*, 258, 85–99. <https://doi.org/10.1016/j.jvolgeores.2013.04.010>
- Der-Chuen, L., Halliday, A. N., Hunter, R. H., Holden, P., & Upton, B. G. J. (1993). Rb-Sr and Sm-Nd isotopic variations in dissected crustal xenoliths. *Geochimica et Cosmochimica Acta*, 57(1), 219–230. [https://doi.org/10.1016/0016-7037\(93\)90480-K](https://doi.org/10.1016/0016-7037(93)90480-K)
- Dickinson, J. E., & Hess, P. C. (1982). Zircon saturation in lunar basalts and granites. *Earth and Planetary Science Letters*, 57(2), 336–344. [https://doi.org/10.1016/0012-821X\(82\)90154-6](https://doi.org/10.1016/0012-821X(82)90154-6)
- Duncan, R. A., Petersen, N., & Hargraves, R. B. (1972). Mantle Plumes, Movement of the European Plates, and Polar Wandering.
- Dygert, N., Liang, Y., & Hess, P. (2013). The importance of melt TiO₂ in affecting major and trace element partitioning between Fe-Ti oxides and lunar picritic glass melts. *Geochimica et Cosmochimica Acta*, 106, 134–151. <https://doi.org/10.1016/j.gca.2012.12.005>
- Edmunson, J., Borg, L. E., Nyquist, L. E., & Asmerom, Y. (2009). A combined Sm-Nd, Rb-Sr, and U-Pb isotopic study of Mg-suite norite 78238: Further evidence for early differentiation of the Moon. *Geochimica et Cosmochimica Acta*, 73(2), 514–527. <https://doi.org/10.1016/j.gca.2008.10.021>
- Ehrenberg, S. N., & Griffin, W. L. (1979). Garnet granulite and associated xenoliths in minette and serpentinite diatremes of the Colorado Plateau. *Geology*, 7(10), 483–487. [https://doi.org/10.1130/0091-7613\(1979\)7<483:GGAAXI>2.0.CO;2](https://doi.org/10.1130/0091-7613(1979)7<483:GGAAXI>2.0.CO;2)
- Elardo, S. M., Draper, D. S., & Shearer, C. K. (2011). Lunar Magma Ocean crystallization revisited: Bulk composition, early cumulate mineralogy, and the source regions of the highlands Mg-suite. *Geochimica et Cosmochimica Acta*, 75(11), 3024–3045. <https://doi.org/10.1016/j.gca.2011.02.033>
- Elkins-Tanton, L. T., Burgess, S., & Yin, Q. Z. (2011). The lunar magma ocean: Reconciling the solidification process with lunar petrology and geochronology. *Earth and Planetary Science Letters*, 304(3–4), 326–336. <https://doi.org/10.1016/j.epsl.2011.02.004>
- Elkins Tanton, L. T., Van Orman, J. A., Hager, B. H., & Grove, T. L. (2002). Re-examination of the lunar magma ocean cumulate overturn hypothesis: Melting or mixing is required. *Earth and Planetary Science Letters*, 196(3–4), 239–249. [https://doi.org/10.1016/S0012-821X\(01\)00613-6](https://doi.org/10.1016/S0012-821X(01)00613-6)

Emery, J. V., R. J. Arculus, and C. E. Henderson, (1985). A possible mineral host for the unusual Sr- and Ba-enrichments in some lower crustal granulites and eclogites: Strontio-barytes, *Eos Trans. AGU*, 66, 387.

Fagan, T. J., Kashima, D., Wakabayashi, Y., & Sugino-hara, A. (2014). Case study of magmatic differentiation trends on the Moon based on lunar meteorite Northwest Africa 773 and comparison with Apollo 15 quartz monzodiorite. *Geochimica et Cosmochimica Acta*, 133, 97–127. <https://doi.org/10.1016/j.gca.2014.02.025>

Fagan, T. J., Taylor, G. J., Keil, K., Hicks, T. L., Killgore, M., Bunch, T. E., Wittke, J.H., Mittlefehldt D.W., Clayton R.N., Mayeda, T. K., Eugster O., Lorenzetti, S., Norman, M. D. (2003). Northwest Africa 773: Lunar origin and iron-enrichment trend. *Meteoritics and Planetary Science*, 38(4), 529–554. <https://doi.org/10.1111/j.1945-5100.2003.tb00025.x>

Fekiacova, Z., Mertz, D. F., Renne, P. R., Gutenberg-universität, J., & Geowissenschaften, I. (2007). Geodynamic Setting of the Tertiary Hocheifel Volcanism (Germany), Part I : 40 Ar / 39 Ar geochronology.

Fernandes, V. A., Burgess, R., & Turner, G. (2003). 40Ar-39Ar chronology of lunar meteorites Northwest Africa 032 and 773. *Meteoritics and Planetary Science*, 38(4), 555–564. <https://doi.org/10.1111/j.1945-5100.2003.tb00026.x>

Fisher (1889) *Physics of the Earth's Crust*, The Macmillan Company, New York

Fonseca, R. O. C., Mallmann, G., Sprung, P., Sommer, J. E., Heuser, A., Speelmanns, I. M., & Blanchard, H. (2014). Redox controls on tungsten and uranium crystal/silicate melt partitioning and implications for the U/W and Th/W ratio of the lunar mantle. *Earth and Planetary Science Letters*, 404, 1–13. <https://doi.org/10.1016/j.epsl.2014.07.015>

Frechen, J., Thiele, W., (1979). Petrographie der vulkanischen Foidite der Westeifel. *N. Jb. Miner. Abh.* Volume 136, Pages 227-237

Fuchs, K., von Gehlen, K., Mälzer, H., Murawski, H., Semmel, A., (1983). Mode and Mechanism of Rhenish Plateau Uplift. In: *Plateau Uplift*, Springer

Gaffney, A. M., & Borg, L. E. (2013). A young age for KREEP formation determined from Lu-Hf isotope systematics of KREEP basalts and Mg-suite samples. 42nd Lunar and Planetary Science Conference, 176–177. <https://doi.org/10.1038/NGEO417>.

Gaffney, A. M., & Borg, L. E. (2014). A young solidification age for the lunar magma ocean. *Geochimica et Cosmochimica Acta*, 140, 227–240. <https://doi.org/10.1016/j.gca.2014.05.028>

Gaffney, A. M., Borg, L. E., Asmerom, Y., Shearer, C. K., & Burger, P. V. (2011). Disturbance of isotope systematics during experimental shock and thermal metamorphism of a lunar basalt with implications for Martian meteorite chronology. *Meteoritics and Planetary Science*, 46(1), 35–52. <https://doi.org/10.1111/j.1945-5100.2010.01137.x>

- Gaidos, E., Krot, A. N., Williams, J. P., & Raymond, S. N. (2009). 26Al and the formation of the solar system from a molecular cloud contaminated by Wolf-Rayet winds. *Astrophysical Journal*, 696(2), 1854–1863. <https://doi.org/10.1088/0004-637X/696/2/1854>
- Garcia-Castellanos, D., Cloetingh, S., & Van Balen, R. (2000). Modelling the Middle Pleistocene uplift in the Ardennes-Rhenish Massif: Thermo-mechanical weakening under the Eifel? *Global and Planetary Change*, 27(1–4), 39–52. [https://doi.org/10.1016/S0921-8181\(01\)00058-3](https://doi.org/10.1016/S0921-8181(01)00058-3)
- Garcia, R. F., Gagnepain-Beyneix, J., Chevrot, S., & Lognonné, P. (2011). Very preliminary reference Moon model. *Physics of the Earth and Planetary Interiors*, 188(1–2), 96–113. <https://doi.org/10.1016/j.pepi.2011.06.015>
- Garvie, O. G., Robinson, D.N. (1984). The Formation of Kelyphite and Associated Sub-Kelyphitic and Sculptured Surfaces On Pyrope from Kimberlite. *Kimberlites: 1: Kimberlites and altered rocks*(Vol. 11). Elsevier Science Publishers B.V. <https://doi.org/10.1016/B978-0-444-42273-6.50031-6>
- Georg, R. B., Halliday, A. N., Schauble, E. A., & Reynolds, B. C. (2007). Silicon in the Earth's core. *Nature*, 447(7148), 1102–1106. <https://doi.org/10.1038/nature05927>
- Glikson A., (2014) *The Archaean: Geological and Geochemical Windows into the Early Earth*, Springer
- Goes, S., Spakman, W., & Bijwaard, H. (1999). A lower mantle source for central European volcanism. *Science*, 286(5446), 1928–1934. <https://doi.org/10.1126/science.286.5446.1928>
- Granet, M., Wilson, M., & Achauer, U. (1995). Imaging a mantle plume beneath the French Massif Central. *Earth and Planetary Science Letters*, 136(3–4), 281–296. [https://doi.org/10.1016/0012-821X\(95\)00174-B](https://doi.org/10.1016/0012-821X(95)00174-B)
- Greenwood, R. C. (2006). Oxygen Isotope Variation in Stony-Iron Meteorites, 1763(2006), 2004–2007. <https://doi.org/10.1126/science.1128865>
- Greenwood, R. C., Barrat, J. A., Miller, M. F., Anand, M., Dauphas, N., Franchi, I. A., Sillard, P., Starkey, N. A. (2018). Oxygen isotopic evidence for accretion of Earth's water before a high-energy Moon-forming giant impact. *Science Advances*, 4(3). <https://doi.org/10.1126/sciadv.aao5928>
- Griffin, W.L., Carswell, D.A., Nixon, P.H., (1979). Lower crustal granulites and eclogites from Lesotho, southern Africa, in *The Mantle Sample: Inclusions in Kimberlites*, edited by F.R. Boyd, and H.O.A. Meyer, pp. 59-86, AGU, Washington, D.C.
- Gross, J., Joy, K. H., Sciences, P., Lunar, T., & Ocean, M. (2016). *Encyclopedia of Archival Science. Archives and Records*, 37(1), 79–81. <https://doi.org/10.2139/ssrn.2843112>
- Gross, J., Treiman, A. H., & Mercer, C. N. (2014). Lunar feldspathic meteorites: Constraints on the geology of the lunar highlands, and the origin of the lunar crust. *Earth and Planetary Science Letters*, 388, 318–328. <https://doi.org/10.1016/j.epsl.2013.12.006>
- Haggerty S.E., Boyd F.R., Bell P.M., Finger L.W. and Bryan W.B. (1970) Opaque minerals and olivine in lavas and breccias from Mare Tranquillitatis. *Proc. Apollo 11 Lunar Sci. Conf.* 513-538.

- Hartman, W. K., & Davis, D. R. (1975). Satellite-Sized Planetesimals and Lunar Origin. *Icarus* 24, 504–515.
- Haskin, L. A. (1998). The Imbrium impact and the thorium distribution at the lunar highlands surface, *16*(2), 305–322.
- Haskin, L. A., Korotev, R. L., Rockow, K. M., & Jolliff, B. L. (1998). The case for Imbrium origin of the Apollo thorium-rich impact-melt breccias. *Journal of Experimental Psychology: General*, 136(1), 23–42.
- Head, J. W., & Wilson, L. (1992). Review Article Platelet Rich Plasma : Clinical Applications in Dentistry. *Saspjournals.Com*, 2(6), 355–362. [https://doi.org/10.1016/0016-7037\(92\)90183-J](https://doi.org/10.1016/0016-7037(92)90183-J)
- Herwartz, D., Pack, A., Friedrichs, B., & Bischoff, A. (2014). Identification of the giant impactor Theia in lunar rocks. *Science*, 344(6188), 1146–1150. <https://doi.org/10.1126/science.1251117>
- Hess, P. C. (1994). Petrogenesis of lunar troctolites. *Journal of Geophysical research* 99, 19083-19093.
- Hess, P. C., & Parmentier, E. M. (1995). A model for the thermal and chemical evolution of the Moon's interior: implications for the onset of mare volcanism. *Earth and Planetary Science Letters*, 134(3–4), 501–514. [https://doi.org/10.1016/0012-821X\(95\)00138-3](https://doi.org/10.1016/0012-821X(95)00138-3)
- Hiesinger, H. (2003). Ages and stratigraphy of mare basalts in Oceanus Procellarum, Mare Nubium, Mare Cognitum, and Mare Insularum. *Journal of Geophysical Research*, 108(E7), 5065. <https://doi.org/10.1029/2002JE001985>
- Hiesinger, H., & Head, J. (2006). New Views of Lunar Geoscience: An Introduction and Overview. *Reviews in Mineralogy and Geochemistry*, 60(1), 1–81. <https://doi.org/10.2138/rmg.2006.60.1>
- Hiesinger, H., Head, J.W., Wolf, U., Jaumann, R., Neukum, G., (2011). "Ages and stratigraphy of lunar mare basalts: A synthesis", *Recent Advances and Current Research Issues in Lunar Stratigraphy*, William A. Ambrose, David A. Williams
- Hoernle, K., Zhang, Y.-S., & Graham, D. (1995). Seismic and geochemical evidence for large-scale mantle upwelling beneath the eastern Atlantic and western and central Europe. *Nature* 374,
- Hubbard, N. J., Meyer, C., Gast, P. W., & Wiesmann, H. (1971). The composition and derivation of Apollo 12 soils. *Earth and Planetary Science Letters*, 10(3), 341–350. [https://doi.org/10.1016/0012-821X\(71\)90040-9](https://doi.org/10.1016/0012-821X(71)90040-9)
- Humayun, M., & Clayton, R. N. (1995). Potassium isotope cosmochemistry: Genetic implications of volatile element depletion. *Geochimica et Cosmochimica Acta*, 59(10), 2131–2148. [https://doi.org/10.1016/0016-7037\(95\)00132-8](https://doi.org/10.1016/0016-7037(95)00132-8)
- Hunt, A. C., Cook, D. L., Lichtenberg, T., Reger, P. M., Ek, M., Golabek, G. J., & Schönbacher, M. (2018). Late metal–silicate separation on the IAB parent asteroid: Constraints from combined W and Pt isotopes and thermal modelling. *Earth and Planetary Science Letters*, 482, 490–500. <https://doi.org/10.1016/j.epsl.2017.11.034>

- Illies, J. H., Prodehl, C., Schmincke, H-G., Semmel, A.,(1979). The Quaternary Uplift of the Rhenish Shield in Germany. *Tectonophysics* 61, 197–225.
- Jacobsen, S. B. (2005). The Hf-W isotopic system and the origin of the Earth and Moon. *Annual Review of Earth and Planetary Sciences*, 33(1), 531–570.
<https://doi.org/10.1146/annurev.earth.33.092203.122614>
- Jacobson, S. A., Morbidelli, A., Raymond, S. N., O'Brien, D. P., Walsh, K. J., & Rubie, D. C. (2014). Highly siderophile elements in Earth's mantle as a clock for the Moon-forming impact. *Nature*, 508(1), 84–87. <https://doi.org/10.1038/nature13172>
- James O.B., Lindstrom M.M. and McGee J.J. (1991) Lunar ferroan anorthosite 60025: Petrology and chemistry of mafic lithologies. *Proc. 21st Lunar Planet. Sci. Conf.* 63-87. Lunar Planetary Institute, Houston.
- Jeans, J. (1929). *Astronomy and Cosmogony* (Cambridge Library Collection - Astronomy). Cambridge: Cambridge University Press. doi:10.1017/CBO9780511694363
- Jolliff, B. L., Gillis, J. J., Haskin, L. A., & Korotev, R. L. (2000). Surface expressions and crust-mantle origins. *Apollo The International Magazine Of Art And Antiques*, 105(1999), 4197–4216.
- Jolliff, B. L., Korotev, R. L., Zeigler, R. A., & Floss, C. (2003). Northwest Africa 773: Lunar mare breccia with a shallow-formed olivine-cumulate component, inferred very-low-Ti (VLT) heritage, and a KREEP connection. *Geochimica et Cosmochimica Acta*, 67(24), 4857–4879.
<https://doi.org/10.1016/j.gca.2003.08.012>
- Joy, K. H., Burgess, R., Hinton, R., Fernandes, V. A., Crawford, I. A., Kearsley, A. T., & Irving, A. J. (2011). Petrogenesis and chronology of lunar meteorite Northwest Africa 4472: A KREEPy regolith breccia from the Moon. *Geochimica et Cosmochimica Acta*, 75(9), 2420–2452.
<https://doi.org/10.1016/j.gca.2011.02.018>
- Jung, S., Vieten, K., Romer, R. L., Mezger, K., Hoernes, S., & Satir, M. (2012). Petrogenesis of tertiary alkaline magmas in the siebengebirge, Germany. *Journal of Petrology*, 53(11), 2381–2409.
<https://doi.org/10.1093/petrology/egs047>
- Kesson, S. E., & Ringwood, A. E. (1976). Mare basalt petrogenesis in a dynamic moon. *Earth and Planetary Science Letters*, 30(2), 155–163. [https://doi.org/10.1016/0012-821X\(76\)90241-7](https://doi.org/10.1016/0012-821X(76)90241-7)
- Khan, A., Connolly, J. A. D., Maclennan, J., & Mosegaard, K. (2007). Joint inversion of seismic and gravity data for lunar composition and thermal state. *Geophysical Journal International*, 168(1), 243–258. <https://doi.org/10.1111/j.1365-246X.2006.03200.x>
- Khan, A., Pommier, A., Neumann, G. A., & Mosegaard, K. (2013). The lunar moho and the internal structure of the Moon: A geophysical perspective. *Tectonophysics*, 609, 331–352.
<https://doi.org/10.1016/j.tecto.2013.02.024>
- Kleine, T., Münker, C., Mezger, K., & Palme, H. (2002). Rapid accretion and early core formation on asteroids and the terrestrial planets from Hf-W chronometry. *Nature*, 418(6901), 952–955.
<https://doi.org/10.1038/nature00982>

- Kleinschmidt, A. (1912). *Geschichte von Arenberg, Salm und Leyen 1789–1815*, Gotha
- König, S., Münker, C., Hohl, S., Paulick, H., Barth, A. R., Lagos, M., ... Büchl, A. (2011). The Earth's tungsten budget during mantle melting and crust formation. *Geochimica et Cosmochimica Acta*, 75(8), 2119–2136. <https://doi.org/10.1016/j.gca.2011.01.031>
- Königshof, P., Becker, R. T., & Hartenfels, S. (2016). The Rhenish Massif as a part of the European Variscides. *Münstersche Forschungen Zur Geologie Und Paläontologie*, 108(November), 1–13.
- Korotev, R. L., Jolliff, B. L., Zeigler, R. A., Gillis, J. J., & Haskin, L. A. (2003). Feldspathic lunar meteorites and their implications for compositional remote sensing of the lunar surface and the composition of the lunar crust. *Geochimica et Cosmochimica Acta*, 67(24), 4895–4923. <https://doi.org/10.1016/j.gca.2003.08.001>
- Korschinek, G., Bergmaier, A., Faestermann, T., Gerstmann, U. C., Knie, K., Rugel, G., ... Remmert, A. (2009). A new value for the half-life of ^{10}Be by Heavy-Ion Elastic Recoil Detection and liquid scintillation counting. *Nuclear Instruments and Methods in Physics Research, Section B: Beam Interactions with Materials and Atoms*, 268(2), 187–191. <https://doi.org/10.1016/j.nimb.2009.09.020>
- Kroner, U., & Romer, R. L. (2013). Two plates - Many subduction zones: The Variscan orogeny reconsidered. *Gondwana Research*, 24(1), 298–329. <https://doi.org/10.1016/j.gr.2013.03.001>
- Kruijer, T., Fischer-Gödde, M., Kleine, T., Sprung, P., Leya, I., Wieler, R., (2013). Neutron capture on Pt isotopes in iron meteorites and the Hf-W chronology of core formation in planetesimals. *Earth and Planetary Science Letters* 361, 162-172.
- Kruijer, T. S., & Kleine, T. (2017). Tungsten isotopes and the origin of the Moon. *Earth and Planetary Science Letters*, 475, 15–24. <https://doi.org/10.1016/j.epsl.2017.07.021>
- Kruijer, T. S., Kleine, T., Fischer-Gödde, M., & Sprung, P. (2015). Lunar tungsten isotopic evidence for the late veneer. *Nature*, 520(7548), 534–537. <https://doi.org/10.1038/nature14360>
- Kushiro I. and Nakamura Y. (1970) Petrology of some lunar crystalline rocks. *Proc. Apollo 11 Lunar Sci. Conf.* 607- 626.
- Laneuville, M., Wieczorek, M. A., Breuer, D., & Tosi, N. (2013). Asymmetric thermal evolution of the Moon. *Journal of Geophysical Research E: Planets*, 118(7), 1435–1452. <https://doi.org/10.1002/jgre.20103>
- Lawrence, D. J., Feldman, W. C., Barraclough, B. L., Binder, A. B., Elphic, R. C., Maurice, S., & Thomsen, D. R. (1998). Global elemental maps of the Moon: The Lunar Prospector gamma-ray spectrometer. *Science*, 281, 1484–1489.
- Lawrence, D. J., Feldman, W. C., Barraclough, B. L., Binder, A. B., Elphic, R. C., Maurice, S., Miller, M.C., Prettyman, T. H. (2000). Thorium abundances on the lunar surface. *Journal of Geophysical Research E: Planets*, 105(E8), 20307–20331. <https://doi.org/10.1029/1999JE001177>

- Lee, D. C., & Halliday, A. N. (1996). Hf-W isotopic evidence for rapid accretion and differentiation in the early solar system. *Science*, 274(5294), 1876–1879. <https://doi.org/10.1126/science.274.5294.1876>
- Lee, D. C., Halliday, A. N., Snyder, G. A., & Taylor, L. A. (1997). Age and origin of the moon. *Science*, 278(5340), 1098–1103. <https://doi.org/10.1126/science.278.5340.1098>
- Leitzke, F. P., Fonseca, R. O. C., Michely, L. T., Sprung, P., Münker, C., Heuser, A., & Blanchard, H. (2016). The effect of titanium on the partitioning behavior of high-field strength elements between silicates, oxides and lunar basaltic melts with applications to the origin of mare basalts. *Chemical Geology*, 440, 219–238. <https://doi.org/10.1016/j.chemgeo.2016.07.011>
- Leitzke, F. P., Fonseca, R. O. C., Sprung, P., Mallmann, G., Lagos, M., Michely, L. T., & Münker, C. (2017). Redox dependent behaviour of molybdenum during magmatic processes in the terrestrial and lunar mantle: Implications for the Mo/W of the bulk silicate Moon. *Earth and Planetary Science Letters*, 474, 503–515. <https://doi.org/10.1016/j.epsl.2017.07.009>
- Lin, Y., Tronche, E. J., Steenstra, E. S., & van Westrenen, W. (2017). Experimental constraints on the solidification of a nominally dry lunar magma ocean. *Earth and Planetary Science Letters*, 471, 104–116. <https://doi.org/10.1016/j.epsl.2017.04.045>
- Longhi J., Walker D., Stolper E.N., Grove T.L. and Hays J.F. (1972) Petrology of mare/rille basalts 15555 and 15065. In *The Apollo 15 Lunar Samples*, 131-134.
- Longhi, J. (2003). A new view of lunar ferroan anorthosites: Postmagma ocean petrogenesis. *Journal of Geophysical Research*, 108(E8), 5083. <https://doi.org/10.1029/2002JE001941>
- Looney, L. W., Tobin, J. J., & Fields, B. D. (2006). Radioactive Probes of the Supernova-contaminated Solar Nebula: Evidence that the Sun Was Born in a Cluster. *The Astrophysical Journal*, 652(2), 1755–1762. <https://doi.org/10.1086/508407>
- Lugmair, G.W., Carlson, R.W., (1978). The sm-nd history of KREEP. *Proc. 9th, Lunar Planet. Sci. Conf.*, 689-704
- Lugmair, G. W., & Shukolyukov, A. (1998). Early solar system timescales according to ⁵³Mn-⁵³Cr systematics. *Geochimica et Cosmochimica Acta*, 62(16), 2863–2886. [https://doi.org/10.1016/S0016-7037\(98\)00189-6](https://doi.org/10.1016/S0016-7037(98)00189-6)
- Lustrino, M., & Wilson, M. (2007). The circum-Mediterranean anorogenic Cenozoic igneous province. *Earth-Science Reviews*, 81(1–2), 1–65. <https://doi.org/10.1016/j.earscirev.2006.09.002>
- Mabuchi, H., Takahashi, H., Nakamura, Y., Notsu, K., & Hamaguchi, H. (1974). The half-life of ⁴¹Ca. *Journal of Inorganic and Nuclear Chemistry*, 36(8), 1687–1688. [https://doi.org/10.1016/0022-1902\(74\)80493-8](https://doi.org/10.1016/0022-1902(74)80493-8)
- Macpherson, G. J., Davis, A. M., & Zinner, E. K. (1995). The distribution of aluminum-26 in the early solar system - a reappraisal. *Meteoritics*, 30(4), 365–386. <https://doi.org/10.1111/j.1945-5100.1995.tb01141.x>

Matsumoto, R., Machida, M., & Hayashi, M. (2000). Computational Magnetohydrodynamics of Turbulence, Dynamos, and Jet Formation in Differentially Rotating Astrophysical Disks, (138), 632–637.

Matzner and McKee, (2000). Efficiencies of Low-Mass Star and Star Cluster Formation The Astrophysical Journal, 545:364-378, 2000 December 10© 2000. The American Astronomical Society. All rights reserved. Printed in U.S.A.

McCulloch, M. T., & Black, L. P. (1984). SmNd isotopic systematics of Enderby Land granulites and evidence for the redistribution of Sm and Nd during metamorphism. Earth and Planetary Science Letters, 71(1), 46–58. [https://doi.org/10.1016/0012-821X\(84\)90051-7](https://doi.org/10.1016/0012-821X(84)90051-7)

McGee P.E., Warner J.L. and Simonds C.H. (1977) Introduction to the Apollo Collections. Part I: Lunar Igneous Rocks. Curators Office, JSC.

Meier, T., Soomro, R. A., Viereck, L., Lebedev, S., Behrmann, J. H., Weidle, C., Cristiano, L., Hanemann, R. (2016). Mesozoic and Cenozoic evolution of the Central European lithosphere. Tectonophysics, 692, 58–73. <https://doi.org/10.1016/j.tecto.2016.09.016>

Melosh, H. J. (2014). New approaches to the Moon 's isotopic crisis Subject Areas : Philosophical Transactions of the Royal Society A: Mathematical, Physical and Engineering Sciences, 372.

Mertes H., (1983). Aufbau und Genese des Westeifeler Vulkanfeldes, Bochumer geologische und geotechnische Arbeiten ; 9 Verlag: Bochum : Selbstverl. XIV, 415 S. : Ill., graph. Darst., Kt. Zugl.: Bochum, Univ., Diss., 1982

Mertes, H., & Schmincke, H. (1985). Mafic potassic lavas of the Quaternary West Eifel volcanic field. Contrib Mineral Petrol 89,, 330–345.

Mertz, D.F., Budsky, A., Chauvel, C., Prelevic, D., Regelous, M., 2014. Zonation of the Pleistocene West Eifel volcanism (Germany): relating isotopic, geochemical and geochronological evidence to the seismic low-velocity anomaly in the asthenosphere. Schriftenr. Dt. Gesellsch. Geowiss. SDGG 85, 427.

Mertz, D. F., Löhnertz, W., Nomade, S., Pereira, A., Prelević, D., & Renne, P. R. (2015). Temporal-spatial evolution of low-SiO₂ volcanism in the Pleistocene West Eifel volcanic field (West Germany) and relationship to upwelling asthenosphere. Journal of Geodynamics, 88, 59–79. <https://doi.org/10.1016/j.jog.2015.04.002>

Metzger, A. e., Trombka, J. I., Peterson, L. E., Reedy, R. C., & Arnold, J. R. (1973). Lunar Surface Radioactivity: Preliminary Results of the Apollo 15 and Apollo 16 Gamma-Ray Spectrometer Experiments, 179(January).

Meyer, C. J., (1977). Petrology, mineralogy and chemistry of KREEP basalt. Physics and chemistry of the Earth, vol. 10, no. 4, 29-260

Meyer, C. (2012). Lunar Sample Compendium Introduction. Lunar Sample Compendium, Astromater.

- Meyer, J., Elkins-Tanton, L., & Wisdom, J. (2010). Coupled thermal-orbital evolution of the early Moon. *Icarus*, 208(1), 1–10. <https://doi.org/10.1016/j.icarus.2010.01.029>
- Meyer, R., & Foulger, G. R. G. R. (2007). The European Cenozoic Volcanic Province is not caused by mantle plumes. <http://www.Mantleplumes.Org/Europe.html>, 1–17. Retrieved from [http://seisweb2.oma.be/bibadmin/uploads/pdf/Meyer and Foulger_No plume under Europe_MantlePlumes-org_2007.pdf%5Cnhttp://www.mantleplumes.org/Europe.html](http://seisweb2.oma.be/bibadmin/uploads/pdf/Meyer_and_Foulger_No_plume_under_Europe_MantlePlumes-org_2007.pdf%5Cnhttp://www.mantleplumes.org/Europe.html)
- Montmerle, T., Augereau, J. C., Chaussidon, M., Gounelle, M., Marty, B., & Morbidelli, A. (2006). Solar system formation and early evolution: The first 100 million years. *Earth, Moon and Planets*, 98(1–4), 39–95. <https://doi.org/10.1007/s11038-006-9087-5>
- Mougel, B., Moynier, F., & Göpel, C. (2018). Chromium isotopic homogeneity between the Moon, the Earth, and enstatite chondrites. *Earth and Planetary Science Letters*, 481, 1–8. <https://doi.org/10.1016/j.epsl.2017.10.018>
- Münker, C. (2010). A high field strength element perspective on early lunar differentiation. *Respiratory Therapy*, 5(2), 25–27, 65. <https://doi.org/10.1016/j.gca.2010.09.021>
- Munker, C., Weyer, S., Scherer, E., & Mezger, K. (2001). Separation of high field strength elements Nb, Ta, Zr, Hf and Lu from rock samples for MC-ICP-MS measurements. *Geochemistry, Geophysics, Geosystems*, 2(12).
- Neal C.R., Hacker M.D., Snyder G.A., Taylor L.A., Liu Y.- G. and Schmitt R.A. (1994) Basalt generation at the Apollo 12 site, Part 1: New data, classification and re-evaluation. *Meteoritics* 29, 334-348.
- Nemchin, A. A., Grange, M. L., Pidgeon, R. T., & Meyer, C. (2012). Lunar zirconology. *Australian Journal of Earth Sciences*, 59(2), 277–290. <https://doi.org/10.1080/08120099.2011.613484>
- Nemchin, A., Timms, N., Pidgeon, R., Geisler, T., Reddy, S., & Meyer, C. (2009). Timing of crystallization of the lunar magma ocean constrained by the oldest zircon. *Nature Geoscience*, 2(2), 133–136. <https://doi.org/10.1038/ngeo417>
- Newsom, H. E., Sims, K. W. W., Noll, P. D., Jaeger, W. L., Maehr, S. A., & Beserra, T. B. (1996). The depletion of tungsten in the bulk silicate earth: Constraints on core formation. *Geochimica et Cosmochimica Acta*, 60(7), 1155–1169. [https://doi.org/10.1016/0016-7037\(96\)00029-4](https://doi.org/10.1016/0016-7037(96)00029-4)
- Nimmo, F., & Kleine, T. (2007). How rapidly did Mars accrete? Uncertainties in the Hf-W timing of core formation. *Icarus*, 191(2), 497–504. <https://doi.org/10.1016/j.icarus.2007.05.002>
- North-Valencia, S.N., Joliff, B.L., Korotev, R.L., (2014). Ferroan Gabbro and Leucogabbro Lithologies in NWA 3170, possible petrogenetic link, and comparison to NWA 2727. Dept. of Earth & Planetary Science, Washington University in St. Louis, MO, 63130, USA
- Nyquist, L.E., Shih, C.-Y., Reese, Y.D., Irving, A.J., (2009). Sm-Nd and Rb-Sr ages for northwest Africa 2977, a young Lunar Gabbro from the PKT. <https://ntrs.nasa.gov/search.jsp?R=20090020687> 2018-10-27T19:52:30+00:00Z

Nyquist, L., Bogard, D., Yamaguchi, A., Shih, C. Y., Karouji, Y., Ebihara, M., Reese, Y., Garrison, D., McKay, G., Takeda, H. (2006). Feldspathic clasts in Yamato-86032: Remnants of the lunar crust with implications for its formation and impact history. *Geochimica et Cosmochimica Acta*, 70(24), 5990–6015. <https://doi.org/10.1016/j.gca.2006.07.042>

Nyquist, L. E., Wiesmann, H., Bansal, B., Shih, C. Y., Keith, J. E., & Harper, C. L. (1995). 146Sm-142Nd formation interval for the lunar mantle. *Geochimica et Cosmochimica Acta*, 59(13), 2817–2837. [https://doi.org/10.1016/0016-7037\(95\)00175-Y](https://doi.org/10.1016/0016-7037(95)00175-Y)

O'Hara, M. J., & Niu, Y. (2015). Obvious Problems in lunar petrogenesis and new perspectives. *The Geological Society of America Special Paper*, 71, 1–28. [https://doi.org/10.1130/2015.2514\(20\)](https://doi.org/10.1130/2015.2514(20))

O'Neill, C., Lenardic, A., Weller, M., Moresi, L., Quenette, S., & Zhang, S. (2016). A window for plate tectonics in terrestrial planet evolution? *Physics of the Earth and Planetary Interiors*. <https://doi.org/10.1016/j.pepi.2016.04.002>

Ozima, M., Yin, Q.-Z., Podosek, F. A., & Miura, Y. N. (2008). Toward understanding early Earth evolution: Prescription for approach from terrestrial noble gas and light element records in lunar soils. *Proceedings of the National Academy of Sciences*, 105(46), 17654–17658. <https://doi.org/10.1073/pnas.0806596105>

Padovani and Carter, (1977a). Aspects of the deep crustal evolution beneath south central New Mexico, in the Earth's Crust: Its Nature and Physical Properties, *Geophys. Monogr. Ser. 20*, edited by J.G. Headcock, pp. 19- 55, AGU, Washington, D.C.

Padovani and Carter, (1977b). Non-Equilibrium partial fusion due to decompression and thermal effects in crustal xenoliths, *Magma Genesis, Bull. Oreg. Dep. Geol. Miner. Ind.*, 96, 43-57,

Padovani, E. R., Hall, J., & Simmons, G. (1982). Constraints on crustal hydration below the Colorado plateau from Vp measurements on crustal xenoliths. *Tectonophysics*, 84(2–4), 313–328. [https://doi.org/10.1016/0040-1951\(82\)90165-2](https://doi.org/10.1016/0040-1951(82)90165-2)

Pahlevan, K., & Stevenson, D. J. (2007). Equilibration in the aftermath of the lunar-forming giant impact. *Earth and Planetary Science Letters*, 262(3–4), 438–449. <https://doi.org/10.1016/j.epsl.2007.07.055>

Palme, H., Hezel, D. C., & Ebel, D. S. (2015). The origin of chondrules: Constraints from matrix composition and matrix-chondrule complementarity. *Earth and Planetary Science Letters*, 411, 11–19. <https://doi.org/10.1016/j.epsl.2014.11.033>

Palme, H., & Rammensee, W. (1981). The significance of W in planetary differentiation processes: Evidence from new data on eucrites. *Journal of Experimental Psychology: General*, 136(1), 23–42.

Papike J.J., Hodges F.N., Bence A.E., Cameron M. and Rhodes J.M. (1976) Mare basalts: Crystal chemistry, mineralogy and petrology. *Rev. Geophys. Space Phys.* 14, 475-540.

Papike, J.J., Shearer, C.K., and Ryder, G. (1998) Lunar samples. In J.J. Papike, Ed., *Planetary Materials*, 36, p. 5–1 to 5–234. *Reviews in Mineralogy*, Mineralogical Society of America, Washington D.C.

Paul, D. K. (1971). Strontium Isotope Studies on Ultramafic Inclusions From Dreiser Weiher, Eifel, Germany. *Contributions to Mineralogy and Petrology*, 34(1), 22-.

Paulick, H., Münker, C., & Schuth, S. (2010). The influence of small-scale mantle heterogeneities on Mid-Ocean Ridge volcanism: Evidence from the southern Mid-Atlantic Ridge (7°30'S to 11°30'S) and Ascension Island. *Earth and Planetary Science Letters*, 296(3–4), 299–310.

<https://doi.org/10.1016/j.epsl.2010.05.009>

Pieters, C. M., Hanna, K.D., Cheek, L., Dhingra, D., Prissel, T., Jackson, C., Moriarty, D., Parman, S., Taylor, L.A., (2014). The distribution of Mg-spinel across the Moon and constraints on crustal origin †, *American Mineralogist* 99, 1893–1910.

Prissel, T. C., Parman, S. W., Jackson, C. R. M., Rutherford, M. J., Hess, P. C., Head, J. W., ... Pieters, C. M. (2014). Pink Moon: The petrogenesis of pink spinel anorthosites and implications concerning Mg-suite magmatism. *Earth and Planetary Science Letters*, 403, 144–156.

<https://doi.org/10.1016/j.epsl.2014.06.027>

Qin, L., Alexander, C. M. O. D., Carlson, R. W., Horan, M. F., & Yokoyama, T. (2010). Contributors to chromium isotope variation of meteorites. *Geochimica et Cosmochimica Acta*, 74(3), 1122–1145.

<https://doi.org/10.1016/j.gca.2009.11.005>

Rai, N., & Van Westrenen, W. (2014). Lunar core formation: New constraints from metal-silicate partitioning of siderophile elements. *Earth and Planetary Science Letters*, 388, 343–352.

<https://doi.org/10.1016/j.epsl.2013.12.001>

Rapp, J. F., & Draper, D. S. (2012). Experimental fractional crystallization of the Lunar magma ocean. *Science*, (5), 40–41. <https://doi.org/10.3747/co.21.2239>

Rapp J. F. and Draper D. S. 2013. Can fractional crystallization of a lunar magma ocean produce the lunar crust? (abstract #2732). 44th Lunar and Planetary Science Conference.

Rapp J. F. and Draper D. S. 2014. The lunar magma ocean: Sharpening the focus on process and composition (abstract #1527). 45th Lunar and Planetary Science Conference.

Rapp J. F. and Draper D. S. 2016. Moonage daydream: Reassessing the simple model for lunar magma oceancrystallization (abstract #2691). 45th Lunar and Planetary Science Conference.

Rapp, J. F., & Draper, D. S. (2018). Fractional crystallization of the lunar magma ocean: Updating the dominant paradigm. *Classical and Quantum Gravity*, 21(5), 1432–1455.

<https://doi.org/10.1111/maps.13086>

Regenauer-Lieb, K. (1998a). Dilatant plasticity applied to Alpine collision: Ductile void growth in the intraplate area beneath the Eifel volcanic field. *Journal of Geodynamics*.

[https://doi.org/10.1016/S0264-3707\(97\)00024-0](https://doi.org/10.1016/S0264-3707(97)00024-0)

Regenauer-Lieb, K. (1998b). Dilatant plasticity applied to Alpine collision: Ductile void growth in the intraplate area beneath the Eifel volcanic field. *Journal of Geodynamics*, 27(1), 1–21.

[https://doi.org/10.1016/S0264-3707\(97\)00024-0](https://doi.org/10.1016/S0264-3707(97)00024-0)

- Reufer, A., Meier, M. M. M., Benz, W., & Wieler, R. (2012). A hit-and-run giant impact scenario. *Icarus*, 221(1), 296–299. <https://doi.org/10.1016/j.icarus.2012.07.021>
- Reynolds, J. H. (1960). I-Xe dating of meteorites. *Journal of Geophysical Research*, 65(11), 3843. <https://doi.org/10.1029/JZ065i011p03843>
- Rhodes J.M. and Hubbard N.J. (1973) Chemistry, classification, and petrogenesis of Apollo 15 mare basalts. *Proc. 4th Lunar Sci. Conf.* 1127-1148.
- Ringwood, A. E. (1960). Some Aspects of the Thermal History of the Earth. *Geophysical Journal of the Royal Astronomical Society*, 4, 267–275. <https://doi.org/10.1111/j.1365-246X.1961.tb06818.x>
- Ringwood A.E. (1966), The chemical composition and origin of the Earth. *Advances in Earth Science*, MIT Press pp. 287-356
- Ritter, J. R. R., Jordan, M., Christensen, U. R., & Achauer, U. (2001). A mantle plume below the Eifel volcanic fields, Germany. *Earth and Planetary Science Letters*, 186(1), 7–14. [https://doi.org/10.1016/S0012-821X\(01\)00226-6](https://doi.org/10.1016/S0012-821X(01)00226-6)
- Rizo, H., Walker, R. J., Carlson, R. W., Touboul, M., Horan, M. F., Puchtel, I. S., Boyet, M., Rosing, M. T. (2016). Early Earth differentiation investigated through ^{142}Nd , ^{182}W , and highly siderophile element abundances in samples from Isua, Greenland. *Geochimica et Cosmochimica Acta*, 175, 319–336. <https://doi.org/10.1016/j.gca.2015.12.007>
- Rocholl, A., & Jochum, K. P. (1993). Th, U and other trace elements in carbonaceous chondrites: Implications for the terrestrial and solar-system Th U ratios. *Earth and Planetary Science Letters*, 117(1–2), 265–278. [https://doi.org/10.1016/0012-821X\(93\)90132-S](https://doi.org/10.1016/0012-821X(93)90132-S)
- Rogers, (1977). Granulite xenoliths from Lesotho kimberlites and the lower continental crust, *Nature*, 270, 681-684.
- Rudge, J. F., Kleine, T., & Bourdon, B. (2010). Broad bounds on Earth's accretion and core formation constrained by geochemical models. *Nature Geoscience*, 3(6), 439–443. <https://doi.org/10.1038/ngeo872>
- Rudnick, R. L., McDonough, W. F., & Chappell, B. W. (1993). Carbonatite metasomatism in the northern Tanzanian mantle: petrographic and geochemical characteristics. *Earth and Planetary Science Letters*, 114(4), 463–475. [https://doi.org/10.1016/0012-821X\(93\)90076-L](https://doi.org/10.1016/0012-821X(93)90076-L)
- Rudnick, R. L., & Taylor, S. R. (1987). The composition and petrogenesis of the lower crust: A xenolith study. *Journal of Geophysical Research: Solid Earth*, 92(B13), 13981–14005. <https://doi.org/10.1029/JB092iB13p13981>
- Rufu, R., Aharonson, O., & Perets, H. B. (2017). A multiple-impact origin for the Moon. *Nature Geoscience*, 10(2), 89–94. <https://doi.org/10.1038/ngeo2866>
- Ryder G. and Norman M.D. (1980) Catalog of Apollo 16 rocks (3 vol.). Curator's Office pub. #52, JSC #16904

- Shaw, C., Woodland, A. B., (2012). The role of magma mixing in the petrogenesis of mafic alkaline lavas, Rockeskyllerkopf Volcanic Complex, West Eifel, Germany. *Bulletin of Volcanology*. 74. 359-376. <https://doi.org/10.1007/s00445-011-0532-6>.
- Schmidt, G., & Snow, J. (2002). Os isotopes in mantle xenoliths from the Eifel volcanic field and the Vogelsberg (Germany): Age constraints on the lithospheric mantle. *Contributions to Mineralogy and Petrology*, 143(6), 694–705. <https://doi.org/10.1007/s00410-002-0372-7>
- Schmincke, H. U. (2007). The Quaternary volcanic fields of the East and West Eifel (Germany). *Mantle Plumes: A Multidisciplinary Approach*, 241–322. https://doi.org/10.1007/978-3-540-68046-8_8
- Schmincke, H. (2008). Volcanism of the East and West Eifel. *The Geology of Central Europe, Vol. 2: Mesozoic and Cenozoic*. 1318-1333.
- Schmincke, H. U. (2014). Eifelvulkanismus. *Mycolological Research (Vol. 106)*.
- Schmincke, H. U., & Mertes, H. (1979). Pliocene and Quarternary Volcanic Phases in the Eifel Volcanic Fields. *Naturwissenschaften*, 66(12), 615. <https://doi.org/10.3390/nu8070420>
- Schmincke, H. U., Park, C., & Harms, E. (1999). Evolution and environmental impacts of the eruption of Laacher See Volcano (Germany) 12 900 a BP. *Quaternary Internatio-Nal*, 61(1999), 61–72.
- Schmitt, A. K., Wetzel, F., Cooper, K. M., Zou, H., & Wörner, G. (2010). Magmatic longevity of laacher see volcano (Eifel, Germany) indicated by U-Th dating of intrusive carbonatites. *Journal of Petrology*, 51(5), 1053–1085. <https://doi.org/10.1093/petrology/egq011>
- Schönbächler, M., Carlson, R. W., Horan, M. F., Mock, T. D., & Hauri, E. H. (2010). Heterogeneous Accretion and the Moderately Volatile Element Budget on Earth. *Science* 328(May).
- Schulmann, K., Catalán, J. R. M., Lardeaux, J. M., Janoušek, V., & Oggiano, G. (2014). The Variscan orogeny: extent, timescale and the formation of the European crust. *Geological Society, London, Special Publications*, 405(1), 1–6. <https://doi.org/10.1144/SP405.15>
- Schulz, T., Münker, C., Mezger, K., & Palme, H. (2010). Hf-W chronometry of primitive achondrites. *Geochimica et Cosmochimica Acta*, 74(5), 1706–1718. <https://doi.org/10.1016/j.gca.2009.12.016>
- Schulz, T., Münker, C., Palme, H., & Mezger, K. (2009). Hf-W chronometry of the IAB iron meteorite parent body. *Earth and Planetary Science Letters*, 280(1–4), 185–193. <https://doi.org/10.1016/j.epsl.2009.01.033>
- Seck HA, Wedepohl KH (1983) Mantle xenoliths in the Rhenish Massif and the Northern Hessian Depression. In: Fuchs K *et al* (eds) Plateau Uplift - The Rh, AGU, Washington, D.C. enish Shield - A Case History. Springer (Heidelberg), pp 343-351
- Shang, H., Glassgold, A. E., & Shu, F. A. (2002). Heating and ionization of x -winds. *The Astrophysical Journal*, 564, 853-876

- Shaulis, B. J., Righter, M., Lapen, T. J., Jolliff, B. L., & Irving, A. J. (2017). 3.1 Ga crystallization age for magnesian and ferroan gabbro lithologies in the Northwest Africa 773 clan of lunar meteorites. *Geochimica et Cosmochimica Acta*, 213, 435–456. <https://doi.org/10.1016/j.gca.2017.06.031>
- Shaw, C. S. J., Eyzaguirre, J., Fryer, B., & Gagnon, J. (2005). Regional variations in the mineralogy of metasomatic assemblages in mantle xenoliths from the West Eifel Volcanic Field, Germany. *Journal of Petrology*, 46(5), 945–972. <https://doi.org/10.1093/petrology/egi006>
- Shearer, C. K. (2006). Thermal and Magmatic Evolution of the Moon. *Reviews in Mineralogy and Geochemistry*, 60(1), 365–518. <https://doi.org/10.2138/rmg.2006.60.4>
- Shearer, C. K., Elardo, S. M., Petro, N. E., Borg, L. E., & McCubin, F. M. (2015). Origin of the lunar highlands Mg-suite: An integrated petrology, geochemistry, chronology, and remote sensing perspective. *American Mineralogist*, 100(1), 294–325. <https://doi.org/10.2138/am-2015-4817>
- Shearer, C. K., & Papike, J. J. (1999). Magmatic evolution of the Moon. *American Mineralogist*, 84(10), 1469–1494. <https://doi.org/10.2138/am-1999-1001>
- Shearer, C. K., & Papike, J. J. (2005). Early crustal building processes on the moon: Models for the petrogenesis of the magnesian suite. *Geochimica et Cosmochimica Acta*, 69(13), 3445–3461. <https://doi.org/10.1016/j.gca.2005.02.025>
- Shu, F. H., Adams, F. C., & Lizano, S. (1987). Star Formation in Molecular Clouds: Observation and Theory. *Annual Review of Astronomy and Astrophysics*, 25(1), 23–81. <https://doi.org/10.1146/annurev.aa.25.090187.000323>
- Simon S.B., Papike J.J. and Laul J.C. (1981) The lunar regolith: Comparative studies of the Apollo and Luna sites. *Proc. 12th Lunar Planet. Sci. Conf.* 371-388.
- Simon S.B., Papike J.J., Gosselin D.C., Laul J.C., Hughes S.S. and Schmitt R.A. (1990) Petrology and chemistry of Apollo 17 regolith breccias: A history of mixing of highland and mare regolith. *Proc. 20th Lunar Planet. Sci.* 219-230. Lunar Planetary Institute, Houston.
- Simonds C.H., Warner J.L. and Phinney W.C. (1973) Petrology of Apollo 16 poikilitic rocks. *Proc. 4th Lunar Sci. Conf.* 613-632.
- Smith, J. V., Anderson, A. T., Newton, R. C., Olsen, E. J., Wyllie, P. J., Crewe, A. V., Isaacson, M.S., Johnson, D. (1970). Petrologic history of the moon inferred from petrography, mineralogy, and petrogenesis of Apollo 11 rocks. *Geochimica et Cosmochimica Acta Supplement, Volume 1. Proceedings of the Apollo 11 Lunar Science Conference, (April)*, 897–925.
- Snape, J. F., Nemchin, A. A., Bellucci, J. J., Whitehouse, M. J., Tartèse, R., Barnes, J. J., ... Joy, K. H. (2016). Lunar basalt chronology, mantle differentiation and implications for determining the age of the Moon. *Earth and Planetary Science Letters*, 451, 149–158. <https://doi.org/10.1016/j.epsl.2016.07.026>
- Snyder, A.G., Borg, L.E., Nyquist, L.E., Taylor, L.A., (2000). Chronology and Isotopic Constraints on Lunar Evolution. *Origin of the earth and moon*, edited by R.M. Canup and K. Righter and 69 collaborating authors. Tucson: University of Arizona Press., p.361-395

- Snyder, G. A., Taylor, L. A., & Neal, C. R. (1992). A chemical model for generating the sources of mare basalts: Combined equilibrium and fractional crystallization of the lunar magmasphere. *Geochimica et Cosmochimica Acta*, 56(10), 3809–3823. [https://doi.org/10.1016/0016-7037\(92\)90172-F](https://doi.org/10.1016/0016-7037(92)90172-F)
- Sobolev, S. V., Sobolev, A. V., Kuzmin, D. V., Krivolutskaya, N. A., Petrunin, A. G., Arndt, N. T., ... Vasiliev, Y. R. (2011). Linking mantle plumes, large igneous provinces and environmental catastrophes. *Nature*, 477(7364), 312–316. <https://doi.org/10.1038/nature10385>
- Sokol, A. K., Fernandes, V. A., Schulz, T., Bischoff, A., Burgess, R., Clayton, R. N., ... Horstmann, M. (2008). Geochemistry, petrology and ages of the lunar meteorites Kalahari 008 and 009: New constraints on early lunar evolution. *Geochimica et Cosmochimica Acta*, 72(19), 4845–4873. <https://doi.org/10.1016/j.gca.2008.07.012>
- Sprung, P., Kleine, T., & Scherer, E. E. (2013). Isotopic evidence for chondritic Lu/Hf and Sm/Nd of the Moon. *Earth and Planetary Science Letters*, 380, 77–87. <https://doi.org/10.1016/j.epsl.2013.08.018>
- Sprung, P., Kleine, T., & Scherer, E. E. (2014). Evidence for a common initial $^{176}\text{Hf}/^{177}\text{Hf}$ of the Earth, Moon and Chondrite. 11–12. <https://doi.org/10.1126/science.1231530>.Figure
- Sprung, P., Scherer, E. E., Upadhyay, D., Leya, I., & Mezger, K. (2010). Non-nucleosynthetic heterogeneity in non-radiogenic stable Hf isotopes: Implications for early solar system chronology. *Earth and Planetary Science Letters*, 295(1–2), 1–11. <https://doi.org/10.1016/j.epsl.2010.02.050>
- Steele I.M. and Smith J.V. (1973) Mineralogy and petrology of some Apollo 16 rocks and fines: General petrologic model of the moon. *Proc. 4th Lunar Sci. Conf.* 519-536.
- Steenstra, E. S., Rai, N., Knibbe, J. S., Lin, Y. H., & van Westrenen, W. (2016). New geochemical models of core formation in the Moon from metal-silicate partitioning of 15 siderophile elements. *Earth and Planetary Science Letters*, 441, 1–9. <https://doi.org/10.1016/j.epsl.2016.02.028>
- Stosch, H.-G., & Lugmair, G. W. (1984). Evolution of the lower continental crust: granulite facies xenoliths from the Eifel, West Germany. *Nature* 311.
- Stosch, H.-G., Lugmair, G. W., & Seck, H. A. (1986). Geochemistry of granulite-facies lower crustal xenoliths: implications for the geological history of the lower continental crust below the Eifel, West Germany. *Geological Society, London, Special Publications*, 24(1), 309–317. <https://doi.org/10.1144/GSL.SP.1986.024.01.27>
- Stosch, H. G., & Lugmair, G. W. (1986). Trace element and Sr and Nd isotope geochemistry of peridotite xenoliths from the Eifel (West Germany) and their bearing on the evolution of the subcontinental lithosphere. *Earth and Planetary Science Letters*, 80(3–4), 281–298. [https://doi.org/10.1016/0012-821X\(86\)90111-1](https://doi.org/10.1016/0012-821X(86)90111-1)
- Stosch, H. G., & Seck, H. A. (1980). Geochemistry and mineralogy of two spinel peridotite suites from Dreiser Weiher, West Germany. *Geochimica et Cosmochimica Acta*, 44(3), 457–470. [https://doi.org/10.1016/0016-7037\(80\)90044-7](https://doi.org/10.1016/0016-7037(80)90044-7)

- Stracke, A. (2012). Earth's heterogeneous mantle: A product of convection-driven interaction between crust and mantle. *Chemical Geology*, 330–331, 274–299. <https://doi.org/10.1016/j.chemgeo.2012.08.007>
- Stracke, A., Snow, J. E., Hellebrand, E., von der Handt, A., Bourdon, B., Birbaum, K., & Günther, D. (2011). Abyssal peridotite Hf isotopes identify extreme mantle depletion. *Earth and Planetary Science Letters*, 308(3–4), 359–368. <https://doi.org/10.1016/j.epsl.2011.06.012>
- Suess, E. (1892). *Das Antlitz der Erde*, 1. Verlag Tempsky Prag Wien Leipzig, 778 pp.
- Taylor L.A., Shervais J.W., Hunter R.H., Shih C.-Y., Nyquist L.E., Bansal B.M., Wooden J. and Laul J.C. (1983) Pre-4.2 AE mare-basalt volcanism in the lunar highlands. *Earth Planet. Sci. Lett.* 66, 33-47.
- Taylor, G. J. (2009). Ancient lunar crust: Origin, composition, and implications. *Elements*, 5(1), 17–22. <https://doi.org/10.2113/gselements.5.1.17>
- Taylor, S. R., (1975). *Lunar Science: A post-Apollo View* (Pergamon, New York, 1975)
- Terada, K., Anand, M., Sokol, A. K., Bischoff, A., & Sano, Y. (2007). Cryptomare magmatism 4.35 Gyr ago recorded in lunar meteorite Kalahari 009. *Nature*, 450(7171), 849–852. <https://doi.org/10.1038/nature06356>
- Thiemens, M. H., & Heidenreich, J. E. (1983). The Mass-Independent Fractionation of Oxygen : A Novel Isotope Effect and Its Possible Cosmochemical Implications. *Science* 219, 5–8.
- Thompson, W. (1864). On the secular cooling of the Earth. *Philosophical Magazine*, 25, 1–14.
- Touboul, M., Kleine, T., Bourdon, B., Palme, H., & Wieler, R. (2007). Late formation and prolonged differentiation of the Moon inferred from W isotopes in lunar metals. *Nature*, 450(7173), 1206–1209. <https://doi.org/10.1038/nature06428>
- Touboul, M., Kleine, T., Bourdon, B., Palme, H., & Wieler, R. (2009). Tungsten isotopes in ferroan anorthosites: Implications for the age of the Moon and lifetime of its magma ocean. *Icarus*, 199(2), 245–249. <https://doi.org/10.1016/j.icarus.2008.11.018>
- Touboul, M., Puchtel, I. S., & Walker, R. J. (2015). Tungsten isotopic evidence for disproportional late accretion to the Earth and Moon. *Nature*, 520(7548), 530–533. <https://doi.org/10.1038/nature14355>
- Turner, G., & Cadogan, P. H. (1975). The history of lunar bombardment inferred from Ar-40-Ar-39 dating of highland rocks. In: *Lunar Science Conference*, 6(January 1975), 1509–1538. Retrieved from http://adsabs.harvard.edu/cgi-bin/nph-data_query?bibcode=1975LPSC...6.1509T&link_type=ABSTRACT%0Apapers3://publication/uuid/E9FABE77-144A-436E-974F-4A7A6F0DD499
- Urey, H. C., 1952. *The Planets: their origin and development*. Yale University Press, New Haven, United States of America.

Urey, H. C. (1955). The Cosmic abundance of Potassium, Uranium, and Thorium and the heat balances of the Earth, the Moon, and Mars, *lign*, 41, 127–144.

Unruh, D.M., Stille, P., Patchett, P.J., Tatsumoto, M., (1984). Lu–Hf and Sm–Nd evolution in lunar mare basalts. In: *Proc. 14th Lunar Planet. Sci. Conf. Part 2*, pp. B459–477.

Van Orman, J. A., & Grove, T. L. (2000). Origin of lunar high-titanium ultramafic glasses: Constraints from phase relations and dissolution kinetics of clinopyroxene-ilmenite cumulates. *Meteoritics and Planetary Science*, 35(4), 783–794. <https://doi.org/10.1111/j.1945-5100.2000.tb01462.x>

Van Wees, J.-D., Stephenson, R. A., Ziegler, P. A., Bayer, U., Mccann, T., Dadlez, R., Gaupp, R., Narkiewicz, M., Bitzer, F., Scheck, M. (2000). On the origin of the Southern Permian Basin, Central Europe. *Marine and Petroleum Geology* 17, 40-59.

Vervoort, Jeff, D., & Blichert-Toft, J. (1999). Evolution of the depleted mantle: Hf isotope evidence from juvenile rocks through time. *The Handbook of Plant Biosecurity: Principles and Practices for the Identification, Containment and Control of Organisms That Threaten Agriculture and the Environment Globally*, 63(3), 119–148. https://doi.org/10.1007/978-94-007-7365-3_5

Vockenhuber, C., Oberli, F., Bichler, M., Ahmad, I., Quitté, G., Meier, M., Halliday, A.N., Lee, D.C., Kutschera, W., Steier, P., Gehrke, R.J., Helmer, R. G. (2004). New half-life measurement of ¹⁸²Hf: Improved chronometer for the early solar system. *Physical Review Letters*, 93(17). <https://doi.org/10.1103/PhysRevLett.93.172501>

Wade, J., & Wood, B. J. (2005). Core formation and the oxidation state of the Earth. *Earth and Planetary Science Letters*, 236(1–2), 78–95. <https://doi.org/10.1016/j.epsl.2005.05.017>

Walsh, K. J., Morbidelli, A., Raymond, S. N., O’Brien, D. P., & Mandell, A. M. (2011). A low mass for Mars from Jupiter’s early gas-driven migration. *Nature*, 475(7355), 206–209. <https://doi.org/10.1038/nature10201>

Walter, M., Newsom, H., Ertel, W., and Holzheid, A. (2000). Siderophile Elements in the Earth and Moon: Metal/Silicate Partitioning and Implications for Core Formation. *Origin of the Earth and Moon*, 265–289.

Wang, K., & Jacobsen, S. B. (2016). Potassium isotopic evidence for a high-energy giant impact origin of the Moon. *Nature*, 538(7626), 487–490. <https://doi.org/10.1038/nature19341>

Wänke, H., Palme, H., Baddenhausen, H., Dreibus, G., Jagoutz, E., Kruse, H., Palme, C., Spettel, B., Teschke, F., Thacker R., (1975). New data on the chemistry of lunar samples: Primary matter in the lunar highlands and the bulk composition of the moon *Proc. Lunar Sci. Conf. 6th* (1975), pp. 1313-1340

Wänke, H., Palme, H., Baddenhausen, H., Dreibus, G., Jagoutz, E., Kruse, H., Spettel, B., Teschke, F., Thacker, R. (1974). Chemistry of Apollo 16 and 17 samples: Bulk composition, late stage accumulation and early differentiation of the moon *Proc. Lunar Sci. Conf. 5th. Geochim. Cosmochim. Acta* (1974), pp. 1307-1335

- Warren, P. H. (1985). The magma ocean concept and Lunar evolution. *Earth and Planetary Science* 13, 201-240
- Warren, P. H. (1990). Lunar anorthosites and the magma-ocean plagioclase-flotation hypothesis: importance of FeO enrichment in the parent magma. *American Mineralogist*, 75(1–2), 46–58. <https://doi.org/0003-004X/90/0102-0046>
- Warren, P. H., & Taylor, G. J. (2014). *The Moon. Treatise on Geochemistry: Second Edition (Vol. 2)*. <https://doi.org/10.1016/B978-0-08-095975-7.00124-8>
- Warren, P. H., & Wasson, J. T. (1979). The origin of KREEP. *Reviews of Geophysics*, 17(1), 73–88. <https://doi.org/10.1029/RG017i001p00073>
- Weber, R. C., Lin, P. Y., Garnero, E. J., Williams, Q., & Lognonné, P. (2011). Seismic detection of the lunar core. *Science*, 331(6015), 309–312. <https://doi.org/10.1126/science.1199375>
- Wegener A., (1912). Die Entstehung der Kontinente. Dr. A. Petermann's Mitteilungen aus Justus Perthes' Geographischer Anstalt, 58(1):
- Weyer, S., Anbar, A. D., Brey, G. P., Münker, C., Mezger, K., & Woodland, A. B. (2005). Iron isotope fractionation during planetary differentiation. *Economic Computation and Economic Cybernetics Studies and Research*, 47(1), 97–112. <https://doi.org/10.1016/j.epsl.2005.09.023>
- Wiechert, U. (2001). Oxygen Isotopes and the Moon-Forming Giant Impact, 345(2001), 345–349. <https://doi.org/10.1126/science.1063037>
- Willbold, M., Elliott, T., & Moorbath, S. (2011). The tungsten isotopic composition of the Earth's mantle before the terminal bombardment. *Nature*, 477(7363), 195–198. <https://doi.org/10.1038/nature10399>
- Wilson, M., & Downes, H. (1991). Tertiary - quaternary extension-related alkaline magmatism in Western and central Europe. *Journal of Petrology*, 32(4), 811–849. <https://doi.org/10.1093/petrology/32.4.811>
- Wilson, M., & Downes, H. (1992). Mafic alkaline magmatism associated with the European Cenozoic rift system. *Tectonophysics*, 208(1–3), 173–182. [https://doi.org/10.1016/0040-1951\(92\)90343-5](https://doi.org/10.1016/0040-1951(92)90343-5)
- Wilson, M., & Downes, H. (2006). Tertiary-Quaternary intra-plate magmatism in Europe and its relationship to mantle dynamics. *Geological Society, London, Memoirs*, 32(1), 147–166. <https://doi.org/10.1144/GSL.MEM.2006.032.01.09>
- Wilson, M., & Patterson, R. (2001). Intraplate magmatism related to short-wavelength convective instabilities in the upper mantle: Evidence from the Tertiary-Quaternary volcanic province of western and central Europe. *Mantle Plumes: Their Identification Through Time.*, 37–58. <https://doi.org/10.1130/0-8137-2352-3.37>
- Witt-Eickschen, G., (2007). Thermal and geochemical evolution of the shallow subcontinental lithospheric mantle beneath the Eifel: Constraints from mantle xenoliths: a review.

- Witt-Eickschen, G., & Kramm, U. (1998). Evidence for the multiple stage evolution of the subcontinental lithospheric mantle beneath the Eifel (Germany) from pyroxenite and composite pyroxenite/peridotite xenoliths. *Contributions to Mineralogy and Petrology*, 131(2), 258–272. <https://doi.org/10.1007/s004100050392>
- Witt-Eickschen, G., & O'Neill, H. S. C. (2005). The effect of temperature on the equilibrium distribution of trace elements between clinopyroxene, orthopyroxene, olivine and spinel in upper mantle peridotite. *Chemical Geology*, 221(1–2), 65–101. <https://doi.org/10.1016/j.chemgeo.2005.04.005>
- Witt-Eickschen, G., Seck, H. A., Mezger, K., Eggins, S. M., & Altherr, R. (2003). Lithospheric mantle evolution beneath the Eifel (Germany): Constraints from Sr-Nd-Pb isotopes and trace element abundances in spinel peridotite and pyroxenite xenoliths. *Journal of Petrology*, 44(6), 1077–1095. <https://doi.org/10.1093/petrology/44.6.1077>
- Witt-eickschen, G., Seck, H. A., & Reys, C. (1993). Multiple enrichment processes and their relationships in the subcrustal lithosphere beneath the Eifel (Germany). *Journal of Petrology*, 34(1), 1–22. <https://doi.org/10.1093/petrology/34.1.1>
- Wittig, N., Humayun, M., Brandon, A. D., Huang, S., Leya, I., (2013). Coupled W-Os-Pt isotope systematics in IVB iron meteorites: In situ neutron dosimetry for W isotope chronology. *Earth and Planetary Science Letters*, 361, 152–161. <https://doi.org/10.1016/j.epsl.2012.10.013>
- Wolbeck, J., & Connolly, H. C. (2010). Origin of the Moon : Icy Impactor Model (IIM), (February).
- Wood, J., (1970). Lunar anorthosites and a geophysical model of the Moon. *Geochim. Cosmochim. Acta*. 34.
- Wood, B. J., Walter, M. J., & Wade, J. (2006). Accretion of the Earth and segregation of its core. *Nature*, 441(7095), 825–833. <https://doi.org/10.1038/nature04763>
- Worner, G., & Wright, T. L. (1984). Evidence for magma mixing within the Laacher See. *Journal of Volcanology and Geothermal Research* 22, 301-327.
- Wörner, G., Zindler, A., Staudigel, H., & Schmincke, H. U. (1986). Sr, Nd, and Pb isotope geochemistry of Tertiary and Quaternary alkaline volcanics from West Germany. *Earth and Planetary Science Letters*, 79(1–2), 107–119. [https://doi.org/10.1016/0012-821X\(86\)90044-0](https://doi.org/10.1016/0012-821X(86)90044-0)
- Yin, Q. Z., Zhou, Q., Li, Q. L., Li, X. H., Liu, Y., Tang, G. Q., ... Jenniskens, P. (2014). Records of the Moon-forming impact and the 470 Ma disruption of the L chondrite parent body in the asteroid belt from U-Pb apatite ages of Novato (L6). *Meteoritics and Planetary Science*, 49(8), 1426–1439. <https://doi.org/10.1111/maps.12340>
- Young, E. D., Kohl, I. E., Warren, P. H., Rubie, D. C., Jacobson, S. A., & Morbidelli, A. (2016). Giant Impact. *Science (New York, N.Y.)*, 351(6272), 493–496. <https://doi.org/10.1126/science.aad0525>
- Zhang, A. C., Hsu, W. B., Floss, C., Li, X. H., Li, Q. L., Liu, Y., & Taylor, L. A. (2010). Petrogenesis of lunar meteorite Northwest Africa 2977: Constraints from in situ microprobe results. *Meteoritics and Planetary Science*, 45(12), 1929–1947. <https://doi.org/10.1111/j.1945-5100.2010.01131.x>

Zhang, J., Dauphas, N., Davis, A. M., Leya, I., & Fedkin, A. (2012). The proto-Earth as a significant source of lunar material. *Nature Geoscience*, 5(4), 251–255. <https://doi.org/10.1038/ngeo1429>

Zhang, N., Parmentier, E. M., & Liang, Y. (2013). Effects of lunar cumulate mantle overturn and megaregolith on the expansion and contraction history of the Moon. *Geophysical Research Letters*, 40(19), 5019–5023. <https://doi.org/10.1002/grl.50988>

Ziegler, P. A. (1992). European Cenozoic rift system. *Tectonophysics*, 208(1–3), 91–111. [https://doi.org/10.1016/0040-1951\(92\)90338-7](https://doi.org/10.1016/0040-1951(92)90338-7)

Ziegler, P. A., & Dezes, P. (2006). Crustal evolution of Western and Central Europe. *Geological Society, London, Memoirs*, 32(1), 43–56. <https://doi.org/10.1144/GSL.MEM.2006.032.01.03>

Zolitschka, B., Negendank, J. F. W., & Lottermoser, B. G. (1995). Sedimentological proof and dating of the Early Holocene volcanic eruption of Ulmener Maar (Vulkaneifel, Germany). *Geologische Rundschau*, 84(1), 213–219. <https://doi.org/10.1007/BF00192252>

Appendix 3.0 Erklärung

Ich versichere, dass ich die von mir vorgelegte Dissertation selbständig angefertigt, die benutzten Quellen und Hilfsmittel vollständig angegeben und die Stellen der Arbeit – einschließlich Tabellen, Karten und Abbildungen –, die anderen Werken im Wortlaut oder dem Sinn nach entnommen sind, in jedem Einzelfall als Entlehnung kenntlich gemacht habe; dass diese Dissertation noch keiner anderen Fakultät oder Universität zur Prüfung vorgelegen hat; dass sie – abgesehen von unten angegebenen Teilpublikationen – noch nicht veröffentlicht worden ist, sowie, dass ich eine solche Veröffentlichung vor Abschluss des Promotionsverfahrens nicht vornehmen werde. Die Bestimmungen der Promotionsordnung sind mir bekannt. Die von mir vorgelegte Dissertation ist von Prof. Dr. Carsten Münker betreut worden.



Köln, den 11.11.2018

Appendix 4.0 Curriculum Vitae:

Maxwell Marzban Thiemens

Universität zu Köln, Institut für Geologie und Mineralogie, Zùlpicher Str. 49b D-50674 Köln, Germany
+49.175.344.3797 maxwellmt@gmail.com

Research Interests

Application of diverse isotope systems in studying the composition and subsequent evolution of the Earth's environments and biosphere.

Understanding planetary formation and evolution (including differentiation) via geochemical analyses.

Education

Universität zu Köln, Köln, Germany

September 2014 – Current

Doctor Rerum Naturalium (Doctorate of Natural Sciences)

Washington University in St. Louis, St. Louis, Mo

August 2010 – June 2012

Master of Arts with specialization in Isotope Geochemistry

University of California, San Diego

September 2004 – June 2010

Bachelors of Science: Geophysics

Experience

Research Assistant

May 2004 – September 2004 Department of Physics, UCSD, La Jolla, Ca

Research Assistant in Professor Ivan Schuller's Nano-technology Laboratory

Lab focus was condensed matter physics, surface reaction physics

Programmed and installed a stepper motor for the spray component of vacuum system

Research Fellow

April 2005 – August 2006 California Institute for Telecommunications and Information Technology, Department of Chemistry, UCSD, La Jolla, Ca

Research towards the creation of a micro-sensor in Andrew Kummel's Physical Chemistry Laboratory for investigations into photochemistry of gases on solid surfaces

Acquired data on the adsorption of Au on Pthalocyanine

Performed CMR (Complex Machine Repair) on ultra-low vacuum systems

Research Assistant

March 2007-July 2010 UCSD, La Jolla, Ca

Research Assistant in Professor Brian Keating's Astrophysics Laboratory. Cosmology, and early universe experiment group

Built telescope alignment system and circuitry for rocket payload

Aided in research on Cosmic Background Radiation from experiments based in Antarctica and Chile for investigations into the Big Bang

Astrophysics Cluster Teacher

Summers of 2007, 2008, 2009, 2010 California State Summer School for Mathematics and Science, UCSD, La Jolla, Ca

Introduced high school students to academic research in physics, such as construction and programming of electronic sensors for rocketry

Taught physics and astronomy in the style of a college course

Masters Student Washington University (Professor Fred Moynier)

August 2010-June 2012

- Worked in a clean laboratory and performed column chromatography for the isolation of zinc in carbonates, several species of methanogenic archaea, and cyanobacteria
- Cultivated three species of archaea (*Methanogenium frigidum*, *Methanocaldococcus jannaschii*, and *Methanococcus marispludis*) for the aforementioned zinc experiments
- Cultivated cyanobacteria for the monitoring of zinc fractionation over time

Universität Münster

September 2012-August 2014

- Developed Ti separation and analysis
- Performed freeze thaw separation of chondrules from meteorites, analyzed for Ti isotope composition, and analyzed chondrule composition with an SEM

Universität zu Köln, Köln, Germany

September 2014 – Current

- Performed mineral separations of Eifel Peridotites, dated the samples via Lu-Hf Sm-Nd, and Rb-Sr isochrons
- Analyzed a large suite of Lunar samples for HFSE compositions, and combined this data with experimental partitioning data for accurate modeling of element behavior
- Performed mineral separates on a KREEPy lunar meteorite, dating it with Lu-Hf to better understand the evolution of KREEP-rich components of the Moon

Bachelor Student Supervision (Carina Gerritzen)

Universität zu Köln, Köln, Germany

May 2017 – Current

- Teaching and supervising clean lab work, mineral separation and isochron construction
- Part of a collaboration with Washington University in St Louis (Assistant Professor Kun Wang) for a project analyzing volatiles in chondrules

Conferences

American Geophysical Union meeting

December 2011, San Francisco, California

Oral Presentation of “Zn and C isotopic evidence of climatic change during the Marinoan”

Lunar and Planetary Space Sciences meeting

March 2012, Houston, Texas

Poster presentation of “Zn and C isotopic variations associated with Neoproterozoic ice ages”

DMG-Sektionstreffen Geochemie und Petrologie/Petrophysik

May 2012, Münster, Germany

Invited Oral Presentation of “Zn, C, and O Isotopic Variations Associated with Neoproterozoic Ice Ages”

Fermor Meeting

September 2012, London, England.

Poster presentation of "Multi-Isotopic Comparison of Namibian Marinoan Cap Carbonates"

Invited speaker at Guiyang Institute of Geochemistry by the Chinese Academy of Sciences

May 2013, Guiyang, China

Oral Presentation of "Application of non-traditional isotopes to the Snowball Earth"

Paneth Kolloquium

October 2013, Nördlingen, Germany

Oral Presentation of “Ti isotope heterogeneities among chondrules”

Goldschmidt Conference

August 2015, Prague, Czech Republic

Poster Presentation of “Multi-Isotopic Dating of West Eifel Xenoliths”

American Geophysical Union meeting

December 2016, San Francisco, California

Poster Presentation of “Multi-Isotopic analyses of West Eifel Xenoliths”

DMG-Sektionstreffen Petrologie/Petrophysik & Geochemie

June 2016, Bremen, Germany

Poster presentation of “Multi-Isotopic Analysis of West-Eifel Xenoliths”

American Geophysical Union meeting

December 2016, San Francisco, California

Poster Presentation of “Extended HFSE systematics of Apollo samples – wrenching further Secrets from the Lunar Mantle”

Meteoritical Society meeting

July 2017, Santa Fe, New Mexico

Oral Presentation of “Early differentiation of the Moon from combined high precision HFSE measurements and partitioning experiments”

Goldschmidt Conference
August 2017, Paris, France
Poster Presentation of “The Lunar Hf/W Budget and the Age of the Moon”

Paneth Kolloquium
October 2017, Nördlingen, Germany
Oral Presentation of “Revising the Moon's W budget”

DMG-Sektionstreffen Geochemie und Petrologie/Petrophysik
June 2018, Göttingen, Germany
Oral Presentation of “New constraints on an old Moon”

Goldschmidt Conference
August 2018, Boston, Massachusetts
Presentation of "Lu-Hf Dating of Lunar Gabbro NWA 6950 – A Young
Manifestation of KREEP"

Geobonn
September 2018, Bonn, Germany
Oral Presentation of “Hf/W implications for an old Moon”

European Planetary Science Congress
September 2018, Berlin, Germany
Invited Oral Presentation of “Hf/W insights into the primeval Moon”

Skills

MC-ICP-MS trained
MAT 253 trained
ThermoFisher XSeries II Quadrupole ICP-MS trained
Scanning Electron Microscope trained
Synchrotron Trained (Chemical Dynamics Ultraviolet, 9.0.2 at the
Berkeley A.L.S.)
Clean lab work and Column Chromatography (Ti, Cr, Zn, Ni, Lu, Hf, Sm,
Nd, Rb, Sr, Ta, W, U, Th, Zr, Nb)
C and multi-oxygen stable isotope analysis
Ultra-high Vacuum System maintenance and use
Microbiology Cultivation and Analysis

Honors

Class Valedictorian
Revelle College, Class of 2010
University of California San Diego
Goldschmidt Student Poster Award
Goldschmidt Prague, 2015
Student Representative, Graduate School of Geological Sciences
Universität zu Köln
July 2015 – Present

*Science is made up of so many things that appear
obvious after they are explained.*

Dune

By F. Herbert

1965